UCLouvain

Faculty of Science
Department of Physics
Earth and Life Institute

RMI

Royal Meteorological Inst.
of Belgium
Dynamical Meteorology and
Climatology Unit

Variability and Predictability of Blocking Regimes from Idealised to General Circulation Models

---

Doctoral Dissertation presented by

Anupama Kuttikkat Xavier

in partial fulfillment of the requirements for the degree of
Doctor in Sciences of the Université catholique de Louvain

Thesis committee:

Prof. Michel Crucifix (Supervisor)	UCLouvain, Belgium
Prof. Lesley De Cruz	RMIB and Vrije Universiteit Brussel
Prof. Hugues Goosse	UCLouvain, Belgium
Dr. Gwendal Rivière	LMD, Paris, France
Dr. Stéphane Vannitsem (Supervisor)	Royal Meteorological Institute of Belgium
Prof. Qiuzhen Yin	UCLouvain, Belgium

Louvain-la-Neuve
October 2025

സമർപ്പണം (Dedication)

ഈ പ്രബന്ധം ഞാൻ എന്റെ അമ്മയ്ക്ക് സമർപ്പിക്കുന്നു...

സമൂഹത്തിന്റെ എല്ലാവിധ പ്രതികൂല സാഹചര്യങ്ങൾക്കും മുന്നിൽ, മക്കൾക്കുവേണ്ടി ഉറച്ച ശബ്ദമുയർത്തി പോരാടിയ ധീരയായ ആ സ്ത്രീരത്നത്തിന്.

അടച്ചുപൂട്ടലുകൾ ഇല്ലാത്ത സ്വപ്നങ്ങൾ കാണാനും, മുന്നോട്ട് നടക്കാനുള്ള അഗ്നിജ്വാല സ്വന്തം പെൺമക്കളുടെ മനസ്സിൽ പകർന്നുനൽകിയ ധൈര്യത്തിന്റെ പ്രതീകത്തിന്.

ആ സ്വപ്നങ്ങളിലേക്ക് പറന്നുയരാൻ എനിക്ക് ചിറകുകൾ നൽകിയ, എന്റെ ജീവിതത്തിലെ ഏറ്റവും വലിയ പോരാളിക്ക്.

"Even if you have lost everything, if a little courage still remains in you, remember — you have not lost anything!"

— A. P. J. Abdul Kalam

Acknowledgments

Moving to a different continent in pursuit of a PhD was a leap filled with uncertainty, excitement, and quiet fear. Yet what could have been an overwhelming journey slowly softened because of the people I met along the way. In a new country, you discover that places don't become familiar through landscapes, but through the warmth of the individuals who surround you. Belgium, with its unfamiliar skies and seasons, became a home away from home thanks to the kindness, generosity, and surprising connections that unfolded over these past four years. This thesis grew within that web of support shaped not only by academic guidance, but by the countless gestures, conversations, and shared moments that made the unfamiliar feel comforting and the difficult days feel bearable.

In this thesis, my deepest gratitude belongs to my supervisor, Stéphane Vannitsem. From the very first moment you decided to take a chance on me until the final days of this journey, you have been my unwavering source of support and confidence. I arrived here unsure, inexperienced, and unaware of even the basics of the field I was stepping into. Yet you met every hesitation of mine with patience, every question with clarity, and every obstacle with calm reassurance. Your guidance extended far beyond scientific advice. Through the endless paperwork, administrative challenges, and the bureaucratic hurdles tied to my immigration status, you stood beside me with kindness and understanding. There were countless forms to sign, countless requests that needed attention, and not once did you show frustration or reluctance. Your quiet willingness to help made the hardest parts of this journey feel lighter. More than a supervisor, you became a steady presence I could trust someone who offered not only academic wisdom, but also warm, fatherly reassurance in moments of doubt. Your words often carried a clarity that eased my fears and gave me the strength to keep moving. I am profoundly grateful for your belief in me, especially on the days when I struggled to believe in myself.

Michel, you entered my PhD journey quite late, but at a moment when I needed support more than ever. Even in my absence, you were willing to step in and offer exactly the reassurance and guidance I was desperately looking for.

Your straightforward honesty, your calm approach, and your ability to reassure me whenever something seemed to be going wrong became an anchor during a very uncertain period. Although I joined your group very late and never fully integrated in the way I wished I could, you still chose to stand by me and help me against all odds. Your willingness to support me despite the circumstances, despite the timing, despite everything made my final year far simpler, lighter, and genuinely less lonely. I am deeply grateful for the kindness and clarity you offered when I needed them most.

I am also deeply grateful to Francesco Ragone, who welcomed me as his student in the middle of my PhD with openness and sincerity. Your willingness to take me on at such a challenging moment, and the real-life advice you offered exactly when I needed it, meant far more than I can express here.

I would also like to thank Thomas Gilbert. Even though we often held different opinions, I remain genuinely appreciative of the support you gave me throughout my initial years—especially during my admissions and my early days settling into Brussels. Your help during that transition shaped the foundation on which the rest of my journey was built, and for that, I am truly thankful.

This project included two research visits, and I would like to express my heartfelt gratitude to Nili Harnik and Davide Faranda, who welcomed me under their expert guidance during these periods. These visits became invaluable milestones in my PhD, not only for the scientific insights I gained but also for the lessons I learned about balancing multiple research projects and stepping confidently into directions far outside my usual areas of expertise. I am deeply thankful for the way both of you helped me grow into a more independent and versatile researcher. Your groups in Tel Aviv and Paris were incredibly warm, welcoming, and accommodating, making me feel at ease from the very beginning. I am especially touched by the moments when you opened your homes to me, inviting me into your personal spaces with such kindness. Those experiences remain unforgettable, and I will always cherish the generosity and humanity you showed me during those visits.

I would like to extend my sincere gratitude to all the members of my jury: Lesly De Cruz, Hugues Goosse, and Gwendal Rivière. I am deeply thankful to each of you for taking the time, amidst your demanding schedules, to read the original version of this thesis and offer your thoughtful comments and critiques. Your insights have not only strengthened this work but have also pushed me to grow as a researcher. It has been a privilege to receive such careful attention and genuine engagement with my research. I also wish to express my appreciation to the president of my jury, Qiuzhen Yin, for the professional, warm, and truly enjoyable manner in which

the defences were conducted. Your presence and guidance made the experience both memorable and meaningful.

I have been incredibly fortunate to be part of the Marie Skłodowska-Curie international training network EDIPI project, working alongside a cohort of fourteen exceptional PhD students. I am grateful to each one of you for the countless conversations, the freedom to ask naïve questions without judgment, and the joy of learning about the wider field often over a drink in unforgettable places. Being part of this group made it so much easier to adapt to an entirely new culture, and I will always cherish how naturally and warmly you all welcomed me into this community. I owe special thanks to Sohan Suresan and Mireia Ginesta. Your help during my secondments in Tel Aviv and Paris, whether with paperwork, accommodation, or navigating the everyday challenges of being in a new city was invaluable. Your support made those transitions smoother and far less overwhelming, and I remain deeply grateful for your kindness.

I have been fortunate enough to be surrounded by a truly wonderful group of colleagues at the RMIB, whose support has meant more to me than they may ever realise. Being part of a community working on such a wide range of topics, from climate dynamics to day to day meteorology has been both inspiring and enriching. My PhD journey began with the immense help of Jonathan, who guided me through the earliest and most uncertain steps. You were always there when doubts overwhelmed me, and even when your schedule became incredibly busy, you still found time to help me with the most basic coding questions. I am also grateful to David, who welcomed me when I first arrived. I still remember how you encouraged me to speak up and engage with the group, even when my anxiety made that feel impossible. And to Benoît and Martin, who joined later but quickly became like family, thank you for creating a space where I could talk about anything without fear of judgment. Our conversations, our laughter, and the ease with which we formed a bond made the workplace feel less like an institution and more like a home. For all of you, this has been more than a research environment; it has been a family. And I believe, deeply, that this sense of family will remain with me even long after I leave.

If I have reached this final step of my PhD, one of the biggest reasons is you, Oisín. Thank you for putting up with my endless ranting, worries, and complaints for four entire years. We started at the same time, the only two PhD students in the group, and from the very beginning you were always there whenever I needed someone to talk to, someone to listen, or someone who truly understood what it meant to be a PhD student in this environment. I think you are the only person who can completely relate to my struggles, because you lived through them alongside me, and not once did you stop listening or lose patience. You taught me so much,

introducing me to new tools, helping me with Python and coding problems, guiding me through technical obstacles that felt impossible at the time. If I am honest, half of the tools I rely on today during this PhD came from you. It became completely normal for me to ask what I needed to do next, because you always had just done it before me. You made the path clearer simply by walking it first. These four years were far easier, lighter, and warmer because you were part of them. I am truly, deeply grateful for everything you have done for me.

Thank you to all my friends for the visits, the long conversations, and the much-needed escapes from work. I am especially grateful to Ketaki and Pavai, who stood by me through some of the most difficult moments of these years. Your presence, kindness, and unwavering support carried me through more than you know. I have also been incredibly lucky to share my life in Brussels with an amazing group of people who taught me so much about how to be a considerate, compassionate, and respectful human being. Living alongside you made my time here not just memorable, but truly transformative. And to Luca, thank you for the wonderful talks, the easy laughter, and the comfort of knowing I always had someone to share both the simple and the complicated moments with. Your companionship has been one of the brightest parts of these years.

പ്രിയപ്പെട്ട അമ്മയ്ക്ക്

എന്റെ ജീവിതത്തിൽ ഞാൻ ഏറ്റവും കൂടുതൽ കടപ്പെട്ടിരിക്കുന്നത് എന്റെ അമ്മയോടാണ്. ഇന്ന് ഞാൻ എത്തിച്ചേർന്നിട്ടുള്ള ഏതൊരു ഉയരത്തിന്റെയും അടിത്തറ, ഞാൻ പിറന്നുവീണ നാൾ മുതൽ അമ്മ എന്നെ ചുമലിലേറ്റിയ ത്യാഗങ്ങളും, അതിജീവിച്ച വേദനകളും, ചിന്തിയ കണ്ണീരുമാണ്. കഴിഞ്ഞ നാല് വർഷങ്ങൾ, നമ്മൾ ഒരുമിച്ചു കണ്ട സ്വപ്നങ്ങളെ യാഥാർത്ഥ്യത്തിലേക്ക് കൊണ്ടുപോയെങ്കിലും, അതിനു ഞാൻ കൊടുത്ത വില നിങ്ങളെ പിരിഞ്ഞ് ദൂരേക്ക് പോവുക എന്നതായിരുന്നു. എങ്കിലും, ഒറ്റപ്പെടലിന്റെയും ഏകാന്തതയുടെയും ഇടയിൽ തളരാതെ പൊരുതി ജയിക്കാൻ എന്നെ പ്രാപ്തയാക്കിയത് അതുവരെ എനിക്ക് പകർന്നുനൽകിയ അടിയുറച്ച ആത്മവിശ്വാസവും, പതറാത്ത ധൈര്യവുമാണ്. ഇന്ന് നമുക്കിടയിൽ അഭിപ്രായവ്യത്യാസങ്ങളുടെ നേർത്ത നിഴലുകൾ ഉണ്ടെങ്കിലും, ഈ ലോകത്ത് ഞാൻ എന്നും അമ്മയുടെ മകളാണ്. സ്നേഹത്തിന്റെയും ത്യാഗത്തിന്റെയും ഈ അമൂല്യമായ ഓർമ്മകൾക്ക് മുൻപിൽ, ഈ പി.എച്ച്. ഡി. പ്രബന്ധം ഞാൻ എന്റെ പ്രിയപ്പെട്ട അമ്മയ്ക്കായി സ്നേഹപൂർവ്വം സമർപ്പിക്കുന്നു.

എന്റെ സ്വന്തം അർച്ചനയ്ക്ക്

നീയില്ലെങ്കിൽ ഈ ജീവിതയാത്രയിൽ ഞാൻ ഒറ്റപ്പെട്ടുപോയേനെ. ഇന്നിവിടെ അഭിമാനത്തോടെ നിൽക്കുമ്പോൾ, കടന്നുപോയ നാല് വർഷങ്ങൾ എങ്ങനെയായിരുന്നെന്ന് എനിക്കോർമ്മയില്ല. പക്ഷെ, ആ നാല് വർഷ-

ങ്ങളിലും ഞാൻ ഏറ്റവും കൂടുതൽ സന്തോഷിച്ചതും, ആഴത്തിൽ സങ്കടപ്പെട്ടതുമായ നിമിഷങ്ങളിലെല്ലാം നീ ഒരു ഫോൺവിളിക്കപ്പുറം ഉണ്ടായിരുന്നു. പലപ്പോഴും നീ എന്റെ അനിയത്തിയാണെന്ന് ഞാൻ മറന്നുപോകാറുണ്ട്. ഞാൻ ബെൽജിയത്തിലേക്ക് പോയപ്പോൾ, നാട്ടിലെ എല്ലാ ഉത്തരവാദിത്തങ്ങളും ഒരു പരാതിയുമില്ലാതെ നീ ഏറ്റെടുത്ത് പൂർത്തിയാക്കി. നീ വീട്ടിലുണ്ടായിരുന്നപ്പോൾ എനിക്ക് ലഭിച്ചിരുന്ന ആശ്വാസം വാക്കുകൾക്കതീതമാണ്. ഇപ്പോഴും, ഏതൊരു സങ്കടത്തിലും നീ എന്റെ കൂടെ ഉണ്ടാവും എന്ന ഒരൊറ്റ ഉറപ്പിലാണ് ഞാൻ മുന്നോട്ട് പോകുന്നത്. എന്റെ വിജയങ്ങൾ നിന്റേതുകൂടിയാണ്.

ഈ യാത്രയിൽ എനിക്ക് പ്രചോദനവും ചാലകശക്തിയുമായി മാറിയ പ്രിയപ്പെട്ട അപ്പച്ചനും എന്റെ ഹൃദയം നിറഞ്ഞ നന്ദി. സ്വന്തം കാലിൽ ഉറച്ചുനിന്ന്, എന്റേതായ വഴികൾ തിരഞ്ഞെടുക്കാനുള്ള ആത്മധൈര്യം എനിക്ക് പകർന്നു തന്നത് അപ്പച്ചനാണ്. കൂടാതെ, എന്റെ സ്വപ്നങ്ങൾക്ക് പിന്നാലെ പോകാൻ എന്നെ എന്നും പ്രോത്സാഹിപ്പിച്ച വല്യപ്പനും വല്യമ്മയ്ക്കും എന്റെ പ്രത്യേക സ്നേഹവും നന്ദിയും അറിയിക്കുന്നു. നിങ്ങളുടെ വാക്കുകൾ ഓരോന്നും എനിക്ക് വലിയ ഊർജ്ജമായിരുന്നു.എന്റെ ബിരുദ, ബിരുദാനന്തര പഠനകാലഘട്ടങ്ങളിൽ അറിവിന്റെ വെളിച്ചം പകർന്നു നൽകിയ എല്ലാ ഗുരുക്കന്മാർക്കും നന്ദി.

ഈ വിജയത്തിനു പിന്നിൽ, ഞാൻ മറന്നുപോയേക്കാവുന്ന വാക്കുകളിലൂടെ എന്നെ പിന്തുണച്ച, സ്നേഹം നൽകിയ എല്ലാ സുഹൃത്തുക്കളോടും അഭ്യുദയകാംഷികളോടും ഞാൻ കടപ്പെട്ടിരിക്കുന്നു. ഞാൻ നേടിയ ഈ വിജയം, ഈ ജീവിതയാത്രയിൽ എന്നെ കൈപിടിച്ചുയർത്തിയ, എന്നെ സഹായിച്ച, എന്റെ കൂടെ നടന്ന ഓരോ വ്യക്തിയുടെയും സഹായത്തിന്റെ പ്രതിഫലനമാണ്. എന്റെ ഹൃദയത്തിൽ നിങ്ങൾക്കെല്ലാവർക്കും പ്രത്യേക സ്ഥാനമുണ്ട്.

This project has received funding from the European Union's Horizon 2020 research and innovation programme under the Marie Sklodowska-Curie grant agreement No.956396.

Résumé

Les conditions météorologiques aux latitudes moyennes présentent une variabilité basse fréquence (*low frequency variablility*, LFV) marquée, caractérisée par des configurations persistantes de circulation qui évoluent sur des échelles de temps bien plus longues que la limite de prévision typique de deux semaines. Une manifestation importante de cette LFV est la situation de blocage atmosphérique, dont l'établissement, le maintien et la dissipation influencent l'occurrence d'événements
météorologiques extrêmes tels que les vagues de chaleur, les vagues de froid, les sécheresses et les périodes prolongées de précipitations. Malgré des décennies d'études à ce propos, les blocages demeurent une source majeure d'incertitudes dans les prévisions en raison de leur dynamique non linéaire, de leur sensibilité aux conditions initiales et de leurs interactions fortes avec la circulation atmosphérique zonale et les perturbations synoptiques. L'objectif principal de cette thèse est d'examiner la variabilité et la prévisibilité des blocages atmosphériques à l'aide d'une hiérarchie de modèles d'ordre réduit et de modèles de circulation générale, afin d'améliorer la compréhension dynamique de la formation des blocages, de la manière dont leur stabilité dépend du contexte géographique.

Une première ligne de recherche utilise un modèle couplé atmosphère–sol quasi-géostrophique d'ordre réduit pour explorer comment le comportement des blocages émerge d'interactions dynamiques idéalisées. La réponse du modèle à des paramètres environnementaux clés, tels que la friction de surface et le forçage radiatif, a été analysée de manière systématique afin d'établir la structure des différents régimes. Des états zonaux, de transition et bloqués ont été identifiés, et leur stabilité a été quantifiée à l'aide des exposants de Lyapunov. Les résultats montrent que les régimes bloqués sont intrinsèquement plus instables que les mouvements zonaux, et que leur prévisibilité varie fortement selon la nature de l'orographie : les blocages formés en amont d'un relief sont systématiquement moins stables que ceux qui se formant en aval.

Pour tester si ces asymétries persistent dans un contexte plus réaliste, les blocages dans le Pacifique nord ont été analysés à partir des simulations quotidiennes du modèle MIROC6, faisant partie de CMIP6. Les événements de blocage ont été classés en régimes occidentaux et orientaux, et leur prévisibilité intrinsèque a été quantifiée à l'aide d'une approche d'analogues basée sur la croissance de l'erreur. Contrairement au modèle idéalisé, les blocages du Pacifique nord orientaux présentent une prévisibilité nettement

plus faible et une divergence d'erreur plus rapide, tandis que les blocages occidentaux sont relativement plus stables. La robustesse de ce résultat a été confirmée par des tests de sensibilité aux seuils de détection et la définition des analogues. Cette analyse a montré que la prévisibilité des blocages n'est pas uniquement dictée par les principes dynamiques idéalisés, mais est également influencée par la géométrie du bassin, la structure de l'écoulement moyen et l'activité des ondes transitoires.

Une analyse complémentaire a examiné les blocages sous un angle énergétique en étudiant l'énergie cinétique, l'énergie potentielle disponible et les anomalies de température de surface dans le modèle. Les interactions entre ces variables ont été quantifiées à l'aide des diagnostics du cycle énergétique de Lorenz et du calcul de transfert d'information. Les résultats révèlent que l'interaction entre les variables du cycle énergétique diffèrent sensiblement entre les blocages orientaux et occidentaux, entraînant des réponses atmosphériques distinctes pendant les périodes bloquées et non bloquées. L'analyse montre aussi que le comportement de l'influence entre les variables énergétiques, et pas seulement la stabilité de l'écoulement, contribuent aux différences régionales observées dans le comportement des blocages dans les modèles réalistes.

Enfin, pour recontextualiser plus largement les blocages par rapport aux dynamiques de basse fréquence, cette thèse a également examiné comment la structure du modèle et les interactions d'échelle influencent la variabilité. Des tests de sensibilité avec différentes résolutions ont mis en évidence la manière dont les systèmes d'ordre réduit peuvent présenter des comportements dynamiques qualitativement différents selon le nombre de modes spatiaux inclus. Cela souligne l'importance de choisir soigneusement la complexité du modèle lors de l'étude des blocages et de la LFV.

Pour résumer, cette thèse montre que la variabilité et la prévisibilité des blocages atmosphériques sont fortement modulés à la fois par la stabilité dynamique et par le contexte géographique, et que différentes hiérarchies de modèles révèlent des aspects complémentaires de ce comportement. Les résultats fournissent un cadre unifié pour comprendre les blocages dans des modèles à la fois idéalisés et de circulation générale, et posent les bases de futures recherches sur la manière dont les blocages et la LFV des moyennes latitudes pourraient évoluer et interagir avec les différentes composantes de l'atmosphère.

[1]

[1] La version française de ce résumé a été rédigée avec l'aide d'outils d'IA, puis relue et éditée manuellement.

Abstract

The weather in the midlatitudes exhibits pronounced low frequency variability (LFV), characterised by persistent circulation patterns that evolve on timescales far longer than the typical two week forecasting limit. A central expression of this LFV is atmospheric blocking, whose onset, maintenance, and decay influence the occurrence of extreme weather such as heatwaves, cold spells, droughts, and prolonged precipitation events. Despite decades of study, blocking remains a major source of forecast uncertainty due to its nonlinear dynamics, sensitivity to initial conditions, and strong interactions with the underlying mean flow and synoptic scale disturbances. The overarching aim of this thesis is to investigate the variability and predictability of blocking using a hierarchy of reduced order and comprehensive general circulation models, with the goal of improving dynamical understanding of how blocking emerges, how its stability depends on geographical context.

A first line of investigation employs a reduced order quasi geostrophic land - atmosphere coupled model to explore how blocking behaviour arises from idealised dynamical interactions. The model's response to key environmental parameters, such as surface friction and radiative forcing, was systematically analysed to establish its regime structure. Distinct zonal, transition, and blocked states were identified, and their stability was quantified using backward Lyapunov exponents. The results show that blocked regimes are inherently more unstable than zonal flows and that their predictability varies strongly with location relative to idealised topography: blocks forming upstream of the imposed orographic feature were systematically less stable than downstream ones. This mechanistic result highlights the importance of geographic positioning in shaping blocking behaviour.

To test whether such asymmetries persist in a more realistic context, blocking in the North Pacific was analysed using daily CMIP6 MIROC6 simulations. Blocking events were objectively classified into Western and Eastern regimes, and their intrinsic predictability was quantified through analogue based error growth. Contrary to the idealised model, Eastern North Pacific blocks displayed markedly lower predictability and faster error divergence, while Western blocks were comparatively more stable. The robustness of this result was confirmed through extensive sensitivity tests on detection thresholds and analogue definitions. This highlights that blocking predictability is not solely dictated by

idealised dynamical principles but is also shaped by realistic basin geometry, background flow structure, and transient eddy activity.

A complementary analysis examined blocking from an energetic viewpoint by quantifying interactions between kinetic energy, available potential energy, and near-surface temperature anomalies using Lorenz Energy Cycle diagnostics and an information transfer framework. These diagnostics reveal that the behavior of influence between energetic variables differ substantially between Eastern and Western blocking events, resulting in distinct atmospheric responses during blocked and non blocked periods. The results show that energetic pathways, and not only flow stability, contribute to the regional differences in blocking behaviour observed in realistic models.

Finally, to contextualise blocking within broader LFV dynamics, the thesis also examines how model structure and scale interactions influence variability. Sensitivity tests with altered model resolution highlighted how reduced order systems can exhibit qualitatively different dynamical behaviour depending on the number of spatial modes included. This underscores the importance of choosing model complexity carefully when studying blocking dynamics and LFV.

In the essence, this thesis demonstrates that atmospheric blocking variability and predictability are strongly modulated by both dynamical stability and geographical setting, and that different model hierarchies reveal complementary aspects of this behaviour. The results provide a unified framework for understanding blocking across idealised and comprehensive models, and they lay the groundwork for future studies on how blocking and midlatitude LFV more broadly may evolve and interact with different atmospheric components.

Contents

Contents **xiii**

List of abbreviations **xv**

1 Introduction **1**
1.1 Midlatitude Weather and the Role of Low-Frequency Variability 1
1.2 Atmospheric Blocking: Definition and Dynamics 8
1.3 Governing Equations of the Atmosphere 13
1.4 Hierarchy of Climate Models 18
1.5 Idealized Frameworks for Blocking 21
1.6 Nonlinear Dynamical Systems and Chaos 25
1.7 Thesis Outline 32

2 From Theory to Application: Technical Methods Used in this Thesis **35**
2.1 Land - Atmosphere Coupled Model 35
2.2 Lyapunov Exponents and the Growth of Perturbations in QG Systems . . 37
2.3 Predictability using Analogues 40
2.4 Liang - Kleeman Information Transfer Index: Theoretical Formulation . . 46
2.5 Application of the Liang - Kleeman Information Flow Index to Blocking Events 48

3 Variability and Predictability of a reduced-order land atmosphere coupled model **53**
3.1 Introduction and motivation 54
3.2 Land atmosphere coupled model 59
3.3 Methodology 63
3.4 Regime stability and Lyapunov properties of the low order land atmospheric coupled model 63
3.5 Predictability properties of zonal, blocking and transition flow regimes . . 71
3.6 Impact of model resolution 73
3.7 Discussions 75

4 Predictability of north Pacific blocking events : Analogue based analysis of historical MIROC6 simulations **77**
4.1 Introduction . . . 78
4.2 Data and Methodology . . . 79
4.3 Results and Discussion . . . 88
4.4 conclusion . . . 94

5 Beyond the mechanistic view of the Lorenz energy cycle of blocking events **97**
5.1 Introduction . . . 97
5.2 Data and Methodology . . . 99
5.3 Results and Discussions . . . 101
5.4 Conclusions . . . 105

6 Conclusions **107**
6.1 Specific Conclusions . . . 107
6.2 General Conclusions . . . 112
6.3 Future Perspectives . . . 114

A Appendix to Chapter 1 **117**
A.1 Gaussian Mixture Clustering (GMC) . . . 117
A.2 Examples of blocking and zonal patterns evolved from the study . . . 118

B Appendix to Chapter 2 **123**
B.1 Predictability analysis ($\alpha = 0.20$) . . . 123
B.2 Sensitivity test to analyze model dependence . . . 124

C List of Publications Related to the Thesis **127**

Bibliography **129**

List of abbreviations

APE	Available Potential Energy
BLV	Backward Lyapunov Vector
CMIP6	Coupled Model Intercomparison Project Phase 6
EOF	Empirical Orthogonal Function
ENP	Eastern North Pacific (blocking region)
GCM	General Circulation Model
GT	Ground Temperature
KE	Kinetic Energy
LE	Lyapunov Exponent
LEC	Lorenz Energy Cycle
LFV	Low Frequency Variability
LKIF	Liang - Kleeman Information Flow
MIROC6	Model for Interdisciplinary Research on Climate 6
MJO	Madden Julian Oscillation
NA	North America
NAO	North American Oscillation
NH	Northern Hemisphere
PNA	Pacific North American pattern
PDF	Probability Density Function
QGS	Quasi Geostrophic
R	Correlation Matrix
UPO	Unstable Periodic Orbit
WNP	Western North Pacific (blocking region)

Chapter 1

Introduction

1.1 Midlatitude Weather and the Role of Low-Frequency Variability

The middle latitudes, often called the temperate regions, cover the area between about 30° and 60° latitude in both the Northern and Southern Hemispheres. This wide band of the planet includes most of North America, Europe, and large parts of Asia, South America, and southern Australia. It is home to the majority of the world's population and many of its major cities and farmlands. The weather here is dynamic because it lies between the hot tropics and the cold polar regions. Warm, moist air from the subtropics often meets cold, dry air from the poles, creating an active zone where storms and fronts develop.

The climate in these regions changes strongly with the seasons. Summers are often warm with frequent movement of high and low pressure systems, while winters bring more storms, snow, and cold fronts. Because of the strong difference in temperature between north and south, the atmosphere strongly dependent of the horizontal temperature gradients. Fast-moving air currents called jet streams flow high above the ground, generally from west to east, steering weather systems across the continents.

The most common weather systems in the midlatitudes are the low-pressure systems known as cyclones and the high-pressure systems known as anticyclones. Cyclones are areas where warm and cold air meet and spiral around a center of low pressure, bringing clouds, rain, and wind. They are responsible for much of the rainfall and many of the storms in temperate regions. Anticyclones, on the other hand, bring calm and dry weather, often lasting for several days. Sometimes, a high-pressure system becomes stationary for a long period, blocking the usual west–east movement of storms. Such situations, called blocking events, can lead to long-lasting weather extremes like heatwaves, droughts, or cold spells.

Midlatitude weather is especially important because it affects the lives and economies of billions of people. Agriculture, transportation, and energy production all depend heavily on the weather conditions in these regions. A single severe storm can damage crops, disrupt air and sea transport, or cause flooding and power outages. Long-lasting dry or wet periods can have major impacts on water resources and food supply. The midlatitudes themselves are of immense socioeconomic importance, home to over half of the world's population and encompassing major urban centers, transportation networks, and agricultural zones across North America, Europe, and East Asia. These areas are especially susceptible to extreme weather events linked to atmospheric blocking. For instance, the 2003 European heatwave attributed to a persistent blocking high over Western Europe resulted in over 70,000 deaths and economic damages exceeding EUR 13 billion [Barriopedro et al., 2011; Miralles et al., 2014; Barriopedro et al., 2023]. Likewise, the February 2021 cold wave in Texas, associated with Arctic blocking and a weakened polar vortex, caused widespread energy infrastructure failures, more than 200 deaths, and economic losses surpassing USD 195 billion [ERCOT, 2021]. Understanding and predicting these weather systems helps governments and communities prepare for such events and reduce their risks. Accurate weather forecasts save lives, protect property, and help plan activities ranging from farming to renewable energy generation.

From a scientific point of view, the midlatitudes are one of the most interesting and complex parts of the atmosphere. They act as a mixing zone between the heat-surplus tropics and the heat-deficit polar regions. The energy that drives midlatitude weather mainly comes from the uneven heating of the Earth's surface by the Sun. Because the tropics receive more solar energy than the poles, there is a continuous attempt by the atmosphere to balance this difference by moving warm air poleward and cold air equatorward. This movement creates large-scale waves and storm systems that help transport heat, moisture, and momentum across the planet.

The strong temperature contrast between north and south is the main fuel for these weather systems. When this contrast becomes large enough, the atmosphere becomes unstable, and small disturbances can grow into large storms. This process converts potential energy stored in temperature differences into the kinetic energy of moving air. Moisture also plays a key role, as the release of heat during condensation can intensify these storms. The combined effect of wind, temperature gradients, and moisture makes the midlatitude atmosphere highly active and ever-changing.

Studying weather in the midlatitudes is therefore essential for both science and society. It helps scientists understand how the global circulation of the atmosphere works and how energy moves between different parts of the Earth. It also improves the ability to forecast extreme events, which are becoming more frequent and intense in a changing climate. Since most of the world's people live in these regions, better understanding of midlatitude weather patterns is directly linked to public safety, economic stability, and long-term sustainability.

In summary, the midlatitudes form a vital and lively part of the Earth's climate system. Here, tropical warmth meets polar cold, producing a constant interplay of storms, fronts,

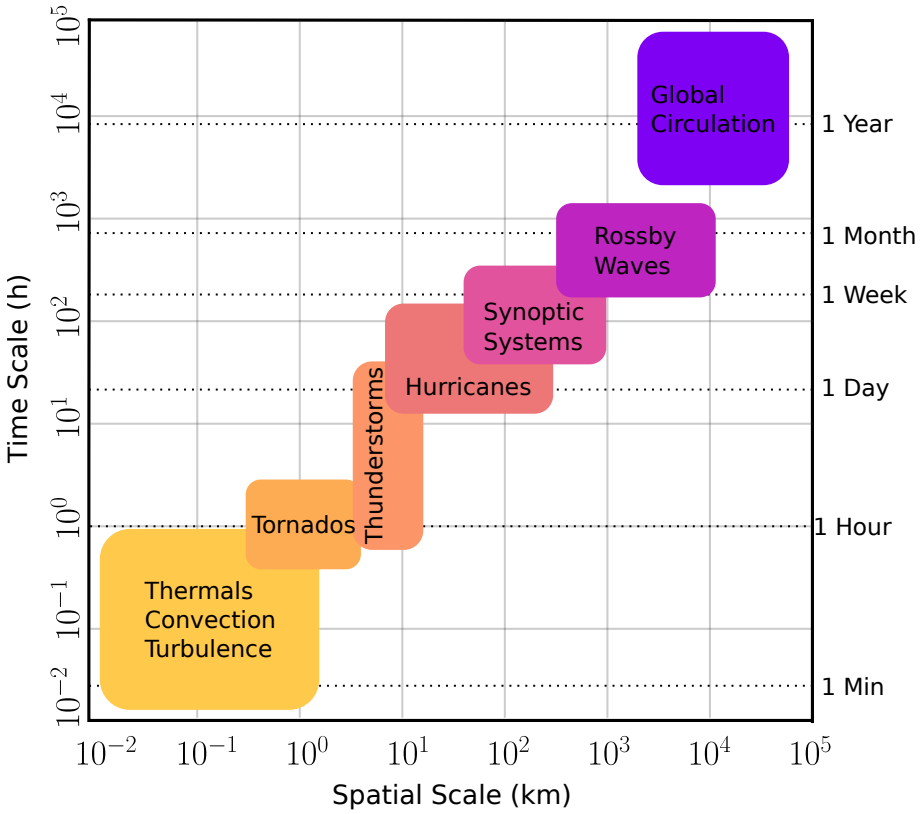


Figure 1.1: Different scales of atmospheric motion (Orlanski classification) (*Picture credit - Oisin Hamilton*) .

and pressure systems. This region's weather affects not only daily life but also global climate patterns. Studying how and why these systems form, move, and change gives us valuable insight into the workings of our planet and helps us prepare for the challenges of a changing world.

As shown in Figure 1.1, the atmosphere exhibits motion across a wide range of spatial and temporal scales. The figure, based on the Orlanski classification, provides a schematic view of how different types of atmospheric motions occupy distinct regions in the space time spectrum. On the horizontal axis are the spatial scales, ranging from a few kilometers to the entire globe, while the vertical axis represents the timescales of these phenomena, from minutes to years.

At the smallest scales lie turbulent eddies and convective updrafts, which operate over minutes and meters to kilometers. These give rise to localized weather phenomena such as thunderstorms and small cumulus clouds. Moving upward in scale, mesoscale systems

such as squall lines, sea breezes, and individual tropical cyclones (hurricanes) evolve over hours to days and extend across hundreds of kilometers.

At even larger scales lie the synoptic systems, typically spanning 1,000–3,000 km and lasting 2–7 days. These systems include extratropical cyclones, fronts, and anticyclones, which dominate the day-to-day weather variability in the midlatitudes. Beyond the synoptic scale, we enter the planetary or global scale, where long, slowly varying Rossby waves and the mean zonal circulation (the westerlies, subtropical jets, and polar vortices) govern the large-scale organization of the atmosphere over weeks to months.

While the synoptic scale captures the evolution of familiar weather systems such as storms, cold and warm fronts, and temperature fluctuations, not all atmospheric variability in the midlatitudes occurs so rapidly. The atmosphere also undergoes slower, more persistent changes on low-frequency timescales, typically ranging from 10 days to several weeks.

This slower component, known as low-frequency variability (LFV), represents the atmosphere's tendency to organize into large, quasi-stationary patterns that can dominate regional weather for extended periods. These include recurring circulation regimes and teleconnection patterns that influence surface temperature, precipitation, and storm tracks over vast regions. LFV manifests through persistent anomalies in the geopotential height, temperature, and wind fields, often organized as quasi stationary planetary waves or recurrent large-scale flow regimes [Wallace and Gutzler, 1981; Ghil and Robertson, 2002a]. Several well-known examples of low frequency variability include:

1. **The North Atlantic Oscillation (NAO):** The NAO represents the dominant pattern of low-frequency variability over the North Atlantic sector, particularly during winter. It is characterized by a *dipole* of atmospheric pressure anomalies between the Icelandic Low and the Azores High, illustrated in Figure 1.2. In its positive phase (fig1.2a), the pressure difference between these two centers is enhanced, leading to stronger westerlies, warmer and wetter conditions over northern Europe, and drier conditions over southern Europe. In the negative phase (fig1.2b), this gradient weakens or reverses, shifting storm tracks southward and producing colder winters in northern Europe and the eastern United States [Barnston and Livezey, 1987; Thompson and Wallace, 2000; Hurrell, 1995]. The two phases can thus be viewed as alternate circulation regimes within the Euro–Atlantic system.

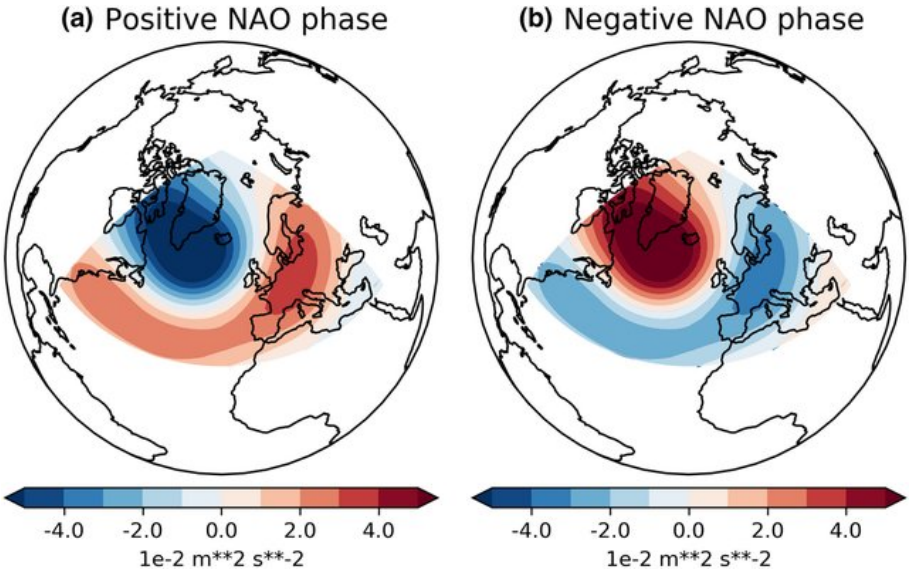


Figure 1.2: The positive (a) and negative (b) phases of the North Atlantic Oscillation (NAO), the dominant mode of wintertime atmospheric variability over the Euro–Atlantic region. The pattern shows a dipole of geopotential height anomalies at 500 hPa. Source: *Climate.gov, data from NCAR/NCEP*.

2. **The Pacific North American (PNA) Pattern:** The PNA is one of the most prominent teleconnection patterns in the Northern Hemisphere extratropics, influencing the path and intensity of storms across the North Pacific and North America. Figure 1.3 displays December–February mean 500 hPa geopotential height anomalies regressed onto the PNA index. The pattern consists of alternating centers of positive (orange) and negative (purple) pressure anomalies that extend from the subtropical Pacific toward western North America. A positive PNA phase is associated with a strengthened ridge over western Canada and a trough over the southeastern United States, leading to warm and dry conditions in the northwest and cooler, wetter weather in the southeast. The opposite holds for the negative phase [Leathers et al., 1991].

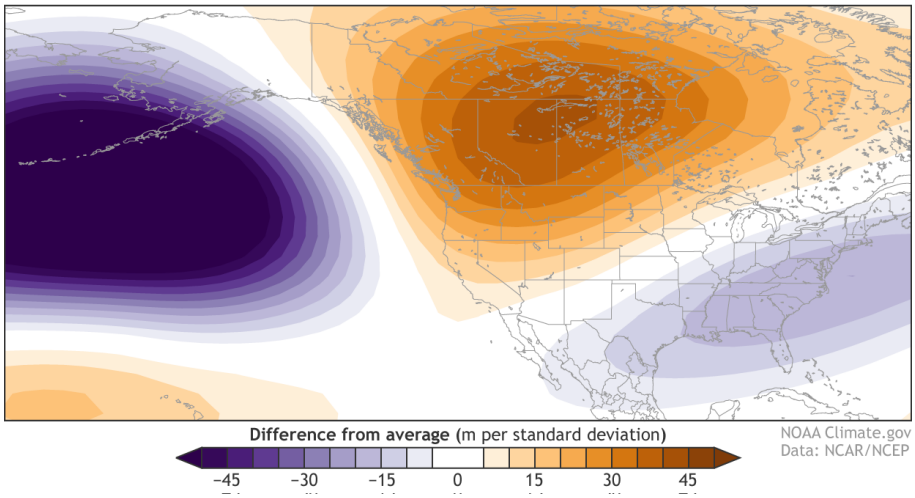


Figure 1.3: December to February 500 hPa geopotential height anomalies regressed onto the monthly PNA index (1979 - 2019). Purple shading indicates below-average pressure, while orange shading indicates above average pressure. Source: *NOAA Climate.gov, data from NCEP/NCAR reanalysis*.

3. **The Madden Julian Oscillation (MJO):** The MJO is a large-scale tropical disturbance that manifests as an eastward moving pattern of enhanced and suppressed convection, completing a full cycle in roughly 30 to 60 days. As depicted in Figure 1.4, the enhanced convective phase (green arrows) is associated with strong upward motion, clouds, and rainfall, while the suppressed phase (brown arrows) corresponds to sinking, drier air. The MJO influences global weather by modulating tropical rainfall and altering large-scale circulation patterns, including the frequency of Rossby wave breaking and storm activity in the extratropics [Cassou, 2008]. Its effects can extend to the midlatitudes, where it contributes to intraseasonal variability and modulates the occurrence of blocking events.

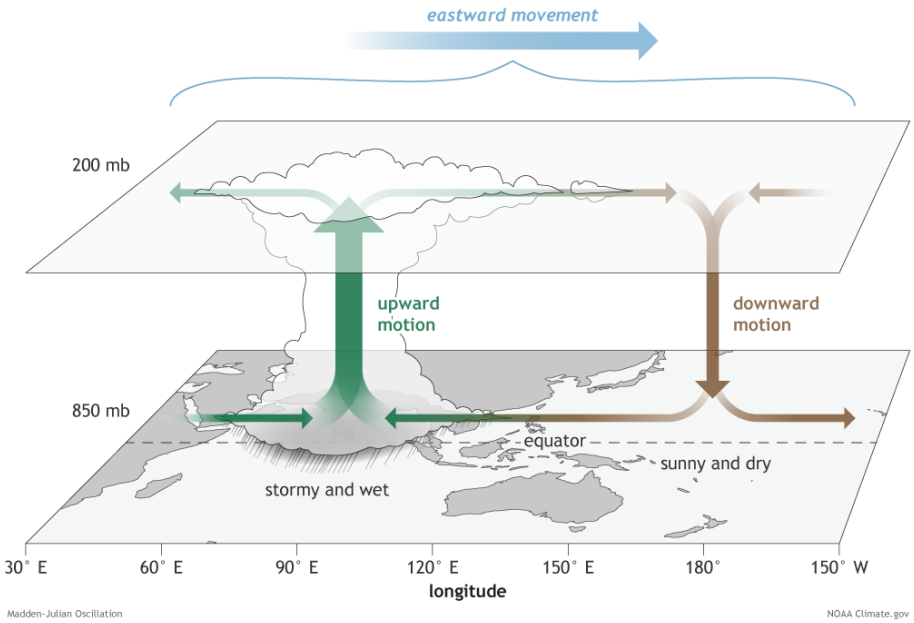


Figure 1.4: Schematic of the MJO showing upward motion (green) over the enhanced convective phase and downward motion (brown) over the suppressed phase. The system propagates eastward across the tropics, influencing rainfall and large-scale circulation. Source: *NOAA Climate.gov, illustration by Fiona Martin*.

Among all forms of low-frequency variability, one phenomenon stands out for its persistence and impact: atmospheric blocking. A blocking event occurs when a large, quasi-stationary high-pressure system disrupts the normal west-to-east flow of the atmosphere. These systems can "block" the progression of storms and lead to prolonged periods of unusual weather, such as heatwaves, cold spells, or droughts. Blocking is particularly interesting because it represents one of the distinct quasi-stable states of the atmosphere, alongside more zonal flow (straight west–east winds) and transitional regimes [Charney and DeVore, 1979].

Understanding blocking is essential because it plays a central role in how low-frequency variability shapes regional climate extremes. During a blocking episode, the usual flow of air masses is altered, leading to extended periods of abnormal temperature and precipitation.

Given its distinct dynamics and substantial impacts, atmospheric blocking provides a focused lens through which to examine LFV in midlatitudes. Its deviation from zonal flow patterns, statistical properties, and involvement in forecast uncertainty all warrant close investigation. The following section delves into the definition and climatology of blocking, highlighting its role in shaping circulation regimes and predictability challenges.

1.2 Atmospheric Blocking: Definition and Dynamics

Among the modes of LFV, atmospheric blocking stands out as one of the most influential and studied phenomena. Blocking refers to large-scale, quasi-stationary high-pressure systems that disrupt the midlatitude westerly flow for periods ranging from several days to weeks. These anomalies are typically identified at 500 hPa geopotential height and exhibit a reversal of the meridional geopotential gradient over a specified latitude band [Tibaldi and Molteni, 1990; Pelly and Hoskins, 2003].

Blocking systems exhibit three key characteristics: persistence, spatial coherence, and self maintenance through dynamical feedbacks. Multiple classification schemes have been developed to categorize blocking structures based on their geometry, dynamical evolution, and impact signatures. The most widely recognized morphological archetypes include:

1. **Rex Blocks:** Rex blocks consist of a high-pressure system positioned directly to the north of a low-pressure system, forming a meridional dipole structure. This configuration leads to strong meridional flow and effectively diverts the jet stream poleward and equatorward on either side of the block (Fig. 1.5). They are most common over the eastern Pacific and Atlantic basins, particularly during spring, and can persist for more than a week [Rex, 1950; Dole and Gordon, 1983].
   Case Example: Figure 1.5 illustrates a Rex block that recently developed over Europe. In this case, a strong anticyclone over central Europe aligned directly north of a closed low over North Africa, interrupting the usual westerly flow. The moist easterly flow on the southern flank of the block enhanced convection over the Mediterranean, producing heavy rainfall across Sicily, Sardinia, and parts of Calabria. Such configurations often result in hydrogeological hazards, underscoring the societal importance of understanding blocking dynamics.

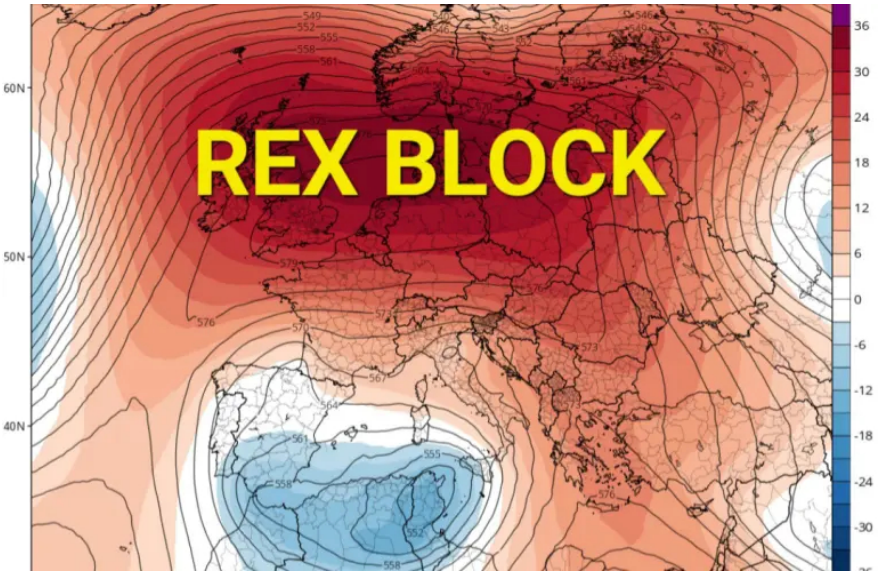


Figure 1.5: Example of a Rex block configuration over Europe, showing a high-pressure ridge over northern Europe positioned directly above a closed low over North Africa. The meridional dipole pattern effectively disrupts the zonal flow, resulting in persistent, anomalous weather conditions such as heavy rainfall in the Mediterranean region. Source: *NOAA/ECMWF reanalysis*.

2. **Omega Blocks:** Omega blocks derive their name from their resemblance to the Greek letter Ω, characterized by a central high-pressure ridge flanked by two low-pressure systems on either side (Fig. 1.6). These structures are among the most persistent forms of blocking, often lasting more than ten days and covering continental-scale areas [Tibaldi and Molteni, 1990; Barriopedro et al., 2011]. The central ridge region typically experiences prolonged clear and warm conditions, while the adjacent troughs bring unsettled and stormy weather.
   Case Example: Figure 1.6 presents a classic Omega block pattern over North America (GEFS 500 hPa geopotential height analysis). The pattern shows two deep troughs along both coasts with a strong ridge across the central United States, leading to simultaneous heat and drought in the center and heavy precipitation along the coasts.

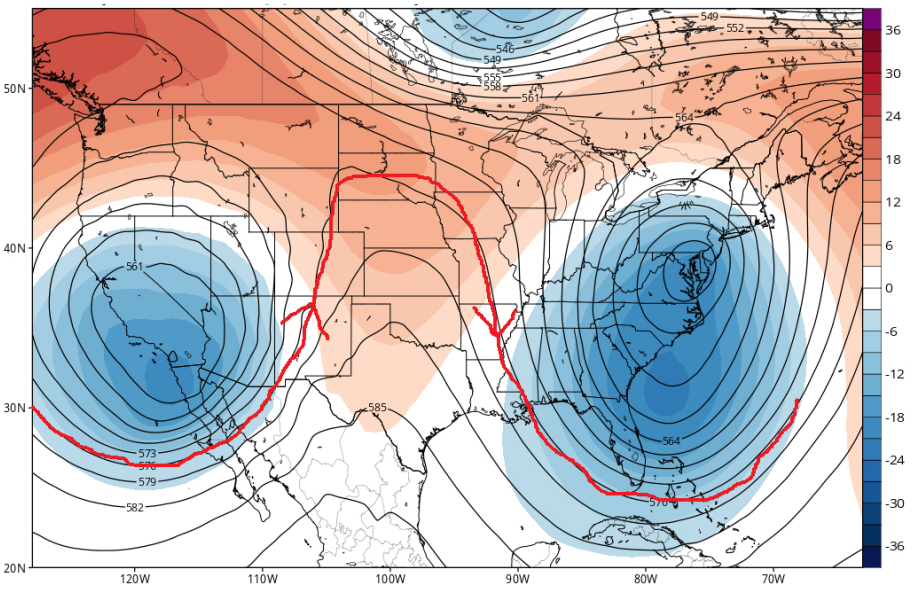


Figure 1.6: Classic Omega block pattern at 500 hPa, featuring a high-pressure ridge centered over the central United States flanked by two troughs on the east and west coasts. This configuration resembles the Greek letter Ω and produces contrasting weather conditions across the continent. Source: *TropicalTidbits.com, NOAA GEFS data*.

3. **Dipole-Type Blocks:** Dipole-type blocks, such as the well-known Scandinavian blocks, are characterized by a strong high-pressure anomaly adjacent to a deep low-pressure anomaly. They often emerge from large-scale wave breaking and can significantly influence regional climates depending on their orientation and position [Nakamura and Huang, 2018]. These blocks can induce prolonged cold spells over one region and persistent warmth over another, especially during winter, by rerouting the jet stream and altering storm tracks.
4. **Zonal Ridge Blocks:** Zonal ridge blocks, or elongated ridge patterns, are more transient than Rex or Omega blocks but still play a critical role in slowing synoptic-scale weather systems. They are characterized by an extensive ridge without closed geopotential height contours (i.e., open structures) that temporarily stall the eastward progression of disturbances [Sousa et al., 2018]. Although less geometrically distinct, they are often precursors to the development of stronger, more persistent blocking regimes.

While the classification of blocking types provides a morphological understanding, it is equally important to examine the physical processes that govern their formation and persistence. Recent studies also differentiate blocks based on their dynamical genesis mechanisms, such as cyclonic versus anticyclonic Rossby wave breaking [Masato et al.,

2012], or their temporal life cycle characteristics, including onset, maintenance, and decay phases [Davini et al., 2012]. Beyond dynamical genesis, the identification of blocking events itself is subject to methodological divergence. Classical methods use reversal of the meridional gradient in geopotential height at 500 hPa [Tibaldi and Molteni, 1990], while potential vorticity (PV)-based diagnostics identify coherent anomalies in PV on isentropic surfaces ([Schwierz et al., 2004a; Pelly and Hoskins, 2003]. Other approaches employ finite-amplitude wave activity to capture wave-mean flow interactions associated with blocking [Nakamura and Huang, 2018]. Hybrid techniques, such as those integrating dynamical criteria with anomaly persistence thresholds, are increasingly used to ensure physical consistency and robustness across datasets and models [Davini et al., 2012; Barnes et al., 2012]. These refined classifications and definitions provide a multifaceted framework for understanding blocking variability and assessing its predictability in both observations and model simulations.

The persistence of atmospheric blocking is not solely determined by large-scale dynamical processes; moisture feedbacks and diabatic heating play a crucial reinforcing role in maintaining these quasi-stationary anomalies. Moisture transport from lower latitudes toward the blocking region enhances latent heat release through condensation within cloud systems, which in turn strengthens the upper-tropospheric ridge and stabilizes the flow pattern [Pfahl et al., 2015; Steinfeld et al., 2020]. Such diabatic amplification effectively increases the equivalent potential temperature within the blocked air mass, reducing baroclinicity locally and thereby inhibiting the growth of transient eddies that could otherwise erode the block [Müller and Roeckner, 2015; Nie and Sobel, 2021]. Moreover, atmospheric rivers and warm conveyor belts can supply sustained moisture flux convergence into the blocking anticyclone, further reinforcing the anomaly through latent heating and potential vorticity modification in the upper troposphere [Martius et al., 2013; Pfahl and Wernli, 2014]. These processes create a two-way interaction in which blocking modulates moisture transport, while the resulting latent heat release acts to prolong the block's lifetime. Consequently, moisture dynamics constitute an essential component of the maintenance and decay mechanisms of blocking, particularly in summer when diabatic processes are most active [Trigo and DaCamara, 2004; Davini and D'Andrea, 2017].

When a blocking system establishes itself, the associated high-pressure region alters the local balance of forces in the atmosphere. The subsiding air within the anticyclone suppresses cloud formation and leads to radiative warming at the surface [Drouard and Woollings, 2018]. The pressure gradient force weakens locally, and the zonal wind component diminishes, often inducing a split or diversion of the jet stream [Nakamura and Huang, 2018]. This deflection of westerly flow enhances the meridional transport of air masses, facilitating the intrusion of warm or cold anomalies into midlatitudes depending on the block's orientation and location. The persistence of such configurations is often reinforced by feedback mechanisms involving radiative heating, soil moisture depletion, and suppressed boundary layer mixing [Nakamura and Huang, 2018; Shutts, 1983; Woollings et al., 2018].

Climatologically, blocking episodes preferentially occur over certain "hotspots" in the Northern Hemisphere, notably the North Atlantic, North Pacific, and Eurasian sectors

[Barriopedro et al., 2006]. These regions are associated with stationary planetary waves, topographic forcing, and strong land-ocean thermal gradients. For instance, blocking over the North Pacific often occurs near the Aleutian low and influences downstream weather over North America [Lupo and Bosart, 1999], while North Atlantic blocking is closely linked to cold spells and snow events in Europe [Sillmann et al., 2011; Whan et al., 2016].

The societal relevance of blocking arises from its role in anchoring extreme weather conditions. In summer, blocking promotes heatwaves and drought through large-scale subsidence, radiative warming, and soil-moisture feedbacks [Pfahl and Wernli, 2012; Miralles et al., 2019] . During winter, cold spells develop downstream or south of blocking highs due to enhanced meridional advection of polar air [Trigo et al., 2004; Brunner et al., 2018].

Historical events underline this connection. The 2010 Russian heatwave, which led to over 55,000 deaths and widespread wildfires, was associated with a persistent Omega block over western Russia [Barriopedro et al., 2011; Lau and Kim, 2012]. Conversely, the February 2012 cold spell in Europe, linked to North Atlantic blocking, resulted in over 650 fatalities and significant disruption to transport and energy infrastructure [Kautz et al., 2021].

Blocking not only modulates local extremes but also influences hemispheric circulation via teleconnections. For example, Pacific blocking events can shift the PNA pattern, altering the storm track across North America [Dole and Gordon, 1983; Henderson et al., 2016; Henderson and Maloney, 2018]. Such interactions contribute to compound and remote extremes, as seen in the simultaneous Russian heatwave and Pakistan flooding of 2010 [Kornhuber et al., 2020].

Despite its significance, atmospheric blocking remains a major challenge for numerical weather prediction (NWP) and climate models. Many models underestimate the frequency, persistence, and amplitude of blocking events, particularly over Europe [Davini and d'Andrea, 2020]. These biases arise from difficulties in representing key physical processes such as Rossby wave breaking, diabatic interactions, and stratosphere troposphere coupling [Ferranti et al., 2015; Matsueda and Palmer, 2018].

Efforts to improve the representation of blocking have focused on increasing model resolution, refining ensemble forecasting methods, and developing better diagnostic metrics. Ensemble prediction systems have shown some success in capturing the onset of blocking when certain flow configurations are present, especially when influenced by tropical forcing or stratospheric precursors [Rodwell et al., 2013; Athanasiadis et al., 2014]. Nevertheless, transitions into and out of blocking remain difficult to forecast beyond 5 to 7 days, which limits operational predictability [Hamill and Kiladis, 2014].

From a dynamical systems perspective, blocking represents a distinct regime of the atmosphere characterized by low local stability. This does not contradict the fact that blocking events can persist for more than ten days in a fixed geographical location. Meteorologically, the persistence of blocking refers to its ability to maintain a quasi-stationary pattern that disrupts the normal west - east progression of weather systems, often re-

sulting in prolonged extremes such as heatwaves or cold spells. Dynamically, however, the blocked state is *unstable and chaotic*, meaning that small perturbations in the initial conditions grow rapidly in time. In such a regime, errors in model initialization or in the representation of key processes amplify faster than in the zonal flow, thereby limiting forecast skill and predictability.

Studies based on Lyapunov exponents and analogue techniques confirm this distinction: blocking states, while persistent in space and time, exhibit higher local instability compared to zonal regimes, particularly in regions prone to wave breaking [Faranda et al., 2016, 2017; Lucarini and Gritsun, 2020; Xavier et al., 2024]. This dual nature 'long-lived yet dynamically fragile' explains why blocking remains both an essential feature of midlatitude climate variability and one of the most challenging phenomena to predict accurately.

To rigorously analyze the dynamics and persistence of blocking events, it is therefore essential to first determine and characterize the fundamental equations that govern atmospheric motion across scales.

1.3 Governing Equations of the Atmosphere

1.3.1 Structure and Physical Characteristics of the Atmosphere

The Earth's atmosphere is a multilayered, compressible, and rotating fluid system composed primarily of nitrogen (approximately 78%), oxygen (21%), and trace gases such as water vapor, carbon dioxide, methane, and ozone [Peixoto and Oort, 1992; Wallace and Hobbs, 2006]. It extends vertically from the surface up to several hundred kilometers, though about 90% of its total mass is concentrated within the lowest 16 kilometers. The vertical structure of the atmosphere is divided into distinct layers based on temperature variations with height, as illustrated in Figure 1.7. These layers, the troposphere, stratosphere, mesosphere, thermosphere, and exosphere exhibit characteristic temperature gradients and physical processes.

The lowest layer, the *troposphere* (0 - 12 km), contains most of the atmospheric mass and water vapor, and it is where turbulent mixing, weather systems, and latent heat exchanges dominate. Above it lies the *stratosphere* (12 - 50 km), where temperature increases with height due to ozone absorption of ultraviolet radiation. The *mesosphere* (50 - 85 km) marks a region of decreasing temperature and is where meteors burn up upon entry. The *thermosphere* (85 - 690 km) experiences strong temperature increases as molecules absorb high energy solar radiation, while the *exosphere* (above $\sim$700 km) gradually transitions into outer space. Together, these layers form a complex and dynamic system that governs the exchange of energy, momentum, and mass between the Earth's surface and space.

Given the relatively small vertical scale compared to Earth's radius (6371 km), the atmosphere is often treated using the shallow-atmosphere approximation, where curvature effects are incorporated in horizontal dynamics, but the vertical coordinate is simplified

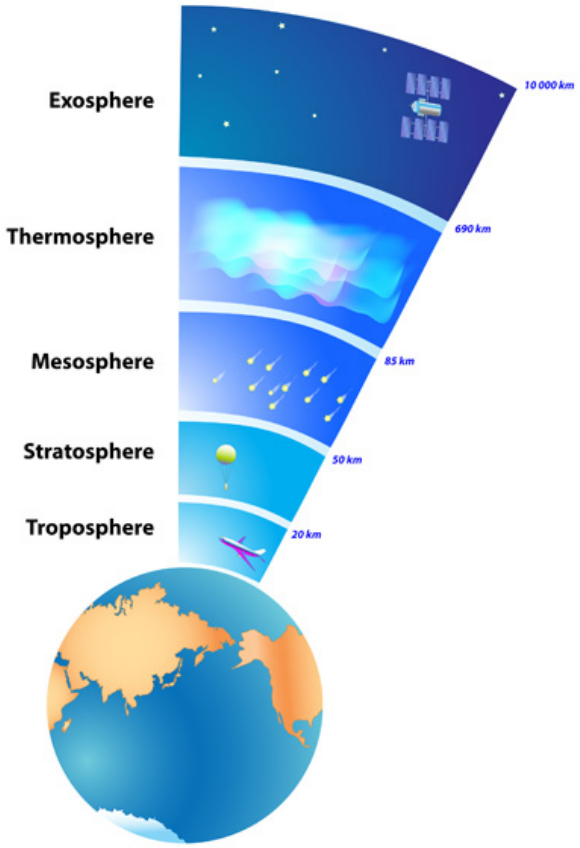


Figure 1.7: Schematic representation of the vertical structure of the Earth's atmosphere. The major layers, troposphere, stratosphere, mesosphere, thermosphere, and exosphere are defined based on temperature gradients and dominant physical processes.

[Holton and Hakim, 2012]. Earth's rotation introduces the Coriolis force, which significantly impacts large-scale geophysical flows, promoting the formation of organized structures such as Rossby waves and mid-latitude cyclones [Vallis, 2017].

From a dynamical systems perspective, the atmosphere evolves in response to both external forcings (e.g., solar radiation, topography, ocean-atmosphere interaction) and internal physical laws. The motion of atmospheric parcels is governed by the laws of fluid dynamics adapted for a rotating, stratified environment. These laws are expressed via a set of equations commonly referred to as the primitive equations, which form the foundation for general circulation models (GCMs) and weather prediction systems.

1.3.2 Primitive Equations and Conservation Principles

The *Navier Stokes equations* describe the motion of a compressible, viscous fluid and serve as the governing equations for atmospheric dynamics. In a rotating reference frame, they are expressed as:

$$\frac{D\mathbf{v}}{Dt} \; + \; 2\boldsymbol{\Omega} \times \mathbf{v} \; = \; -\frac{1}{\rho}\,\nabla p \; + \; \mathbf{g} \; + \; \mathbf{F}_{\text{visc}}. \tag{1.1}$$

where $\vec{v}$ is the three-dimensional velocity vector, $\vec{\Omega}$ is the angular velocity of Earth's rotation, p is pressure, ρ is air density, $\vec{g}$ is the gravitational acceleration, and $\vec{F}_{\text{visc}}$ represents viscous forces. When combined with the thermodynamic energy equation and the equation of state for an ideal gas, this system forms the basis of comprehensive atmospheric models.

To make these equations more tractable for large-scale atmospheric motions, a set of simplifying assumptions is applied. Chief among these are hydrostatic balance in the vertical direction (neglecting vertical acceleration), and approximations such as the Boussinesq or anelastic formulations to handle weak compressibility. Under these conditions, the full Navier–Stokes system reduces to the so-called *primitive equations* [Gill, 1982; Kalnay, 2003].

For practical and computational efficiency, these equations are typically reformulated in pressure coordinates, where pressure serves as the vertical coordinate. This choice is motivated by the nearly exponential decrease of pressure with altitude and the alignment of isobaric surfaces with stratified atmospheric processes, thereby improving the representation of thermodynamic and dynamical interactions in general circulation models.

The horizontal momentum equations describe the evolution of wind components (u, v) under the influence of pressure gradients, the Coriolis force, and frictional processes. In the zonal and meridional directions, these can be written as:

$$\frac{Du}{Dt} - fv = -\frac{\partial \Phi}{\partial x} + F_u, \tag{1.2}$$

$$\frac{Dv}{Dt} + fu = -\frac{\partial \Phi}{\partial y} + F_v, \tag{1.3}$$

where $f = 2\Omega \sin\phi$ is the Coriolis parameter (with Ω being the Earth's rotation rate and ϕ the latitude), Φ is the geopotential, and F_u, F_v are frictional terms representing subgrid-scale processes such as boundary layer turbulence or gravity wave drag. The total derivative $\frac{D}{Dt}$ accounts for local and advective changes in velocity. These equations demonstrate how horizontal accelerations are dictated by the balance of Coriolis and pressure gradient forces, often approximated as geostrophic balance at synoptic scales.

Vertical momentum is simplified via the hydrostatic approximation, which assumes that vertical accelerations are negligible compared to the pressure gradient force and

gravity. This leads to the hydrostatic equation:

$$\frac{\partial \Phi}{\partial p} = -\alpha = -\frac{RT}{p}, \tag{1.4}$$

where α is the specific volume, R is the specific gas constant for dry air, and T is temperature. This relation implies that the vertical distribution of geopotential is directly linked to temperature stratification, a cornerstone in atmospheric thermodynamics and height field analysis.

The conservation of mass in a compressible atmosphere is captured by the continuity equation. In pressure coordinates, this becomes:

$$\frac{\partial u}{\partial x} + \frac{\partial v}{\partial y} + \frac{\partial \omega}{\partial p} = 0, \tag{1.5}$$

where $\omega = \frac{Dp}{Dt}$ is the vertical velocity in pressure coordinates. This form ensures that convergence or divergence in horizontal winds is accompanied by compensating vertical motion, maintaining the total mass budget of the system. This continuity constraint is essential for the development of vertical circulations such as Hadley cells or midlatitude ascent/descent in frontal systems.

The thermodynamic energy equation governs the evolution of temperature and accounts for both adiabatic and diabatic processes:

$$\frac{DT}{Dt} - \frac{\kappa T}{p}\,\omega = \frac{Q}{c_p}, \tag{1.6}$$

where D/Dt is the material derivative following an air parcel, T is temperature, p is pressure, $\omega \equiv Dp/Dt$ is the vertical velocity in pressure coordinates (Pa s^{-1}; negative for ascent), Q is the diabatic heating rate per unit mass (W kg^{-1}), c_p is the specific heat at constant pressure, R is the gas constant for dry air, and $\kappa \equiv R/c_p$. The equation quantifies how a parcel warms under adiabatic compression ($\omega > 0$) or cools under expansion ($\omega < 0$), and how external heating/cooling (Q) further modifies T. It is central to three standard diagnostics: (i) the *lapse rate* $\Gamma \equiv -\partial T/\partial z$ (with the dry-adiabatic value $\Gamma_d = g/c_p$ and a smaller moist-adiabatic lapse rate when condensation releases latent heat); (ii) *static stability*, commonly measured by the vertical gradient of potential temperature $\theta = T(p_0/p)^{\kappa}$ or the Brunt–Väisälä frequency $N^2 = (g/\theta)\,\partial\theta/\partial z$ ($N^2 > 0$ stable, $N^2 < 0$ unstable); and (iii) the *energetics of convection and storm development*, often summarized by the convective available potential energy (CAPE) and convective inhibition (CIN), e.g.

$$\mathrm{CAPE} = \int_{\mathrm{LFC}}^{\mathrm{EL}} \frac{g\,[\theta_{v,p} - \theta_{v,e}]}{\theta_{v,e}}\,dz, \quad \mathrm{CIN} = -\int_{z_s}^{\mathrm{LFC}} \frac{g\,[\theta_{v,p} - \theta_{v,e}]}{\theta_{v,e}}\,dz,$$

where θ_v is virtual potential temperature (subscripts p and e denote parcel and environment), z_s is the surface level, LFC is the level of free convection, and EL is the equilibrium level. These quantities depend directly on the adiabatic term and on diabatic heating Q, which together regulate parcel buoyancy and stability.

The system is closed with the equation of state for an ideal gas:

$$p = \rho RT, \tag{1.7}$$

which links pressure (p), density (ρ), and temperature (T), and enables the conversion between thermodynamic variables. This relation is fundamental to all meteorological analyses and model formulations, as it connects dynamic fields with thermodynamic diagnostics.

In addition to these dynamical equations, the laws of conservation underpin the entire atmospheric system. Mass conservation, as previously noted, is intrinsic to the continuity equation. Momentum conservation arises from Newton's second law applied to a rotating reference frame, where forces such as gravity, pressure gradients, and friction determine the evolution of wind fields. These principles enable the study of wave motions, vorticity dynamics, and large-scale circulation patterns.

Energy conservation, often expressed through the first law of thermodynamics, tracks the exchange between kinetic, potential, and internal energy. For a parcel of dry air, this is often written in differential form as:

$$\frac{dQ}{dt} = c_p \frac{dT}{dt} - \frac{\alpha}{\rho} \frac{dp}{dt}, \tag{1.8}$$

which distinguishes between diabatic heating and work done by expansion or compression. This framework allows one to derive conserved quantities such as dry static energy or moist static energy in the presence of latent heating.

A particularly important quantity in geophysical fluid dynamics is potential vorticity (PV), which integrates conservation of angular momentum and stratification:

$$PV = \frac{\boldsymbol{\omega}_a \cdot \nabla\theta}{\rho}, \tag{1.9}$$

where $\boldsymbol{\omega}_a$ is the absolute vorticity and θ is the potential temperature. Under adiabatic and frictionless conditions, PV is materially conserved, making it a powerful tracer for atmospheric dynamics, wave breaking, and stratosphere-troposphere exchange processes [Andrews et al., 1987]. It serves as the foundation for quasi-geostrophic theory, baroclinic instability diagnostics, and potential vorticity inversion methods.

Collectively, the primitive equations represent a mathematically consistent and physically comprehensive framework for atmospheric modeling. Their simplifications using hydrostatic balance, traditional approximations, pressure coordinates, strike a balance between computational feasibility and physical fidelity. These equations are typically closed by assuming a parameterization of unresolved physical processes such as turbulence, radiation, convection, and cloud microphysics [Washington and Parkinson, 2005; Stephens, 2005]. Numerical weather prediction models and Earth system simulators employ discretized forms of these equations to capture phenomena from mesoscale convection to planetary scale wave dynamics. Their central role in climate and weather sciences underscores the continued importance of theoretical development, parameterization, and high performance computing in advancing atmospheric research.

1.4 Hierarchy of Climate Models

The mathematical formulation of the primitive equations provides the foundation upon which a wide hierarchy of climate models is constructed. These models vary in complexity, resolution, and the range of physical processes included. The appropriate level of complexity depends on the scientific objectives, the spatial and temporal scales of interest, and computational constraints. Broadly, this hierarchy ranges from comprehensive Earth System Models (ESMs) to highly reduced low-order dynamical systems, each serving a distinct purpose in climate research [Held, 2005].

1.4.1 General Circulation Models (GCMs)

At the most comprehensive level, *General Circulation Models* (GCMs), or fully coupled Earth System Models (ESMs), are designed to simulate the full spectrum of physical, chemical, and biological interactions within the Earth system. These models numerically integrate the primitive equations on a global grid, incorporating the atmosphere, ocean, land surface, cryosphere, and biogeochemical cycles using discretization in both space and time. To represent unresolved subgrid-scale processes, GCMs employ advanced parameterizations for convection, boundary layer turbulence, radiative transfer, and cloud microphysics [Washington and Parkinson, 2005; Hourdin et al., 2013]. These comprehensive models serve as the core tools for climate change projection, climate sensitivity estimation, and detection and attribution of anthropogenic signals. Notable examples include the NASA GISS ModelE [Schmidt et al., 2014], the NCAR Community Earth System Model (CESM) [Hurrell et al., 2013], the MPI-ESM developed by the Max Planck Institute [Giorgetta et al., 2013], and the ECMWF Integrated Forecasting System (IFS) [Haiden et al., 2019].

A central framework for organizing and comparing GCM simulations is the Coupled Model Intercomparison Project (CMIP), which standardizes experimental protocols across modeling centers. The sixth phase, *CMIP6*, comprises an ensemble of over 100 models participating in coordinated experiments to assess model performance, climate responses to various forcings, and inter-model uncertainties [Eyring et al., 2016]. CMIP6 provides a foundational dataset for IPCC assessments and is widely used for multi-model ensemble analysis of future climate projections, internal variability, and process-based evaluation.

To complement the theoretical foundations discussed earlier, this thesis incorporates simulations from a comprehensive general circulation model. Specifically, we employ *MIROC6*, a state of the art CMIP6 model developed collaboratively by the Japan Agency for Marine-Earth Science and Technology (JAMSTEC), the University of Tokyo, and the National Institute for Environmental Studies. *MIROC6* is particularly well-suited for studying midlatitude dynamics and blocking behavior [Lohmann and *et al.*, 2024], as it offers notable improvements over its predecessors [Tatebe et al., 2019b]. The model features a T85 spectral resolution and 81 vertical levels reaching into the mesosphere, enabling finer representation of upper-atmospheric processes. Enhancements in the physical parameterizations, including updated radiative transfer schemes, a prognostic aerosol

model, and improved treatment of non-orographic gravity wave drag, contribute to a more accurate simulation of cloud-aerosol interactions, stratosphere–troposphere coupling, and large-scale circulation patterns [Tatebe et al., 2019b; Watanabe et al., 2010]. These capabilities make *MIROC6* a robust platform for analyzing the predictability and variability of atmospheric blocking, as presented in Chapter 4.

MIROC6 has demonstrated notable improvements in the simulation of blocking events, jet variability, and Rossby wave dynamics, a phenomena that are particularly relevant to this study [Tatebe et al., 2019b; Lohmann and *et al.*, 2024; Davini and D'Andrea, 2020]. Its ability to resolve stratospheric influences and upper-tropospheric flow anomalies makes it a robust tool for diagnosing large-scale circulation regimes. In this work, historical daily output from the MIROC6 (1850–2014) simulations are used to investigate the representation and predictability of atmospheric blocking patterns, particularly over the North Pacific sector, as elaborated in Chapter 4.

1.4.2 Intermediate Complexity Models (ICMs)

To reduce computational cost while retaining essential dynamics, *Intermediate Complexity Models* (ICMs) simplify either the spatial resolution, physical processes, or the number of model components. These include models like SPEEDY (Simplified Parameterizations, primitivE-Equation DYnamics) [Kucharski et al., 2013], which retains primitive-equation dynamics with simplified physics. ICMs are well-suited for long-term integrations, paleoclimate reconstructions, and ensemble sensitivity analyses.

1.4.2.1 Quasi-Geostrophic (QG) Models

At a more idealized level, *Quasi-Geostrophic* (QG) models provide the theoretical backbone for understanding midlatitude atmospheric dynamics. They are derived from the primitive equations under the assumptions of small Rossby number, hydrostatic balance, and near-geostrophic equilibrium. These approximations filter out fast gravity waves and retain the slower, rotational motions that dominate large-scale weather systems. The central governing equation expresses the conservation of quasi-geostrophic potential vorticity (PV):

$$\frac{Dq}{Dt} = \frac{\partial q}{\partial t} + \mathbf{u}_g \cdot \nabla q = F - D, \tag{1.10}$$

where q is the quasi-geostrophic potential vorticity, $\mathbf{u}_g$ the geostrophic velocity, F represents external or diabatic forcing, and D denotes dissipative effects such as friction or diffusion.

The operator $\frac{D}{Dt}$ is the *material derivative*, describing the rate of change of q following the geostrophic flow. The term $\frac{\partial q}{\partial t}$ represents the local (temporal) rate of change of PV at a fixed point, while $\mathbf{u}_g \cdot \nabla q$ represents the horizontal advection of PV by the geostrophic wind. The geostrophic velocity is defined from the streamfunction ψ as $\mathbf{u}_g = \hat{\mathbf{k}} \times \nabla_H \psi$, meaning that the flow is nondivergent and parallel to isobars. In the absence of forcing and dissipation ($F = D = 0$), PV is materially conserved air parcels retain their PV as they move.

In a multi-layer QG model, potential vorticity is computed at each pressure level (200, 500, and 800 hPa) as a combination of three contributions: (i) the *relative vorticity* of the flow, which measures local rotation; (ii) the *planetary vorticity gradient*, often referred to as the β-effect, arising from the variation of the Coriolis parameter with latitude; and (iii) a *baroclinic term* that depends on vertical shear and stratification. The lower boundary can also include an additional term representing the influence of topography on PV.

The QG system is often written in the compact form

$$\frac{\partial q_i}{\partial t} + J(\psi_i, q_i) = -\mathcal{D}_i[\psi] + \mathcal{S}_i, \tag{1.11}$$

where the subscript i denotes the model level ($i = 1, 2, 3$), $J(A, B)$ is the horizontal Jacobian operator describing advection, $\mathcal{D}_i$ represents damping and diffusion processes, and $\mathcal{S}_i$ is a prescribed forcing term that drives a statistically steady climate state.

The operator $\mathcal{D}_i[\psi]$ typically includes:

- **Newtonian temperature relaxation**, which restores large-scale temperature anomalies toward a reference profile;
- **Scale-selective horizontal diffusion**, which removes small-scale noise and enforces numerical stability; and
- **Linear surface drag** applied at the lowest model level to represent frictional dissipation.

These processes together ensure a physically realistic balance between energy input, transfer, and dissipation within the model.

In Equation (1.11), the first term on the left-hand side $\partial q_i/\partial t$ expresses the temporal evolution of potential vorticity at level i, while $J(\psi_i, q_i)$ captures the nonlinear advection of PV by the geostrophic flow. The right-hand side terms govern how external forcing ($\mathcal{S}_i$) and damping ($\mathcal{D}_i$) modify the natural dynamics of the flow.

QG models, despite their simplicity, reproduce many of the key features of midlatitude circulation such as baroclinic instability, Rossby-wave propagation, and eddy–mean flow interaction [Holton and Hakim, 2012; Vallis, 2017]. They also provide an essential framework for exploring regime transitions, variability of the jet stream, and the formation and decay of atmospheric blocking [Charney and Straus, 1980]. Through controlled experiments, they offer a clear link between theory and the complex behaviors observed in full general circulation models.

1.4.3 Low-order models

Further simplification leads to *low-order idealized models*, which are typically derived through techniques such as Galerkin projection or Fourier mode truncation of more complex systems like the quasi-geostrophic or shallow water equations. These models reduce the system to a small set of ordinary differential equations, enabling focused exploration

of fundamental dynamical behaviors such as nonlinearity, bifurcations, multiple equilibria, and chaotic regimes. A well-known example is the Lorenz system [Lorenz, 1963b], originally developed to study atmospheric convection, which despite its simplicity exhibits deterministic chaos and has become a cornerstone in the study of predictability and sensitivity to initial conditions in climate dynamics [Lorenz, 1963b].

Other low order frameworks, such as the Modular Arbitrary Order Ocean Atmosphere Model (MAOOAM) [De Cruz et al., 2016], represent both atmospheric and oceanic components in a spatially truncated setup, allowing the investigation of coupling mechanisms, variability, and energy cascades. Such models are often employed for stochastic parameterization testing, Lyapunov spectrum computation, and data-driven model reduction [Vallis, 2017].Low-order models also include *conceptual coupled systems* that link the atmosphere to simple land as well through energy or mass exchange (e.g., slab ocean or soil moisture dynamics)[Li et al., 2018; Xavier et al., 2024]. These models are invaluable for exploring feedbacks such as land-atmosphere coupling, surface heat flux variability, or moisture convection interactions [d'Andrea et al., 2006]. Due to their transparency and tractability, these models are particularly well-suited for regime analysis, bifurcation theory, and the study of intrinsic low-frequency variability.

Altogether, the hierarchy of climate models from high resolution Earth system simulators to idealized dynamical systems constitutes a powerful toolkit for climate science. While comprehensive models offer quantitative forecasts, idealized models offer interpretability and theoretical insight. Their complementary nature allows one to bridge the gap between physical realism and conceptual clarity. The subsequent section will delve into the mathematical formulation and dynamical behaviour of low-order models, which provide a compact yet powerful framework for probing non linear processes, regime transitions, and predictability in large scale atmospheric flow. Building on this foundation, we will further explore idealized frameworks developed specifically to investigate atmospheric blocking, tracing their historical evolution and highlighting key advances that have shaped our understanding of blocking dynamics in simplified model settings.

1.5 Idealized Frameworks for Blocking

Idealized atmospheric models provide controlled environments to isolate the physical and dynamical mechanisms governing large-scale circulation regimes such as atmospheric blocking. By omitting many of the complexities found in comprehensive General Circulation Models (GCMs), these models emphasize the essential nonlinear interactions, wave–mean flow dynamics, and regime transitions that shape midlatitude variability. The evolution of idealized frameworks parallels the development of dynamical systems theory and advances in computational capability.

1.5.1 Barotropic Models and Nonlinear Equilibria

The application of dynamical systems theory to atmospheric science began with the pioneering work of Lorenz [1963b], who reduced atmospheric convection to a minimal set of

three nonlinear ordinary differential equations:

$$\begin{aligned} \frac{dx}{dt} &= \sigma(y - x), \\ \frac{dy}{dt} &= x(\rho - z) - y, \\ \frac{dz}{dt} &= xy - \beta z, \end{aligned} \tag{1.12}$$

where x represents the convective velocity, y the horizontal temperature contrast, and z the deviation of vertical temperature from the conductive equilibrium. The nondimensional parameters σ, ρ, and β denote the Prandtl number, a scaled Rayleigh number, and a geometric aspect ratio, respectively. Despite its simplicity, the Lorenz system exhibits deterministic chaos, where infinitesimal differences in initial conditions lead to divergent trajectories. This discovery established the concept of limited atmospheric predictability and laid the foundation for nonlinear approaches to climate dynamics [Palmer, 1993].

Building on this conceptual groundwork, Charney and DeVore [1979] formulated a low-order barotropic model on a β-plane with stationary topographic forcing, described by the barotropic vorticity equation:

$$\frac{\partial \zeta}{\partial t} + J(\psi, \zeta + f + h) = -r\zeta + F, \tag{1.13}$$

where $\zeta = \nabla^2 \psi$ is the relative vorticity, ψ is the streamfunction, f is the Coriolis parameter, h represents the prescribed topographic height, r is a linear damping coefficient, and F is external forcing. The nonlinear Jacobian operator $J(A, B) = \partial_x A \, \partial_y B - \partial_y A \, \partial_x B$ captures advection of vorticity by the flow. When the equation is expanded in a small number of Fourier modes, the system exhibits multiple nonlinear equilibria corresponding to distinct flow regimes zonal and blocked states whose existence depends on the amplitude of stationary planetary waves and their interaction with orography. This framework provided a mechanistic explanation for the coexistence and persistence of different large-scale regimes and underscored the importance of planetary wave mean flow feedbacks in blocking dynamics.

Reinhold and Pierrehumbert [1982] extended the Charney–DeVore model by including stochastic forcing to represent the impact of transient synoptic eddies:

$$\frac{d\mathbf{a}}{dt} = \mathbf{N}(\mathbf{a}) + \mathbf{F} + \boldsymbol{\xi}(t), \tag{1.14}$$

where $\mathbf{a}$ is a vector of mode amplitudes, $\mathbf{N}(\mathbf{a})$ encapsulates nonlinear wave interactions, $\mathbf{F}$ is the deterministic forcing, and $\boldsymbol{\xi}(t)$ denotes a stochastic white noise process. The addition of $\boldsymbol{\xi}(t)$ enables transitions between coexisting regimes, simulating the random excitation of blocked and zonal states. Subsequent theoretical work using statistical mechanics and path integral formulations [Ghil, 1987; Legras and Ghil, 1985] demonstrated that regime persistence and transition probabilities are controlled by both the structure of the underlying attractor and the statistics of stochastic perturbations.

Later studies refined this paradigm by modifying basis functions (spectral vs. empirical orthogonal modes), applying stochastic optimal forcing, or introducing Markovian frameworks [Nitsche and Krasny, 1994; Crommelin, 2004]. These extensions confirmed the effectiveness of low-order barotropic models in capturing flow regime transitions, predictability limits, and nonlinear sensitivity of midlatitude circulation to external forcing.

1.5.2 Baroclinic and Quasi-Geostrophic Systems

To represent the vertical structure and thermal stratification of the atmosphere, barotropic models were extended into baroclinic and quasi-geostrophic (QG) frameworks. The QG approximation, derived from the primitive equations under assumptions of small Rossby number and near-geostrophic balance, filters out fast gravity waves and retains the slower, rotational motions that dominate midlatitude dynamics.

The simplest configuration is the barotropic QG model, governed by potential vorticity (PV) conservation [Charney, 1948]:

$$\frac{\partial}{\partial t}(\nabla^2\psi) + J(\psi, \nabla^2\psi + f) = 0, \tag{1.15}$$

where ψ is the streamfunction representing nondivergent horizontal flow, $J(\cdot,\cdot)$ the nonlinear advection operator, and $f = f_0 + \beta y$ the Coriolis parameter on a β-plane. This equation describes a single-layer homogeneous fluid and explains large-scale Rossby wave propagation, but it lacks representation of vertical wind shear or temperature gradients essential for baroclinic processes.

To overcome these limitations, Phillips [1951] developed a two-layer baroclinic QG model, later expanded by Charney and Straus [1980]. Each layer possesses its own streamfunction ψ_i and potential vorticity q_i, governed by

$$\frac{\partial q_1}{\partial t} + J(\psi_1, q_1) = -D_1 + F_1, \tag{1.16}$$

$$\frac{\partial q_2}{\partial t} + J(\psi_2, q_2) = -D_2 + F_2, \tag{1.17}$$

with potential vorticity defined as

$$q_i = \nabla^2\psi_i + (-1)^i \frac{1}{L_D^2}(\psi_1 - \psi_2) + \beta y. \tag{1.18}$$

Here $\nabla^2\psi_i$ denotes the relative vorticity, βy represents the planetary vorticity gradient, and the term $(-1)^i L_D^{-2}(\psi_1 - \psi_2)$ expresses the vertical coupling between layers through the Rossby deformation radius L_D. The forcing (F_i) and dissipation (D_i) terms represent diabatic heating and frictional damping, respectively. This two-layer system captures both baroclinic instability and energy exchange between layers, explaining how meridional temperature gradients generate eddies that redistribute momentum and heat, sustaining midlatitude variability. Extensions of this framework [Charney and Straus, 1980; Shutts, 1983; Tung and Rosenthal, 1985] further explored nonlinear equilibria, wave–mean flow feedbacks, and transitions between blocked and zonal regimes.

1.5.3 Coupled Systems and Surface Feedbacks

While atmospheric models such as those of Charney and DeVore [1979] treated the atmosphere as an isolated subsystem, real climate variability arises from interactions among multiple components of the Earth system. Idealized coupled models incorporate simplified representations of these interactions to examine how thermal and mechanical feedbacks between the atmosphere, ocean, and land affect large-scale circulation and predictability [Dijkstra, 2013].

One fundamental form of coupling links atmospheric dynamics to surface temperature through an *Energy Balance Model* (EBM) [North et al., 1981; De Cruz et al., 2016]. The EBM expresses the surface energy balance as

$$C\frac{\partial T_{\mathrm{s}}}{\partial t} = Q - A - BT_{\mathrm{s}} + D\nabla^2 T_{\mathrm{s}}, \tag{1.19}$$

where T_{s} is the surface temperature, C the effective heat capacity, Q the net absorbed solar radiation, A and B parameters of the linearized longwave radiation, and D a diffusion coefficient representing meridional heat transport. This equation states that surface temperature evolves from the balance between incoming and outgoing radiation, modulated by horizontal diffusion of heat. When coupled with the QG atmosphere, the evolving T_{s} modifies the meridional temperature gradient and thus the baroclinicity of the overlying flow, while the atmosphere simultaneously redistributes surface heat through advection and radiation.

Mechanical coupling, on the other hand, arises from orographic forcing and surface drag. In a two-layer QG system, the lower-layer potential vorticity equation can be written as

$$\frac{\partial q_2}{\partial t} + J(\psi_2, q_2 + f_0 h/H) = -D_2 - k_{\mathrm{drag}}\nabla^2\psi_2 + F_2, \tag{1.20}$$

where ψ_2 is the streamfunction of the lower layer, h represents topographic height, H is mean layer thickness, and k_{drag} is a friction coefficient. The term $J(\psi_2, f_0 h/H)$ introduces the effect of stationary topography, generating quasi-stationary Rossby waves that can anchor blocking highs. The linear damping term $-k_{\mathrm{drag}}\nabla^2\psi_2$ represents momentum loss to the surface through turbulent friction and boundary-layer drag. Together, these terms describe how topography and friction jointly influence large-scale flow regimes.

These idealized thermodynamic and mechanical couplings make QG systems more physically consistent with observed atmosphere–surface interactions. They enable investigation of how baroclinic eddies, orographic forcing, and radiative feedbacks interact to shape midlatitude variability and blocking persistence [Held and Ting, 1990; Faranda et al., 2017]. Despite their simplicity, such frameworks remain analytically and computationally tractable, providing essential building blocks for interpreting the behavior of more comprehensive General Circulation Models (GCMs).

1.6 Nonlinear Dynamical Systems and Chaos

The atmosphere, as part of the Earth system, exhibits high dimensional nonlinear behavior arising from fluid motion, thermodynamic processes, and interactions across spatial and temporal scales. Despite its apparent complexity, the evolution of atmospheric states can often be effectively understood using the mathematical framework of *nonlinear dynamical systems theory*, which provides the tools to analyze temporal evolution, stability, bifurcations, and the onset of chaotic dynamics [Strogatz, 2024; Ott, 2002; Thompson and Stewart, 2002].

1.6.1 Dynamical Systems: Definitions and Relevance

A dynamical system is formally defined as a system in which a function describes the time dependence of a point in a geometrical space. In mathematical terms, the evolution of a state vector $\vec{x}(t)$ is governed by a set of ordinary or partial differential equations:

$$\frac{d\vec{x}}{dt} = \vec{F}(\vec{x}, t), \tag{1.21}$$

where $\vec{x} \in \mathbb{R}^n$ is the state of the system at time t and $\vec{F}$ is a nonlinear vector field representing the governing physical laws. In autonomous systems, $\vec{F}$ is not explicitly dependent of time. In atmospheric science, examples include low-order models like the Lorenz system [Lorenz, 1963b] (section 1.5.1), quasi geostrophic equations [Vallis, 2017], and reduced-order frameworks for studying baroclinic instability or blocking [Lucarini and Gritsun, 2020].

Such systems can capture essential features of atmospheric dynamics such as oscillatory behavior, energy cascades, and feedback loops without the need for full scale numerical models [Ghil, 1987]. The central goal is to understand the qualitative behavior of the system, identify attractors, and assess stability and predictability.

1.6.2 Phase Space and Trajectory Evolution

A central concept in dynamical systems theory is the notion of *phase space* or *state space*, an abstract n - dimensional space in which each possible state of the system is represented as a unique point. For a three-dimensional system, the phase space is a 3D manifold where the system trajectory $\mathbf{x}(t)$ traces out the temporal evolution. For instance, in the Lorenz system, the phase space is defined by the three variables (X, Y, Z), and the attractor represents the bounded but non-repeating behavior of the system [Sparrow, 1982].

1.6.3 Phase Space Geometry, Attractors, and Regime Behavior

Phase space geometry encodes critical information about the qualitative behavior of a dynamical system. Fundamental structures include:

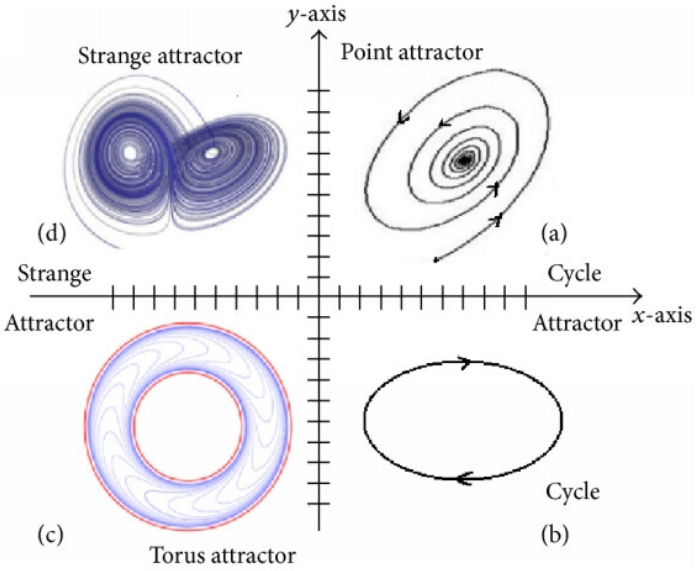


Figure 1.8: Different types of attractors constructed in 2-dimensional phase space; (a) point attractor, (b) limit cycle, (c) limit torus, and (d) strange attractor *Source : Adewumi et al. [2016]; Shewalo et al. [2012]*

- **Fixed points (equilibria):** Points where $\mathbf{F}(\mathbf{x}) = 0$. Their stability is determined by linearizing the system around them [Wiggins, 2003].
- **Limit cycles:** Closed trajectories representing periodic oscillations.
- **Quasi-periodic orbits (tori):** Motions characterized by incommensurate frequencies on low-dimensional manifolds.
- **Strange attractors:** Non-periodic but bounded trajectories with fractal structure, indicative of deterministic chaos [Ott, 2002; Eckmann and Ruelle, 1985a].
- **Basins of attraction:** Regions of phase space from which trajectories converge to a particular attractor [Strogatz, 2001].

An *attractor* is a subset of phase space toward which the system tends to evolve. In dissipative systems like the atmosphere, attractors are typically low-dimensional manifolds embedded in a much higher-dimensional phase space [Ruelle, 1989]. Depending on system parameters, attractors may take the form of steady states (fixed points), periodic orbits (limit cycles), quasi-periodic tori, or chaotic sets (strange attractors) as shown in figure 1.8.

The long-term statistical properties of trajectories on attractors are described by *invariant measures*, which provide a probabilistic description of system states and form the mathematical basis for ergodic theory [Eckmann and Ruelle, 1985a]. Invariant measures allow time-averaged observables (e.g., mean flow, variance) to be related to ensemble averages, thus linking deterministic dynamics with statistical behavior.

In multistable systems, multiple attractors may coexist, with transitions triggered by stochastic perturbations or deterministic instabilities. This framework is particularly relevant for atmospheric circulation, where distinct regimes such as zonal flow and blocking correspond to different regions of phase space. Noise-induced transitions between regimes [Nicolis and Nicolis, 1981; Ghil, 1987] provide a natural language to describe the persistence, recurrence, and predictability of large-scale anomalies in idealized and realistic atmospheric models [Faranda et al., 2017; Lucarini et al., 2016].

1.6.4 Chaos and Sensitivity to Initial Conditions

An important feature of nonlinear dynamical systems is their potential to exhibit *chaos*, a regime in which the system's evolution is highly sensitive to initial conditions, despite being governed by deterministic rules [Lorenz, 1963b]. This means that arbitrarily small perturbations in initial state $\delta\mathbf{x}(0)$ can grow exponentially over time:

$$|\delta\mathbf{x}(t)| \sim |\delta\mathbf{x}(0)|e^{\lambda t}, \tag{1.22}$$

where λ is the *Lyapunov exponent* [Eckmann and Ruelle, 1985a; Boffetta and Musacchio, 2002]. Positive Lyapunov exponents are indicative of chaotic behavior and finite predictability horizons, a fundamental challenge in weather forecasting [Palmer, 1993].

Chaos manifests in the fractal geometry of attractors (e.g., the Lorenz attractor), nonperiodic trajectories and sensitivity to small perturbations in model structure or forcing. In climate models, chaotic dynamics can coexist with forced responses, leading to irregular transitions between flow regimes such as blocking and zonal states [Ghil, 2008; Crommelin, 2004].

1.6.5 Bifurcation Theory and Transitions Between Flow Regimes

Bifurcation theory investigates how the qualitative behavior of a dynamical system changes as one or more control parameters vary. In atmospheric and climate dynamics, bifurcations provide a theoretical foundation for understanding transitions between different large-scale circulation regimes and the emergence of complex behavior such as periodic oscillations or chaos. They signify the creation or destruction of equilibria, changes in their stability, or the birth of oscillatory modes, thereby explaining how continuous variations in forcing can lead to abrupt reorganizations in flow patterns [Strogatz, 2001; Sparrow, 1982; Wiggins, 2003].

1.6.5.1 Pitchfork Bifurcation

A *pitchfork bifurcation* is a classic example of a symmetry-breaking transition in nonlinear systems. It occurs when an initially symmetric equilibrium becomes unstable as a control parameter such as topographic amplitude or thermal forcing crosses a critical threshold. This mechanism is particularly relevant in atmospheric models where symmetric zonal flows give way to asymmetric blocked states.

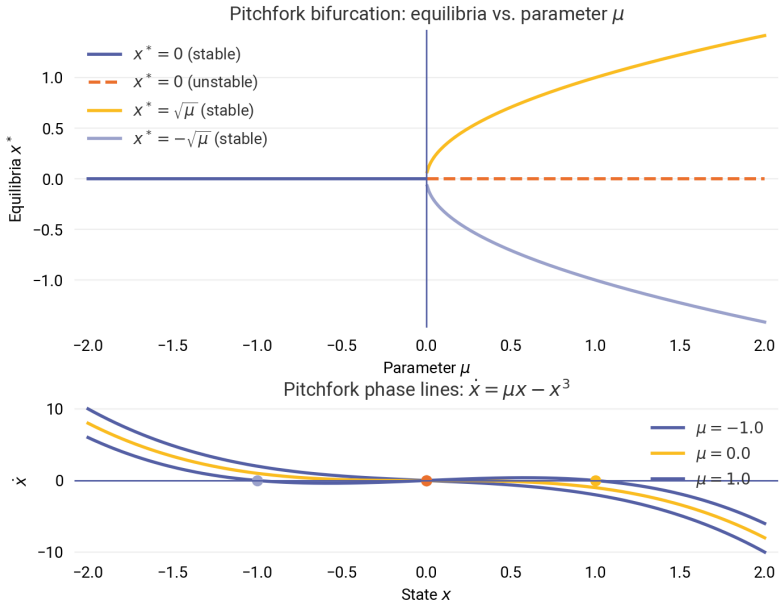


Figure 1.9: **Pitchfork bifurcation (normal form $\dot{x} = \mu x - x^3$).** *Top:* Equilibria x^* versus control parameter μ. The symmetric state $x^* = 0$ is stable for $\mu < 0$ (solid) and unstable for $\mu > 0$ (dashed); two stable asymmetric equilibria $x^* = \pm\sqrt{\mu}$ appear for $\mu > 0$ (solid), illustrating symmetry breaking. *Bottom:* One–dimensional phase lines $\dot{x}$ vs. x for representative μ values, with dots marking equilibria and indicating stability (zero crossings with negative slope are stable).

The behavior shown in Fig. 1.9 can be represented by the normal form:

$$\frac{dx}{dt} = \mu x - x^3, \tag{1.23}$$

where μ is the control parameter. For $\mu < 0$, the system possesses a single stable equilibrium at $x = 0$. At the critical value $\mu = 0$, this equilibrium loses stability, and for $\mu > 0$, two new stable equilibria appear at $x = \pm\sqrt{\mu}$ while $x = 0$ becomes unstable. The system's behavior "branches" into two preferred configurations, hence the name *pitchfork*.

In the atmospheric context, this bifurcation captures how a zonally symmetric circulation can transition into two asymmetric steady states, each representing a preferred stationary wave or blocking configuration displaced east or west of a topographic feature. This behavior was first identified in the barotropic model of Charney and DeVore [1979], where increasing topographic forcing produced multiple steady solutions, one zonal and one blocked under the same external conditions. Such coexistence explains why the midlatitude atmosphere can shift spontaneously between regimes without significant external changes, a hallmark of *regime behavior*.

A *subcritical* pitchfork bifurcation can also occur, in which the new equilibria exist before the symmetric state loses stability, creating a region of multistability. This feature is crucial for understanding *regime persistence and memory*, where the flow remains trapped in a blocked or zonal state depending on its history.

1.6.5.2 Hopf Bifurcation

A *Hopf bifurcation* describes the transition from a steady equilibrium to self-sustained oscillations as a pair of complex conjugate eigenvalues of the system's Jacobian cross the imaginary axis. Here, the *Jacobian* refers to the matrix of first-order partial derivatives of the vector field defining the dynamical system, evaluated at the equilibrium point; its eigenvalues determine the local linear stability of that equilibrium. The bifurcation occurs when a complex conjugate pair of these eigenvalues shifts from having negative real parts (stable) to positive real parts (unstable) as a control parameter varies.

This leads to the emergence of a *limit cycle*, representing periodic motion around the original equilibrium.

The Hopf normal form is expressed as

$$\frac{dz}{dt} = (\mu + i\omega)z - |z|^2 z, \tag{1.24}$$

where z is a complex variable, μ the bifurcation parameter, and ω the intrinsic frequency. In this reduced form, μ acts as the real control parameter governing the stability transition, while ω sets the natural angular frequency of the oscillations at the onset of the bifurcation.

For $\mu < 0$, trajectories decay toward the steady state $z = 0$. At $\mu = 0$, the equilibrium loses stability, and for $\mu > 0$, the system evolves into a periodic orbit of radius $|z| = \sqrt{\mu}$.

Figure 1.10 illustrates this transition: for $\mu < 0$, trajectories spiral inward to a stable focus; for $\mu > 0$, they settle onto a stable limit cycle. Physically, the Hopf bifurcation represents the onset of temporal oscillations once the steady state can no longer remain stable. In atmospheric systems, such behavior is observed when a critical temperature gradient or rotation rate is exceeded, giving rise to oscillatory phenomena such as baroclinic wave vacillations, the Quasi-Biennial Oscillation (QBO), or the Madden–Julian Oscillation (MJO). Thus, while the pitchfork bifurcation explains the appearance of multiple steady regimes, the Hopf bifurcation accounts for the emergence of periodic variability in time.

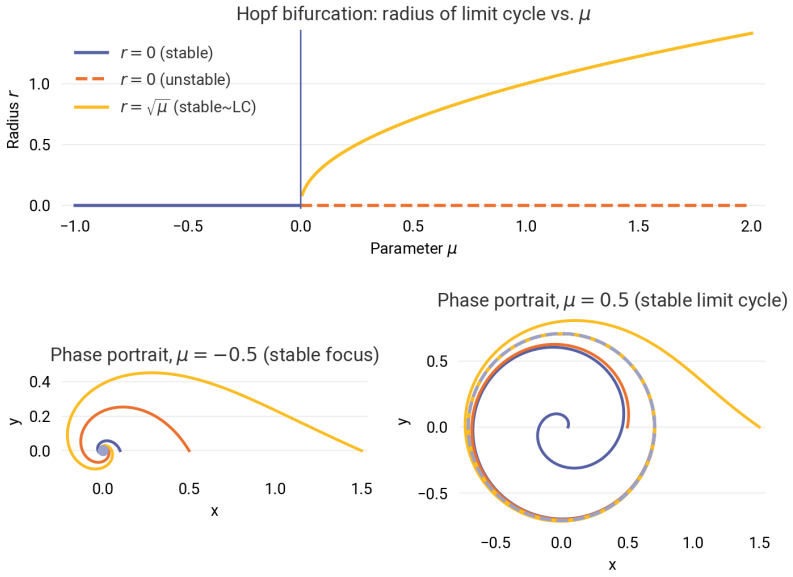


Figure 1.10: Hopf bifurcation (normal form $\dot{z} = (\mu + i\omega)z - |z|^2 z$). Top: Radius of the periodic orbit r versus μ. For $\mu < 0$ the fixed point $r = 0$ is stable (solid); at $\mu = 0$ it loses stability (dashed), and for $\mu > 0$ a stable limit cycle with radius $r = \sqrt{\mu}$ emerges (solid). Bottom: Phase portraits in (x, y) for $\mu < 0$ (left; trajectories spiral to the stable focus) and $\mu > 0$ (right; trajectories approach the stable limit cycle; dashed circle shows the theoretical radius).

1.6.5.3 Saddle Node Bifurcation

A *saddle node* (or *fold*) bifurcation occurs when two equilibria, one stable and one unstable, collide and annihilate each other as a control parameter changes. This mechanism explains how smooth parameter variations can produce abrupt transitions or *tipping points* in nonlinear systems.

Its canonical form is

$$\frac{dx}{dt} = \mu - x^2, \tag{1.25}$$

where μ is the control parameter. For $\mu > 0$, two fixed points exist at $x = \pm\sqrt{\mu}$—the positive branch stable, the negative branch unstable. At $\mu = 0$, these equilibria merge into a single semi-stable point, and for $\mu < 0$, no equilibrium exists. The disappearance of the stable equilibrium forces the system to shift abruptly to a different state.

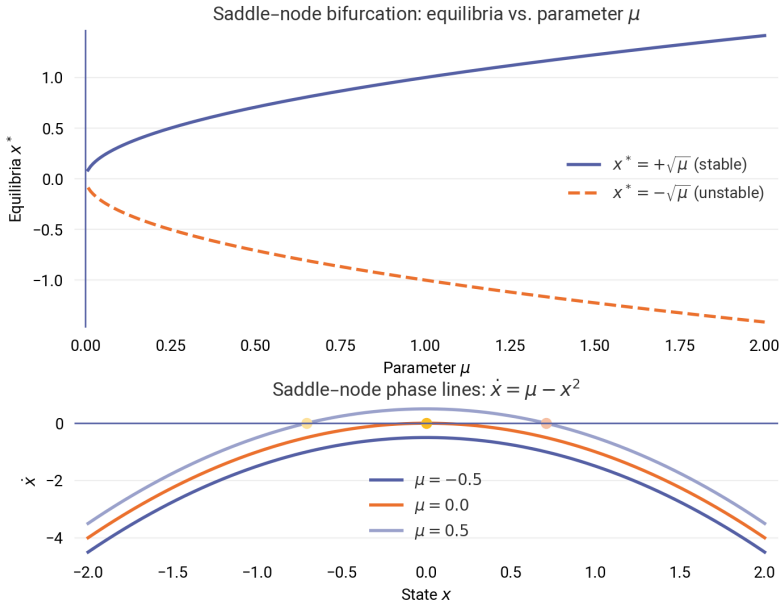


Figure 1.11: **Saddle node (fold) bifurcation (normal form $\dot{x} = \mu - x^2$).** *Top:* Equilibria $x^* = \pm\sqrt{\mu}$ exist only for $\mu > 0$: the positive branch is stable (solid) and the negative branch unstable (dashed). At $\mu = 0$, the equilibria collide and annihilate; for $\mu < 0$ no equilibria exist. *Bottom:* Phase lines $\dot{x}$ vs. x for representative μ values highlight the tangent (semi-stable) case at $\mu = 0$ and the absence of fixed points for $\mu < 0$, illustrating abrupt regime loss and tipping behavior.

As shown in Fig. 1.11, this process captures the essence of a tipping event: a slow change in forcing (e.g., planetary wave amplitude or surface temperature contrast) can push the system to a threshold beyond which a stable circulation pattern (such as a blocked state) ceases to exist. The atmosphere then transitions suddenly to another configuration, often accompanied by hysteresis. Once the new state is reached, reversing the forcing does not immediately restore the original regime a feature characteristic of nonlinear climate responses.

The theoretical framework of dynamical systems has been widely applied to study *atmospheric blocking*, an archetypal example of regime behavior [Romeiras et al., 1990; Faranda et al., 2017; Xavier et al., 2024]. Blocking episodes correspond to quasi-stationary attractors in the system's phase space, whose persistence and transitions are controlled by the local stability structure. Techniques such as Lyapunov exponents, recurrence analysis, and transition path theory reveal that blocked states are dynamically unstable yet

long-lived, leading to enhanced forecast uncertainty and low predictability. These methods have deepened understanding of how nonlinear bifurcations underpin the emergence, persistence, and decay of large-scale flow regimes in both idealized and realistic models [Lucarini and Gritsun, 2020; Crommelin, 2004].

1.7 Thesis Outline

The concepts introduced in the preceding sections, from the physical structure of the atmosphere to the hierarchy of climate models and the fundamental principles of nonlinear dynamics, were presented to build a coherent framework for understanding the complex nature of midlatitude circulation. Each topic contributes to a central question that motivates this thesis: *why is atmospheric blocking so difficult to predict and how can its variability be quantified using a dynamical systems perspective?*

Atmospheric blocking represents a quintessential example of nonlinear regime behavior. Its emergence, persistence, and decay arise from intricate interactions between waves, mean flow, and surface boundary conditions. By revisiting the theoretical underpinnings of bifurcation theory, stability analysis, and coupled quasi–geostrophic dynamics, the discussion so far has aimed to show that the atmosphere is not a simple, linearly responding system but one characterized by multiple equilibria, oscillatory modes, and abrupt transitions. These phenomena collectively govern the limits of predictability and the intrinsic variability of large scale flow regimes.

The review of model hierarchies, from comprehensive General Circulation Models (GCMs) to low order quasi geostrophic systems was included to highlight how the same physical processes can be studied across varying levels of complexity. Idealized models provide the interpretive clarity necessary to isolate key dynamical mechanisms, while GCMs ensure realism and global relevance. The combination of these frameworks allows us to link theoretical understanding with practical predictability in a physically consistent way.

Building on this foundation, the subsequent chapter introduces the quantitative tools employed in this thesis to diagnose and measure predictability and variability of atmospheric blocking. Specifically, Lyapunov exponents are used to characterize local stability and error growth; analogue techniques quantify flow recurrence and regime similarity; and causality analysis is applied to disentangle information transfer between energy reservoirs and surface variables. Together, these tools bridge theory and simulation, enabling a systematic evaluation of how nonlinear dynamics govern the temporal and spatial organization of blocking events.

In essence, the preceding chapters establish the theoretical and modelling basis required to address the core objective of this work: *to quantify the predictability and variability of atmospheric blocking in with both idealized and comprehensive climate model frameworks.* The following chapter therefore transitions from conceptual foundations to the specific methodological approaches developed and applied throughout this thesis.

Guided by the gaps outlined in Chapter 1, my collaborators and I focused on three core questions that emerged over the course of my PhD. What began as a single question expanded as our first results opened new directions. This thesis is organized around those three guiding questions. In what follows, we state each question and briefly describe how the corresponding chapter addresses it, moving from idealized dynamics to more complex models and from description to mechanism.

Can a low-order land - atmosphere coupled model capture the variability and predictability of large scale flow regimes in the atmosphere?
This chapter uses a reduced order quasi geostrophic land - atmosphere coupled model in which parameters (e.g., friction (k_d), heat exchange between land and atmosphere λ) are systematically varied to obtain different flow regimes in the atmosphere, zonal, blocking, and transitional regimes. Regime identification is performed with clustering while predictability is assessed using the average of local lyapunov exponents based on different clusters. Important results were the highly stable zonal regimes compared to blocking regime. We also identified that the morphology or proximity of topographical features influence the predictability of blocking regime (chapter 3).

Can the location of atmospheric blockings relative to topography affect their predictability in complex climate models such as CMIP6?
This study as I said earlier was an idea developed from the second result of my initial work where we identified the influence of morphology in the predictability of blocks. Here the methodology is transferred to complex climate model simulations, focusing on the North Pacific in MIROC6 (with targeted cross-checks in other CMIP6 models) to examine whether blocks adjacent to the Asian versus North American margins exhibit different predictability. Blocking events are identified with established Davini et al. [2012] indices and other defined constraints, then paired with reference - analogue framework to quantify predictability, allowing a comparison with an important result obtained from the idealized experiments. Results showed that there is indeed a difference in predictability of blocks due to its proximity towards topographical features. Specifically we obtained very stable Western North Pacific blocks compared to its Eastern counterpart(chapter 4).

Can directional energetic couplings between kinetic energy, available potential energy, and ground temperature explain differences in blocking variability across regions and models?
This chapter introduces a causality based energetics analysis by applying the Liang - Kleeman information flow framework to both the idealized model and MIROC6, quantifying directed interactions among LEC reservoirs (KE, APE) and surface temperature to answer the 'why' question. why there is a difference in the variability of blocks? By comparing blocked versus non blocked composites, and eastern versus western events, the chapter is connecting the difference in causal pathways to the identified difference in the variability of the identified blocking situations. Eastern and western blocks are having an entirely different causal path ways between the selected parameters and the pathways are also model dependent which can be attributed towards the differences in the variability between them (chapter 5).

Chapter 2

From Theory to Application: Technical Methods Used in this Thesis

2.1 Land - Atmosphere Coupled Model

We employ a reduced order quasi geostrophic (QG) land - atmosphere model implemented in the qgs Python framework [Demaeyer et al., 2020]. The formulation builds on the conceptual lineage of Saltzmann [Saltzman, 1962], Lorenz [Lorenz, 1963b], Charney–DeVore [Charney and DeVore, 1979], and Charney–Straus [Charney and Straus, 1980]. In particular, Saltzmann's pioneering work introduced the use of truncated spectral expansions to construct finite dimensional approximations of the QG equations, laying the foundation for later low order models of atmospheric regimes and predictability. The model used here couples a two layer QG channel atmosphere on a β - plane to a simplified land surface energy balance component [Li et al., 2018; Xavier et al., 2024]. This section gives a compact statement of the dynamical core; detailed thermodynamic and mechanical couplings are developed in Section 1.5.3.

2.1.1 Atmospheric dynamics

Let ψ_1 and ψ_3 be the upper and lower layer streamfunctions. We work with barotropic and baroclinic combinations

$$\psi = \tfrac{1}{2}(\psi_1 + \psi_3), \qquad \theta = \tfrac{1}{2}(\psi_1 - \psi_3). \tag{2.1}$$

The barotropic and baroclinic vorticity equations read

$$\frac{\partial}{\partial t}\nabla^2\psi + J(\psi,\nabla^2\psi) + J(\theta,\nabla^2\theta) + \beta\,\frac{\partial\psi}{\partial x} = -\tfrac{1}{2}J\left(\psi,\frac{f_0 h}{H}\right) + \tfrac{1}{2}J\left(\theta,\frac{f_0 h}{H}\right) - k\nabla^2(\psi-\theta), \tag{2.2}$$

$$\frac{\partial}{\partial t}\nabla^2\theta + J(\psi,\nabla^2\theta) + J(\theta,\nabla^2\psi) + \beta\,\frac{\partial\theta}{\partial x} = \tfrac{1}{2}J\left(\psi,\frac{f_0 h}{H}\right) - \tfrac{1}{2}J\left(\theta,\frac{f_0 h}{H}\right) + k\nabla^2(\psi-\theta) - 2k'\nabla^2\theta + \frac{f_0}{\Delta p}\,\omega. \tag{2.3}$$

Here J is the horizontal Jacobian, β the meridional gradient of the Coriolis parameter, $h(x,y)$ the orography with mean layer depth H, k the surface-drag coefficient acting on barotropic/baroclinic shear, k' an internal damping, and ω the vertical pressure velocity. The $J(\cdot, f_0 h/H)$ terms encode stationary topographic forcing; drag terms parameterize boundary layer dissipation. The physical interpretation of these terms, and their role in regime behavior, is discussed in Section 1.5.3.

2.1.2 Thermal Coupling via Surface Temperature Feedback

The atmosphere is thermodynamically coupled to a land surface through prognostic atmospheric and ground temperatures, T_a and T_g, with radiative and turbulent heat exchanges [Barsugli and Battisti, 1998; Li et al., 2018]:

$$\gamma_a\left(\frac{\partial T_a}{\partial t} + J(\psi,T_a) - \frac{\sigma\,\omega}{p}\right) = -\lambda(T_a - T_g) + \epsilon_a\sigma_B T_g^4 - 2\epsilon_a\sigma_B T_a^4 + R_a, \tag{2.4}$$

$$\gamma_g\frac{\partial T_g}{\partial t} = -\lambda(T_g - T_a) - \sigma_B T_g^4 + \epsilon_a\sigma_B T_a^4 + R_g. \tag{2.5}$$

Here λ is the turbulent exchange coefficient, σ_B the Stefan–Boltzmann constant, and R_a, R_g shortwave forcings; quartic terms are linearized for tractability [Vannitsem et al., 2015; Li et al., 2018]. The linkage between θ and T_a follows from hydrostatic balance and the thermal-wind relation (see Section 1.5.3 for a pedagogical derivation). Unlike the Charney–Straus setup with a prescribed radiative equilibrium, Eqs. (2.4)–(2.5) enable true two-way feedback between surface temperature anomalies and atmospheric baroclinicity.

2.1.3 Mechanical Coupling: Orography and Friction

Topography forces quasi-stationary Rossby waves through $J(\psi, f_0 h/H)$ and $J(\theta, f_0 h/H)$ in Eqs. (2.2) - (2.3), while surface drag and internal damping are represented by $-k\nabla^2(\psi-\theta)$ and $-2k'\nabla^2\theta$, respectively. The full lower-layer PV tendency with topographic vorticity source is given in Eq. (1.20) (Section 1.5.3), where each term is interpreted physically.

Within realistic parameter ranges the coupled system exhibits multiple equilibria (ridge- and trough-locked states relative to orography), high/low-index flows (zonal vs. blocked), and transitions between periodic, quasi-periodic, and chaotic regimes near bifurcations [Li et al., 2018; Xavier et al., 2024].

To support stability and continuation analyses (e.g., Lyapunov exponents, Jacobians, parameter sweeps), we extended qgs with a symbolic backend using `SymPy` [Meurer et al., 2017; Demaeyer et al., 2020]. Core operations (inner products, tensor contractions, equation assembly) are performed symbolically, enabling on-the-fly equation generation, parameter variation without recompilation, and seamless export of model equations to other languages (e.g., Fortran, Julia). This symbolic engine underpins the diagnostics used throughout this thesis.

2.2 Lyapunov Exponents and the Growth of Perturbations in QG Systems

The concept of Lyapunov exponents (LEs) lies at the heart of nonlinear dynamical systems theory and provides a rigorous measure of predictability. First introduced in the late 19$^{\text{th}}$ century by Aleksandr Lyapunov, these exponents quantify the average exponential rate at which infinitesimal perturbations to initial conditions grow or decay over time [Benettin et al., 1980b; Eckmann and Ruelle, 1985b; Boffetta et al., 2002]. In atmospheric science, LEs provide a theoretical limit to forecast skill and have been widely applied in both low-order models [Palmer, 1993; Vannitsem et al., 2015; De Cruz et al., 2016] and high dimensional climate simulations [Ghil, 2008; Lucarini et al., 2016; Vannitsem and Nicolis, 1997a].

2.2.1 Definition and Theoretical Framework

Consider a deterministic dynamical system governed by a system of ordinary differential equations (ODEs):

$$\frac{d\mathbf{x}}{dt} = \mathbf{F}(\mathbf{x}), \tag{2.6}$$

where $\mathbf{x}(t) \in \mathbb{R}^n$ is the state vector and $\mathbf{F} : \mathbb{R}^n \to \mathbb{R}^n$ is a nonlinear differentiable vector field.

Suppose a small perturbation $\delta\mathbf{x}(0)$ is introduced to the initial state. The evolution of this perturbation is governed by the tangent linear equation:

$$\frac{d\delta\mathbf{x}}{dt} = \mathbf{J}(\mathbf{x})\,\delta\mathbf{x}, \tag{2.7}$$

where $\mathbf{J}(\mathbf{x}) = \partial\mathbf{F}/\partial\mathbf{x}$ is the Jacobian matrix evaluated along the trajectory $\mathbf{x}(t)$.

The fundamental matrix solution $\mathbf{M}(t)$ of Eq. (2.7), with $\mathbf{M}(0) = \mathbf{I}$, evolves perturbations via:

$$\delta\mathbf{x}(t) = \mathbf{M}(t)\delta\mathbf{x}(0). \tag{2.8}$$

The first (or dominant) Lyapunov exponent associated with a perturbation $\delta\mathbf{x}(0)$ is defined as:

$$\lambda = \lim_{t\to\infty} \frac{1}{t} \ln \frac{\|\delta\mathbf{x}(t)\|}{\|\delta\mathbf{x}(0)\|} = \lim_{t\to\infty} \frac{1}{t} \ln \|\mathbf{M}(t)\delta\mathbf{x}(0)\|. \tag{2.9}$$

For an n-dimensional system, there exists a spectrum of n Lyapunov exponents $\lambda_1 \geq \lambda_2 \geq \cdots \geq \lambda_n$, corresponding to the exponential growth rates along different directions in tangent space [Oseledec, 1968; Boffetta et al., 2002]. A positive maximum Lyapunov exponent (MLE) indicates chaos and sensitive dependence on initial conditions.

2.2.2 Computation via QR Decomposition

The computation of the full Lyapunov spectrum for systems of moderate to high dimension typically follows the algorithm of Benettin et al. [1980b]. The nonlinear system (Eq. (2.6)) is evolved together with n perturbation vectors that satisfy the tangent linear model (Eq. (2.7)). As time advances, these perturbations tend to align with the most unstable direction, leading to numerical collapse. To prevent this, the perturbation matrix is periodically re-orthonormalized every Δt using a QR decomposition, which preserves linear independence while allowing the extraction of local stretching rates. The ergodic properties and theoretical background of Lyapunov spectra were formalized by Eckmann and Ruelle [1985b].

At each re-orthonormalization step, the matrix of evolved perturbations $\mathbf{M}$ is factorized as

$$\mathbf{M} = \mathbf{QR},$$

where $\mathbf{Q}$ is orthonormal and $\mathbf{R}$ is upper triangular. The diagonal entries r_{ii} of $\mathbf{R}$ represent the instantaneous expansion or contraction rates along each orthogonalized direction. Accumulating their logarithms over successive QR steps yields the Lyapunov exponents,

$$\lambda_i = \lim_{t\to\infty} \frac{1}{t} \sum_{k=1}^{N} \ln r_{ii}^{(k)}, \quad t = N\Delta t.$$

This QR-based approach is robust and widely used, though it becomes computationally demanding for very high-dimensional systems due to the repeated evolution of the tangent linear model and QR factorizations.

2.2.3 QR Decomposition via the Gram–Schmidt Process

One classical approach for constructing the QR decomposition is the Gram–Schmidt orthogonalization procedure. Given a matrix of perturbation vectors $\mathbf{M} = [\mathbf{m}_1, \ldots, \mathbf{m}_n]$, the Gram–Schmidt process constructs an orthonormal basis $\{\mathbf{q}_i\}$ and triangular matrix $\mathbf{R}$ such that $\mathbf{M} = \mathbf{QR}$. Although conceptually transparent, the classical Gram–Schmidt algorithm is known to be numerically unstable for high-dimensional or ill-conditioned systems [Golub and Van Loan, 2013; Trefethen and Bau, 1997]. In most practical implementations of Lyapunov exponent calculations, modified Gram–Schmidt or Householder-based

QR methods [Benettin et al., 1980a; Dieci and Van Vleck, 2002] are therefore preferred. The purpose of this subsection is solely to illustrate the geometric interpretation of the QR factorization; the computation of Lyapunov exponents follows the general algorithm described above.

2.2.4 Lyapunov Exponents in Quasi-Geostrophic Models

In the two-layer quasi-geostrophic (QG) channel model used in this thesis, the state vector $\mathbf{x}$ consists of Fourier coefficients or grid-point values of dynamical fields such as streamfunctions, temperatures, and vorticities. The vector field $\mathbf{F}(\mathbf{x})$ defining the evolution equations (Eqs. (2.2)–(2.3), (2.4)–(2.5)) is differentiated symbolically using the SymPy-based qgs framework [Meurer et al., 2017; Demaeyer et al., 2020], yielding the Jacobian matrix $\mathbf{J}(\mathbf{x})$ required for the tangent linear model. Recent extensions of qgs also allow automated bifurcation and stability analysis [Demaeyer and Hamilton, 2025].

The nonlinear model is integrated using a fourth-order Runge–Kutta method with a sufficiently small time step to resolve all relevant dynamical modes. Simultaneously, the tangent linear model,

$$\frac{d\delta\mathbf{x}}{dt} = \mathbf{J}(\mathbf{x})\delta\mathbf{x},$$

advances a set of perturbation vectors. At fixed intervals, the perturbation matrix is re-orthonormalized using a numerically stable QR factorization, and the diagonal entries of the resulting $\mathbf{R}$ matrices are accumulated to estimate the Lyapunov exponents via Eq. (**??**). The resulting spectrum provides quantitative information on instability, predictability, and the effective number of active degrees of freedom in the QG system.

2.2.5 Physical Interpretation and Predictability

The maximum Lyapunov exponent λ_1 provides a fundamental measure of the system's predictability horizon T_p via:

$$T_p \approx \frac{1}{\lambda_1} \ln\left(\frac{\delta_{\text{max}}}{\delta_0}\right), \tag{2.10}$$

where δ_0 is the initial uncertainty and δ_{max} the acceptable forecast error. This relation underscores the exponential divergence of nearby trajectories in chaotic systems and bounds the useful forecasting timescale [Palmer, 1993; Nicolis and Nicolis, 1991].

In the context of atmospheric blocking, the LE spectrum reveals the stability properties of different flow regimes. Blocked states often exhibit larger MLEs and decreased persistence compared to zonal flows, indicating metastability and reduced local instability [Vannitsem et al., 2015; De Cruz et al., 2016; Xavier et al., 2024]. Near bifurcation thresholds, averaged local Lyapunov exponents approach zero, indicating marginal stability and enhanced sensitivity to external perturbations. Lyapunov exponents have been extensively used to characterize low-frequency variability [Romeiras et al., 1990], investigate ensemble forecast divergence [Boffetta and Musacchio, 2002], and assess climate response to external forcing [Lucarini et al., 2016; Ghil, 2008]. In particular, Lyapunov exponents

enable the identification of dynamical transitions between periodic, quasi-periodic, and chaotic regimes by analysing changes in the Lyapunov spectrum. The averaged local Lyapunov exponents also allow for a quantitative comparison of the predictability associated with different flow regimes, such as blocked versus zonal states. Furthermore, Lyapunov analysis facilitates the exploration of how coupling mechanisms such as land-atmosphere feedbacks modify the overall stability of the system by altering its sensitivity to initial conditions and structural perturbations. Recent advances also connect LEs to extreme value theory [Lucarini et al., 2016], response theory [Ruelle, 1989], and information theory metrics such as entropy production and Kolmogorovn - Sinai entropy [Eckmann and Ruelle, 1985b].

Lyapunov exponents serve as a powerful diagnostic tool to quantify the intrinsic predictability of atmospheric systems, revealing the growth of uncertainties and the underlying phase space geometry. Their computation in coupled QG models, especially those incorporating land surface feedbacks, allows for a nuanced understanding of flow regime stability and transitions. In this thesis, the full Lyapunov stability framework, including Lyapunov exponents, spectrum, and backward Lyapunov vectors, is employed to investigate how different atmospheric flow regimes - zonal, blocked, and transitional - respond to internal variability and external forcing within a controlled idealized setting.

2.3 Predictability using Analogues

While the historical development and conceptual foundations of analogue methods were reviewed in Chapter 1, the present section introduces a novel application of this framework, motivated by work conducted during a research stay at Tel Aviv University in collaboration with Dr. Nili Harnik and Dor Sandler. Unlike conventional analogue studies that rely on physical-space similarity over localized regions, this analysis explores analogue behaviour within a reduced-dimension EOF phase space associated with large-scale teleconnection modes.

Though the results did not reveal conclusive geographical differences in predictability, this phase-space analogue approach provided critical insights and laid the groundwork for the analogue methodology developed in Chapter 4. What follows is a detailed account of the methodology, data, and outcomes of this early investigation.

2.3.1 Predictability of Circumglobal Teleconnection Pattern Using Analogues

The Circumglobal Teleconnection (CGT) pattern is a large-scale, quasi-stationary Rossby wave train predominantly observed in the Northern hemisphere's upper troposphere during boreal summer and winter [Branstator, 2002]. It is often characterized by a zonal wave number - 5 structure and serves as a dominant mode of variability in meridional wind at 300 hPa [Feldstein and Dayan, 2008; Harnik et al., 2016]. The CGT not only modulates large-scale flow regimes but also influences the occurrence and persistence of extreme

events such as heatwaves, droughts, and flooding across Asia, Europe, and North America [Wang et al., 2013; Branstator and Teng, 2017].

Historically, CGT has been extracted through Empirical Orthogonal Function (EOF) analysis applied to sub-seasonal anomalies of upper tropospheric meridional wind. This method allows the identification of dominant modes of variability, with CGT typically captured by the first two EOFs [Branstator, 2002]. The persistence and predictability of CGT events are of paramount importance for subseasonal forecasting and for understanding their contribution to climate extremes [Sandler and Harnik, 2020; Ghil, 2008].

2.3.2 Data and Methodology

This study was initiated during an international secondment at Tel Aviv University, aiming to explore the predictability of the CGT pattern using analogue methods. Unlike traditional analogue approaches that operate in physical space or over fixed spatial domains [Yiou, 2014], we applied the analog method in the phase space defined by leading circumglobal teleconnection (CGT) pattern is extracted by computing the leading two empirical orthogonal functions (EOFs) of 300 hPa meridional wind.

We utilize ERA5 reanalysis data [Hersbach et al., 2020] spanning the period 1983 - 2019, focusing on the boreal winter season (DJF). The spatial domain encompasses the extratropical Northern Hemisphere, specifically from 20°N to 70°N latitude and 70°W to 40°E longitude. Following the methodology outlined by Branstator [2002], the dominant structure of the circumglobal teleconnection (CGT) pattern is extracted by computing the leading two EOFs of 300 hPa meridional wind anomalies. To better resolve latitudinal differences in the CGT structure, EOF analyses are performed separately for two latitude bands: the subtropics (20°N - 45°N, 40°W - 40°E) and the midlatitudes (45°N - 70°N, 70°W - 40°E) along with the entire domain [Sandler and Harnik, 2020]. The EOF decomposition was applied within each of these spatial windows to extract the leading modes of variability specific to their respective dynamical regimes.

To explore the broader spatial imprint of these regionally dominant modes, we computed EOFs of the subseasonal anomaly of DJF meridional wind at 300 hPa within two latitude bands (25–45°N and 45–70°N) with all the longitudes. Each regional EOF yields a corresponding principal component (PC) time series. While the EOF patterns themselves are confined to the latitude band in which they were computed, the PCs provide scalar indices of the temporal variability associated with each mode. To examine how this variability projects onto the full flow, we regressed the PC time series against the meridional wind anomaly field at every gridpoint across the larger domain. This pointwise regression produces a spatial map of the teleconnection structure dynamically linked to each mode, including regions outside the latitude bands originally used for the EOF calculation. Within the original computation domains, the regressed fields reproduce the regional EOF patterns, while outside they reveal the remote responses that co vary with the same PC. In this way, the regression does not extend the EOFs themselves but rather maps how the variability captured by each regional mode manifests across the wider flow

field, thereby clarifying how subtropical and midlatitude patterns combine to reconstruct the full-domain variability.

To examine the temporal evolution of the CGT pattern, we employ a phase-resolved compositing framework in which analogues are grouped according to their angular position along the leading EOF phase space. Each composite panel is labeled by latitude band ("subtropics" or "midlatitudes") and phase bin, expressed in units of $1/4\pi$, ranging from $0/4\pi$ to $3/4\pi$. The phase coordinate, derived from the arctangent of the first two EOF principal components, defines the position of a flow state along the wavenumber-5 CGT oscillation. For example, the $0/4\pi$ phase is typically aligned with a reference ridge or trough, while $1/4\pi$ and $2/4\pi$ correspond to 90° and 180° shifts along the phase circle, respectively, enabling discrete snapshots of wave propagation across the domain.

This approach provides a dynamic view of CGT variability by decomposing the phase evolution of the dominant teleconnection mode. By associating each phase segment with a distinct subset of analogues, we produce composite anomaly maps of streamfunction and geopotential height that reveal the evolving structure of the wave train. The resulting composites highlight spatial transitions in wave amplitude, zonal position, and coherence [Sandler and Harnik, 2020].

We then projected daily wind anomalies at 300 hPa onto the EOF modes to generate a reduced phase space. Points exhibiting high projection amplitudes defined as those lying beyond twice the standard deviation from the origin in the EOF space were considered to represent strong CGT signatures. These high amplitude points formed the reference set for analogue pair selection.

For each reference point $\mathbf{x}_r$ in the reduced space, we identified its closest analogue $\mathbf{x}_a$ as:

$$\mathbf{x}_a = \arg\min_{\mathbf{x}_i} \{\|\mathbf{x}_i - \mathbf{x}_r\|\}, \quad \mathbf{x}_i \in \mathcal{X}, \quad i \neq r. \tag{2.11}$$

Here, $\mathcal{X}$ denotes the set of all projected high-amplitude states. This defines a set of analogue pairs $\{(\mathbf{x}_r, \mathbf{x}_a)\}$ across the full dataset.

To quantify predictability, we tracked the Euclidean distance $D(t)$ between the trajectories of each analogue pair over the following 20 days:

$$D(t) = \|\mathbf{x}_r(t) - \mathbf{x}_a(t)\|, \quad t = 1, 2, \ldots, T. \tag{2.12}$$

This approach evaluates how closely analogue pairs evolve over time and thus serves as a proxy for predictability. All analyses were conducted both in a 2 - dimensional phase space (EOF1 and EOF2) for subtropics and midlatitudes, and in an extended 4 - dimensional phase space combining both regions.

2.3.3 Results and Interpretation

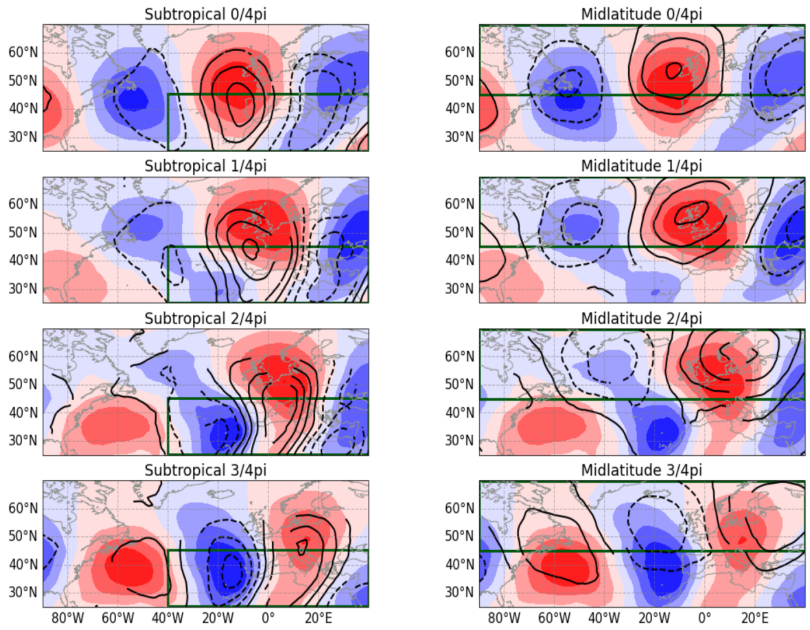


Figure 2.1: climatological mean DJF 300 hPa meridional wind field (in m/s), constructed for distinct CGT phase bins and latitude bands. Panels on the left correspond to the subtropical domain (20°N-45°N), and those on the right to the mid latitude domain (45°N-70°N). Each row represents a different phase of the dominant CGT wave pattern, progressing in $1/4\pi$ increments from $0/4\pi$ to $3/4\pi$. The colour gradient represents the flow structure of the entire domain where as black contours represents subtropical or midlatitude domains with solid (dashed) lines indicating positive (negative) values respectively.

The first and second empirical orthogonal functions (EOFs) derived from 300 hPa meridional wind anomalies collectively explain over 50% of the total variance, capturing the dominant mode of variability corresponding to the Circumglobal Teleconnection (CGT) pattern. In Figure 2.1, shaded red and blue regions denote centers of positive and negative meridional wind anomalies associated with this leading mode. The overlaid contours represent regional EOFs computed separately within predefined subtropical and midlatitude latitude bands (as indicated by green boxes).

Notably, the EOF structures obtained from the subtropical region (left panel) exhibit strong spatial alignment with the leading modes of the full domain, although the anomaly centers are slightly displaced equatorward. In contrast, the midlatitude EOF patterns (right panel) show a poleward shift in anomaly centers relative to the domain-wide EOFs.

These spatial discrepancies underscore that the CGT pattern manifests differently across latitudinal bands, implying region specific dynamical behavior and atmospheric responses.

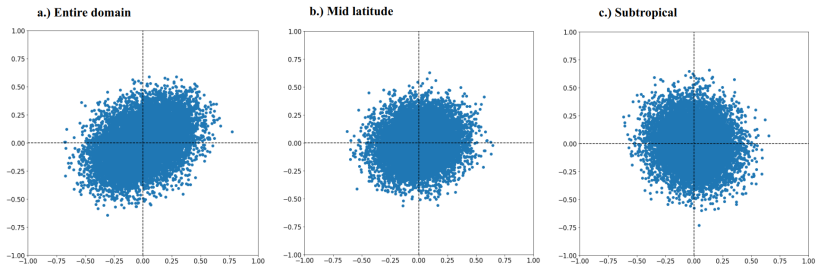


Figure 2.2: daily subseasonal anomalies of meridional wind at 300 hPa projected onto the first two leading EOF modes (EOF1 and EOF2) during DJF (1979–2019). The projections are shown for (a) the entire analysis domain, (b) the midlatitude sector, and (c) the subtropical sector. Each point represents the normalized projection amplitude for a given day.

To further investigate the persistence and predictability of these EOF-derived circulation patterns, we projected the daily 300 hPa meridional wind anomalies onto the first two EOFs. Days with large projection magnitudes were selected to represent prominent realizations of the EOF structures, either individually or in combination. The resulting distribution of projected points is visualized in Figure 2.2, with separate analyses for the entire domain, midlatitude, and subtropical regions. For the full domain, the projected anomalies cluster in an elliptical pattern, primarily occupying the first and third quadrants, indicative of a preferred phase alignment between the leading modes. In contrast, projections onto the regional EOFs exhibit more isotropic, nearly circular distributions, with points more evenly dispersed across all quadrants. The outermost points in each projection space are identified as the most strongly projected instances (as in figure 2.3), corresponding to days when the atmospheric state most closely resembles the canonical CGT like structure described by the leading EOFs.

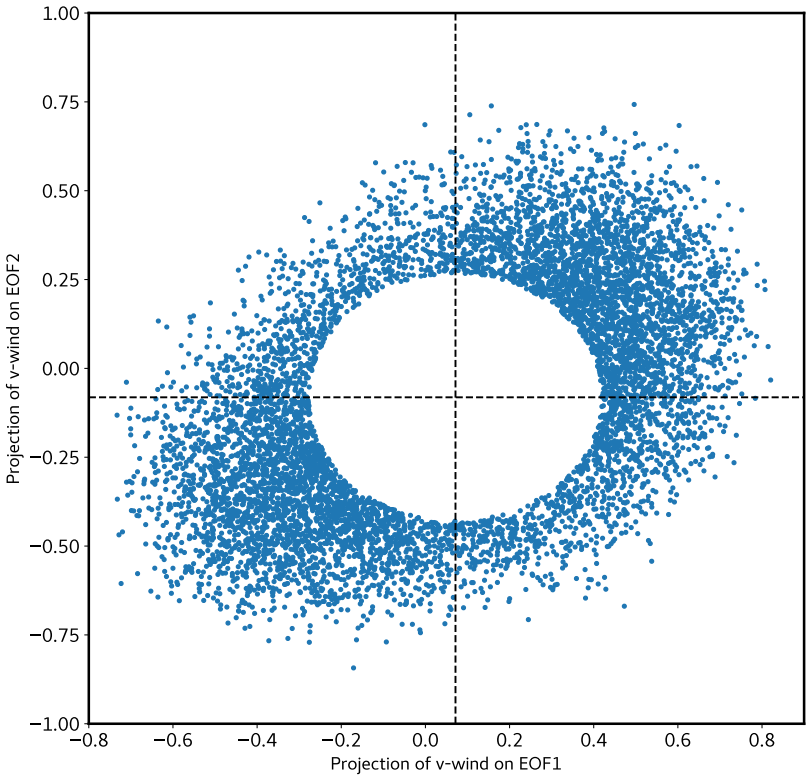


Figure 2.3: Highly projected points selected for the entire domain following the methodology provided in section 2.3.2

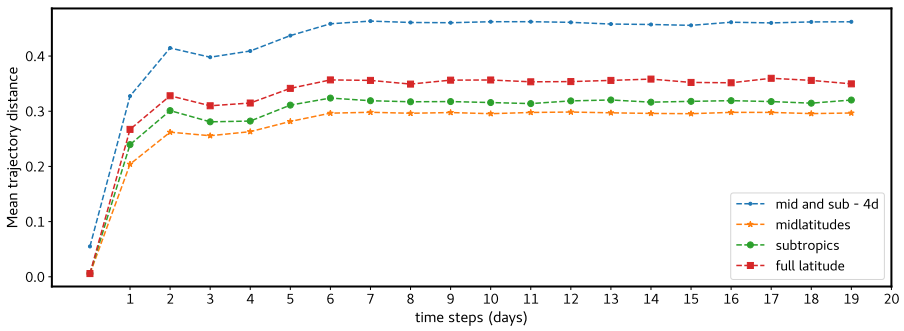


Figure 2.4: Mean trajectory distance between reference-analogue points with respect to the day of evolution

In Figure 2.4, Mean distance between trajectories of the reference-analogue points in different study area are depicted. As you can observe, no matter what the geographical area considered, the system getting saturated by 6th day. Even though the result is inconclusive this study become stepping stone of the methodology I used in my second paper which is explained explicitly in chapter 4.

2.4 Liang - Kleeman Information Transfer Index: Theoretical Formulation

To move beyond statistical association and toward a more mechanistic understanding, we now turn to a causal inference framework grounded in dynamical systems theory. Specifically, we utilize the Liang - Kleeman information transfer index to quantify the direction and magnitude of influence from key physical variables on the evolution of Atmospheric blocking in idealized version and CMIP6 MIROC6 simulations.

Unlike traditional correlation-based or regression approaches, the Liang - Kleeman framework derives directional information flow rigorously from first principles and can be applied directly to observational or model-derived time series. This allows us to identify and compare the relative dynamical drivers of western versus eastern blocking events, offering insight into why their predictability and persistence differ.

This section introduces the theoretical basis of the Liang-Kleeman index, outlines the methodological steps for its application to atmospheric datasets, and presents key results that help elucidate the causal architecture governing blocking behavior.

The Liang - Kleeman index quantifies directional information flow between components of a dynamical system. Unlike empirical or heuristic causality measures, this formulation is derived rigorously from first principles in stochastic dynamical systems theory [Liang and Kleeman, 2005; Liang, 2008, 2014, 2016].

2.4.1 Forward Problem: Information Flow in Stochastic Systems

Consider a continuous-time stochastic differential equation (SDE) system of the form:

$$d\mathbf{X} = \mathbf{F}(\mathbf{X}, t)\, dt + \mathbf{B}(\mathbf{X}, t)\, d\mathbf{W}, \tag{2.13}$$

where $\mathbf{X} = (X_1, \ldots, X_d)^\top \in \mathbb{R}^d$, $\mathbf{F} \in \mathbb{R}^d$ is the drift vector, $\mathbf{B} \in \mathbb{R}^{d\times m}$ is the diffusion matrix, and $\mathbf{W} \in \mathbb{R}^m$ is an m-dimensional Wiener process. From a physical perspective, the stochastic differential equation in Eq. 2.13 describes the time evolution of a system whose dynamics arise from the interplay between deterministic laws and random fluctuations. The drift term, $\mathbf{F}(\mathbf{X}, t)\, dt$, represents the systematic tendency of the system to evolve according to underlying physical processes, such as advection, dissipation, or restoring forces. The diffusion term, $\mathbf{B}(\mathbf{X}, t)\, d\mathbf{W}$, accounts for the unresolved or inherently random influences acting on the system, which in geophysical contexts can represent small-scale turbulence, external noise, or variability from neglected degrees of freedom.

In this way, the SDE framework provides a coarse-grained yet physically consistent representation of complex systems, bridging deterministic dynamics with stochastic forcing [Nicolis and Nicolis, 2012]. It allows us to track not only the mean trajectory of the system but also the uncertainty and variability induced by stochastic perturbations, thereby offering a natural setting for studying information flow and causality in multiscale physical systems.

The marginal entropy of X_i, denoted $H_i(t)$, evolves according to:

$$\frac{dH_i}{dt} = \text{contribution from } X_j + \text{contributions from other components}, \tag{2.14}$$

which motivates defining the information flow from X_j to X_i as the rate of change in H_i directly attributable to X_j.

2.4.2 Rigorous Definition of Information Flow

Consider a dynamical system represented by the stochastic differential equation

$$\frac{dX_i}{dt} = F_i(\mathbf{X}, t) + \sum_k b_{ik}(\mathbf{X}, t)\, \dot{W}_k, \tag{2.15}$$

where F_i is the deterministic drift term, b_{ik} the stochastic forcing coefficients, and $\dot{W}_k$ denotes Gaussian white noise.

Within this framework, the information flow $T_{j\to i}$ from variable X_j to X_i is rigorously defined as [Liang and Kleeman, 2005; Liang, 2014]:

$$T_{j\to i} = -\mathbb{E}\left[\frac{1}{\rho_i}\int \frac{\partial(F_i\rho_{\setminus j})}{\partial x_i}\, d\mathbf{x}_{\setminus i\setminus j}\right] + \frac{1}{2}\mathbb{E}\left[\frac{1}{\rho_i}\int \frac{\partial^2(g_{ii}\rho_{\setminus j})}{\partial x_i^2}\, d\mathbf{x}_{\setminus i\setminus j}\right], \tag{2.16}$$

where ρ_i is the marginal density of X_i, $\rho_{\setminus j}$ the joint density excluding X_j, and $g_{ii} = \sum_k b_{ik}^2$ the variance of the diffusion term for X_i.

In the special case of a two-dimensional linear system,

$$\dot{X}_1 = f_1 + a_{11}X_1 + a_{12}X_2 + \eta_1, \qquad \dot{X}_2 = f_2 + a_{21}X_1 + a_{22}X_2 + \eta_2, \tag{2.17}$$

with additive Gaussian noise η_i, the estimator of information flow from X_2 to X_1 can be expressed in closed form using sample covariances:

$$\widehat{T}_{2\to 1} = \frac{C_{11}C_{12}C_{2,\dot{1}} - C_{12}^2 C_{1,\dot{1}}}{C_{11}^2 C_{22} - C_{11}C_{12}^2}, \tag{2.18}$$

where C_{ij} denotes the covariance between X_i and X_j, and $C_{i,\dot{j}}$ the covariance between X_i and $\dot{X}_j$.

This formula provides a consistent estimator of the causal influence between variables in a linear stochastic system. It avoids assumptions of linear predictability as in Granger causality and is directly derived from the underlying dynamics of the system.

2.4.3 Properties of the Liang - Kleeman Index

The Liang-Kleeman information flow index possesses several mathematically and physically rigorous properties that distinguish it from traditional correlation-based approaches. First and foremost, the index is inherently *asymmetric*, meaning that the information flow from variable X_j to X_i is not necessarily equal to that from X_i to X_j. This asymmetry is a critical feature for inferring directionality in causal interactions. Moreover, while causality as defined in this framework generally implies some degree of statistical correlation, the converse is not true, high correlation does not imply causality. This distinction is essential in multivariate systems where apparent associations may arise from shared influences or confounding factors. Another important property is the concept of *nil causality*: if the evolution equation of a variable X_i (i.e., its drift term F_i) is independent of another variable X_j, then the information flow $T_{j\to i}$ will be exactly zero. This makes the index structurally sensitive to the true underlying dynamics. Finally, since the index can be estimated using a maximum likelihood formulation, it admits rigorous statistical inference. In particular, confidence intervals can be constructed from the Fisher information matrix, allowing for robust significance testing of inferred causal links.

2.4.4 Practical Estimation from Time Series

To implement the Liang - Kleeman information flow index using real-world time series data, a straightforward yet rigorous procedure is followed. First, the discrete time derivative $\dot{X}_i$ of each variable is estimated using forward differencing, typically by computing the change over a short interval $k\Delta t$, where $k \in \mathbb{N}$ and Δt is the sampling time step. This approximation is necessary because the theoretical formulation requires instantaneous rates of change, which are not directly observable from discrete observations; forward differencing provides a simple and consistent way to recover these quantities from sampled data. Next, the necessary covariances are computed from the data: specifically, the covariance between each variable and its time derivative ($C_{i,j}$), and the covariances between the variables themselves (C_{ij}). These statistical quantities are then substituted into the analytical expression for the Liang - Kleeman estimator (Eq. (2.18)), yielding a direct estimate of the directional information flow $\widehat{T}_{j\to i}$. This approach has been validated extensively on both linear and nonlinear dynamical systems, including stochastic differential equations and chaotic models, and has demonstrated robustness in various application domains such as climate science, neuroscience, and financial systems [Liang, 2014, 2021a].

2.5 Application of the Liang - Kleeman Information Flow Index to Blocking Events

To investigate the underlying the contrast in the variability of atmospheric blocking over the North Pacific, we employed the Liang - Kleeman Information Flow (LKIF) index to quantify directional causal interactions among key energy-related and thermodynamic variables. In particular, we focused on diagnosing the role of Available Potential Energy (APE), Kinetic Energy (KE), and near-surface Ground Temperature (GT) in variability

of blocking systems. The analysis was conducted separately for eastern and western blocks, motivated by earlier results from analogue-based methods that suggested marked differences in their stability characteristics.

2.5.1 Data and Preprocessing

The analysis was based on time series extracted from CMIP6 MIROC6 historical simulations as well as from a land - tmosphere coupled model corresponding to pre-identified blocking events. The MIROC6 model is the sixth-generation version of the Model for Interdisciplinary Research on Climate (MIROC), developed jointly by Japanese institutions including the University of Tokyo, JAMSTEC, and the National Institute for Environmental Studies. As part of the Coupled Model Intercomparison Project Phase 6 (CMIP6), MIROC6 provides state of the art simulations of past, present, and future climate, incorporating improved representations of atmospheric dynamics, ocean circulation, and land processes [Tatebe et al., 2019a]. For each event, daily values of APE, KE, and GT were computed and aggregated to construct continuous time series for each blocking regime (i.e., western vs. eastern blocks). The methodology for this study is explained in detail in chapter 5.

Prior to causal analysis, each time series was tested for weak stationarity using linear trend diagnostics. Specifically, a least-squares regression model of the form

$$X(t) = \alpha + \beta t + \epsilon(t), \tag{2.19}$$

was fitted to each time series, where β denotes the linear trend coefficient. A time series was considered approximately stationary if the slope was statistically indistinguishable from zero at the $\alpha = 0.01$ significance level. Here, weak stationarity refers to the property that the mean and variance of the series remain finite over time and that the covariance depends only on the time lag, not on the absolute time. This precondition ensures the validity of subsequent causal inference steps.

2.5.2 Causal Inference via the Liang-Kleeman Index

To quantify the directional causal interactions among the Lorenz Energy Cycle (LEC) reservoirs and ground temperature anomalies, the Liang - Kleeman information flow index was employed in its continuous time multivariate linear form [Liang and Kleeman, 2005; Liang, 2014, 2021b]. For a system of interacting variables $\{X_i(t)\}$, the absolute rate of information transfer from variable X_j to variable X_i is expressed as:

$$T_{j\to i} = \frac{1}{\det(\mathbf{C})} \sum_{k=1}^{d} \Delta_{jk}\, C_{k,di}\, \frac{C_{ij}}{C_{ii}}, \tag{2.20}$$

where $\mathbf{C}$ is the covariance matrix of all variables under consideration, d is the total number of variables, Δ_{jk} represents the cofactors of $\mathbf{C}$, $C_{k,di}$ is the sample covariance between variable X_k and the time derivative of X_i, C_{ij} is the covariance between X_i and

X_j, and C_{ii} is the variance of X_i. The resulting quantity $T_{j\to i}$ has units of information per unit time and quantifies the *directional rate at which uncertainty (entropy)* in X_i is influenced by X_j. Positive values indicate that X_j increases the uncertainty (entropy rate) of X_i, whereas negative values denote a stabilizing or constraining effect.

In this study, the state vector is constructed as:

$$\mathbf{X}(t) = \begin{bmatrix} \mathsf{APE}(t) \\ \mathsf{KE}(t) \\ \mathsf{GT}(t) \end{bmatrix}, \quad \dot{\mathbf{X}}(t) = \begin{bmatrix} \dot{\mathsf{APE}}(t) \\ \dot{\mathsf{KE}}(t) \\ \dot{\mathsf{GT}}(t) \end{bmatrix},$$

where **APE** and **KE** represent the available potential and kinetic energy reservoirs of the LEC, respectively, and **GT** denotes ground temperature. The derivatives $\dot{\mathbf{X}}(t)$ are estimated using finite-difference approximations. This formulation enables the identification of *directional causal pathways* and the strength of energetic linkages among the LEC components and surface temperature variability.

2.5.3 Uncertainty Quantification and Significance Testing

The LKIF estimator was applied to each realization, enabling the construction of confidence intervals for every pairwise information flow estimate. A threshold of 2.58σ (corresponding to the 99% confidence interval) was applied to test the statistical significance of each directional link.

In parallel, Pearson correlation coefficients R_{ij} were computed for each pair of variables to contrast symmetric statistical dependencies with asymmetric causal flows. While correlation captures mutual association, it lacks directionality and may obscure driver response asymmetries thus making the LKIF framework uniquely suited for identifying directional influence in the multivariate dynamics of atmospheric blocks.

The resulting matrices of information flow $\widehat{T}_{j\to i}$ and correlation R_{ij} were then compared across eastern and western blocking regimes, enabling a physically grounded interpretation of the dynamical drivers contributing to their differing predictability and persistence. This methodology enables a rigorous causal decomposition of dynamical interactions influencing blocking regimes and forms a key step toward understanding why eastern blocks exhibit weaker persistence compared to their western counterparts.

Through the discussions presented so far, the theoretical background, modeling hierarchy, and methodological tools have been introduced with the aim of providing a clear foundation for the analyses that follow. The reader has now been equipped with the essential concepts ranging from the physical basis of midlatitude dynamics to the dynamical systems frameworks and diagnostic approaches such as Lyapunov exponents, analogue techniques, and causality analysis that underpin this research.

I hope that this overview has offered sufficient context to appreciate the motivation and reasoning behind the choices made throughout this work. The next three chapters (Chapters 3, 4, and 5) present the main results obtained from the investigations conducted

over the past several years, combining idealized modeling and comprehensive simulations to quantify the predictability and variability of atmospheric blocking. I encourage the reader to follow these chapters closely, as each builds upon the concepts established here to reveal how nonlinear dynamics shape one of the most intriguing and challenging phenomena in the midlatitude atmosphere.

Chapter 3

Variability and Predictability of a reduced-order land atmosphere coupled model

---

This chapter is based on the following paper, published in Earth System Dynamics:

Xavier, A. K., Demaeyer, J., and Vannitsem, S.: Variability and predictability of a reduced-order land–atmosphere coupled model , *Earth Syst. Dynam.*, 15, 893–912, https://doi.org/10.5194/esd-15-893-2024, 2024.

Abstract

This study delves into the predictability of atmospheric blocking, zonal, and transition patterns utilizing a simplified coupled model. This model, implemented in Python, emulates midlatitude atmospheric dynamics with a two-layer quasi-geostrophic channel atmosphere on a beta-plane, encompassing simplified land effects. Initially, we comprehensively scrutinize the model's responses to environmental parameters like solar radiation, surface friction, and atmosphere-ground heat exchange. Our findings confirm that

the model faithfully replicates real-world Earth-like flow regimes, establishing a robust foundation for further analysis. Subsequently, employing Gaussian mixture clustering, we successfully delineate distinct blocking, zonal, and transition flow regimes, unveiling their dependencies on surface friction. To gauge predictability and persistence, we compute the averaged local Lyapunov exponents for each regime. Our investigation uncovers the presence of zonal, blocking, and transition regimes, particularly under conditions of reduced surface friction. As surface friction increases further, the system transitions to a state characterized by two blocking regimes and a transition regime. Intriguingly, periodic behavior emerges under specific surface friction values, returning to patterns observed under low friction coefficients. Model resolution increase impacts the system in a way that only two regimes are then obtained with the clustering: the transition phase disappears and the predictability drops to roughly 2 days for both of the remaining regimes. In accordance with previous research findings, our study underscores that when all three regimes coexist, zonal patterns exhibit a more extended predictability horizon compared to blocking patterns. Remarkably, transition patterns exhibit reduced predictability when coexisting with the other regimes. In addition, within a specified range of surface friction values where two blocking regimes are found, it is observed that blocked atmospheric situations in the west of the applied topography are marked by instabilities and reduced predictability in contrast to the blockings appearing on the eastern side of the topography.

In this study, we investigate how midlatitude circulation alternates between blocking, zonal, and transition regimes and how predictable each regime is. Using an idealized land - atmosphere coupled (quasi-geostrophic) model, we simulate *'earth like'* variability and classify the model's daily states into distinct regimes with Gaussian mixture clustering. We then quantify regime dependent stability and forecast horizons by computing local (backward) Lyapunov exponents along the trajectory. This framework allows us to compare error growth characteristics and persistence across regimes and to identify which flow configurations are intrinsically more (or less) predictable.

3.1 Introduction and motivation

Low-Frequency Variability (LFV) encompasses a wide range of atmospheric and climate processes, including atmospheric blockings, heat waves, cold spells, and long-term oscillations like the Madden-Julian Oscillation (MJO), the North Atlantic OScillation (NAO), and the El-Ni/ño - Southern Oscillation (ENSO). Despite extensive research, a comprehensive understanding of the nature of these LFVs remains elusive. In practical terms, exploiting these LFVs to achieving accurate extended-range forecasts beyond two weeks at midlatitudes remains a formidable challenge. On the climate front, comprehending how climate change affects the low-frequency variability of the atmosphere also remains

an area of incomplete knowledge. Previous works, as reported in Ghil and Robertson [2002b], Lucarini and Gritsun [2020], have highlighted this gap in understanding.

Blocking systems - a notable form of LFV observed in the atmosphere - can be described as long-lasting, quasi-stationary flow patterns in the troposphere [Liu, 1994a]. These patterns are characterized by a significant meridional flow component, leading to a disruption or deceleration of the zonal westerly flow at midlatitudes [Nakamura and Huang, 2018]. While the blocking systems persist, strong zonal flows may simultaneously exist to the north and south of them. The evolution of blocking systems involves transitions between more zonal and more meridional flow patterns during their onset and decay phases, posing challenges for forecast models [Frederiksen et al., 2004]. Moreover, the dynamics of blocking systems are complex, involving interactions across different spatial and temporal scales, both internally within the system and with the surrounding flow environment [Shutts, 1983; Lupo and Smith, 1995]. Researchers have highlighted the intricate nature of these dynamics and the connections between various scales, contributing to the challenges in understanding and predicting the behavior of blocking systems. As blocking systems have the potential to induce weather extreme like heatwaves, there is a notable interest in understanding how the characteristics of these blocking events might evolve in the future and how such changes could subsequently impact the occurrence and features of surface extreme weather events. The investigation of these potential changes is of significant importance to assess the risks associated with extreme weather events and to enhance our understanding of the complex interactions between blocking patterns and surface weather conditions in a changing climate context [Kautz et al., 2022].

Eventhough the concerns above matters, identifying and evaluating LFVs in GCMs is computationally expensive, so in this study an idealised reduced order coupled model is used. It is a climate model 'stripped to the bone', which links theoretical understanding to the complexity of more realistic models, made by key ingredients and approximations; which hence helps us to study a particular phenomenon by tweaking the parameters affecting them with less computational cost. The pursuit of simplified models for atmospheric phenomena has a long history, dating back to Lorenz's seminal work in the early 1960s [Lorenz, 1960, 1962, 1963a,b]. This approach recognizes the value of sacrificing some detail in exchange for a deeper grasp of fundamental physical processes.

Lorenz demonstrated the power of this strategy by leveraging Fourier series to distill the barotropic vorticity equation into three ordinary differential equations [Lorenz, 1960]. These equations, while omitting smaller scales of motion, yielded valuable insights into atmospheric scenarios such as flow interactions and current stability. Subsequently, he developed a simplified geostrophic model using truncated Fourier-Bessel series [Lorenz, 1962]. This eight-equation model captured baroclinic instability, a critical process in atmospheric dynamics, while maintaining key energy relationships. Notably, the model successfully reproduced observed flow regimes and transitions in rotating fluids, suggesting its effectiveness in studying large-scale atmospheric behavior. Lorenz's 1963 research yielded significant advancements in our understanding of atmospheric dynamics through two key publications [Lorenz, 1963a]. The first introduced a now-iconic system of three differential equations, derived from a further simplified model for fluid flow. This groundbreaking

work unveiled the concept of sensitive dependence on initial conditions, a cornerstone of chaos theory.

In the same year, Lorenz explored a separate avenue by investigating a simplified model for symmetrically heated rotating viscous fluids [Lorenz, 1963b]. This work resulted in a system of fourteen ordinary differential equations governed by two external parameters: the thermal Rossby number and the Taylor number. Analytical solutions revealed the existence of purely zonal flow and superimposed steady waves, while numerical integration unveiled a richer tapestry of flow behaviors. Oscillatory solutions with periodic shape changes and irregular non-periodic flow emerged. Interestingly, increasing the Taylor number generally led to greater flow complexity, except at very high values where the model's truncations became unrealistic.

Perhaps most intriguing was the coexistence of unstable purely zonal, steady-wave, and oscillatory solutions. This suggests intricate flow dynamics, with transitions between symmetric and unsymmetric vacillation occurring independently of instability. These findings highlight the ability of simplified models to unveil complex and nuanced behaviors in atmospheric dynamics [Shen et al., 2023]. Lorenz's pioneering work in the early 1960s demonstrated the power of simplified models for understanding atmospheric dynamics. By strategically neglecting certain complexities, he was able to capture key phenomena like baroclinic instability and chaos. However, for large-scale atmospheric simulations, computational efficiency becomes paramount. This is where Qg (quasi-geostrophic) models come in. Qg models prioritize large-scale features by making specific approximations, allowing for rapid simulations and analyses of broad atmospheric circulation patterns. While they may not capture the intricate details explored by Lorenz's models, Qg models remain a workhorse for studying large-scale atmospheric phenomena. Hence the trend continued with Charney and DeVore [1979] in which a quasi-geostrophic model, projected onto Fourier modes for a more efficient and concise representation, has been developed. It also incorporates an idealized parameterization closure to account for subgrid-scale processes. By imposing in addition a meridional temperature gradient over a topography, the model becomes a forced-dissipative system, which exhibits multiple stable equilibria, representing distinct atmospheric flow patterns. Charney and Devore hypothesized that the transitions between these solutions were primarily influenced by small-scale perturbations or the presence of baroclinic instability within the system.

Charney and Straus [1980] partially confirmed this hypothesis and found out that these transitions were indeed the result of baroclinic instability. Their study sheds light on the complex interactions between atmospheric flow, orography and propagating planetary waves in baroclinic systems. They discovered that the interactions between atmospheric flow and orography induces form-drag instability, generating eddies and perturbations, and leading to multiple stable equilibria with distinct flow patterns under consistent forcing conditions.

Charney's seminal study sparked significant interest in the low-order spectral model and the theory of multiple flow equilibria. Zhengxin and Baozhen [1982] and Zhu [1985] employed a two-layer low-order spectral model, discovering stable equilibrium states re-

sembling actual blocking, with zonally asymmetric thermal and topographic forcings and flow nonlinearity playing critical roles in blocking dynamics. The summarized version of the evolution of numerical weather prediction and predictability tools are included in Yoden [1983a,b, 2007].

Reinhold and Pierrehumbert [1982, 1985] extended Charney's model, incorporating additional synoptic-scale waves, revealing two distinct weather regime states influenced by wave-wave interactions causing transitions between equilibrium states.

Cehelsky and Tung [1987] demonstrated that the behavior of a reduced-order model exhibits notable disparities at higher resolutions, primarily attributed to the inadequate representation of energy upscaling and vorticity downscaling pathways. They coined this phenomenon as '*spurious chaos*', denoting the emergence of irregular dynamics that are not genuinely representative of the underlying physical processes. Although this is a valid point, high resolution models are usually hard to analyze in detail. There is therefore a need for investigating first reduced coupled model in order to get qualitative conclusions on a problem at hand. We started this journey by using a reduced order land atmospheric model to investigate the impact of coupling between the land and the atmosphere on LFV.

Legras and Ghil [1985] employed a higher-order barotropic spectral spherical model to investigate blocking and zonal flow regimes dynamics, suggesting that their model displayed properties akin to an index cycle, and later stochastic forcing was introduced to Charney's deterministic model, leading to transitions between high- and low-index states [Benzi et al., 1984; Egger, 1981; Sura, 2002]. The impact of stochastic forcing on the stability of atmospheric regimes was also recently considered in a highly-truncated barotropic model by Dorrington and Palmer [2023], where they provide a mechanism to explain the increased persistence of blocking due to the noise in such simple models.

Legras and Ghil [1985] also discussed the realistic existence of blocked and zonal flow regimes which are obtained as unstable stationary solutions due to the barotropic influence of the LFVs in the atmosphere. More persistent zonal flows are also identified in several occasions which seems to be a deviation from the earlier studies. Later the stability studies by Weeks et al. [1997] recreating zonal and blocked regimes in an experimental annulus setup further substantiated the findings of Legras and Ghil [1985].

Schubert and Lucarini [2016]'s numerical investigation employing a QG model revealed a counter-intuitive finding that during blocking events, the global growth rates of the fastest growing covariant Lyapunov vectors (CLVs) are significantly higher, indicating stronger instability compared to typical zonal conditions. The difficulty in predicting the specific timing of blocking onset and decay further contributes to the observed instability behavior, aligning with Kwasniok [2019] findings associating anomalously high values of finite time largest Lyapunov exponents with blocked atmospheric flows.

Lucarini and Gritsun [2020] demonstrated that blocking phenomena exhibit higher instability compared to typical atmospheric conditions, irrespective of whether they occur in the Atlantic, Pacific, or globally. This analysis utilized the simplified atmospheric model

proposed by Marshall and Molteni [1993] and assessed stability based on unstable periodic orbits (UPOs). Importantly, this research dispelled the misconception that the increased stability of zonal flows solely resulted from the barotropic nature of the model in the study of Legras and Ghil [1985] and Weeks et al. [1997] apparatus. Consistent results were obtained by Faranda et al. [2016, 2017], utilizing extreme value theory for dynamical systems, which identified blocking regimes with unstable fixed points in a heavily reduced phase space. Their findings indicated that blockings exhibit higher instability in the circulation, linked to an increased effective dimensionality of the system. This agreement with Lucarini and Gritsun [2020] study further supports the notion that blocking events display stronger turbulence and instability, challenging conventional expectations.

We here aim at extensively investigating the predictability of blocking, zonal, and transition regimes utilizing backward Lyapunov exponents (BLVs) in the context of a recently developed reduced-order land-atmosphere model, providing a more comprehensive understanding of the system's behavior and regime predictability.

The classic Charney's model lacks feedback from atmospheric flow to the artificially specified "thermal forcing," leading to potential unrealistic effects on large-scale atmospheric motions. To address this limitation, a new land atmospheric coupled model is proposed in Li et al. [2018], which incorporate an energy balance scheme to allow atmospheric motions to influence the land temperature distribution and vice-versa. By considering horizontally inhomogeneous radiative input fields as the driving force for land-atmosphere dynamics, this coupled model offers a more realistic representation of the interactions between the land and the atmosphere. The model bears resemblance to the low-order coupled ocean-atmosphere model proposed by Vannitsem et al. [2015], but with a heat bath featuring the land and an idealized topography.

Prior to conducting the investigation on the predictability of blocking, zonal, and transition regimes using backward Lyapunov exponents (BLVs), we performed a characterization of the sensitivity of the quasi-geostrophic land-atmosphere coupled model embedded in the qgs framework [Demaeyer et al., 2020] with respect to various environmental parameters that are essential for the functioning of the atmosphere.

The structure of the paper is as follows. Section 3.2 introduces the model, outlining its structure, main properties, and the parameters employed in the study. Additionally, this section includes a discussion on the stability properties of the system and temporal evolution of the modes (barotropic stream function, baroclinic streamfunction and ground temperature). In Section 3.3, the methodology used for the investigation is explained. Section 3.4 presents the stability and the Lyapunov properties of the model corresponding to various environmental factors, and in Section 3.5, predictability properties of different weather regimes are discussed. Effects of the model resolution are presented in section 3.6 and the conclusions drawn from the research are provided in section 3.7, along with future perspectives for further studies.

3.2 Land atmosphere coupled model

3.2.1 Model Characteristics

qgs is a Python framework in which several reduced-order climate models are implemented for midlatitudes [Demaeyer et al., 2020]. It models the dynamics of a 2-layer quasi-geostrophic (QG) channel atmosphere on a beta-plane, coupled to a simple surface component that could be a land or an ocean. In the current study, we are using the quasi-geostrophic land-atmosphere coupled model version [Li et al., 2018].

The atmospheric part of the model is represented as a 2-layered, quasi-geostrophic flow defined on a β plane within the zonal walls $y = 0$ and πL [Reinhold and Pierrehumbert, 1982]. The thermodynamic equations of the baroclinic atmosphere includes the energy exchanges between land, atmosphere and space similar to the radiative and heat flux scheme provided in Barsugli and Battisti [1998]. The coupling of the atmospheric components with the ground is constituted by the surface friction and the radiative and heat exchanges between the atmosphere and the ground. As usual in such types of models, channel atmosphere is considered with no-flux boundary conditions on the north and south borders and periodic boundary conditions on the east and west border.

The equations governing the time evolution of barotropic and baroclinic streamfunction of the atmospheric part are as follows:

$$\frac{\partial}{\partial t}\left(\nabla^2\psi_{\mathrm{a}}\right) + J(\psi_{\mathrm{a}}, \nabla^2\psi_{\mathrm{a}}) + J(\theta_{\mathrm{a}}, \nabla^2\theta_{\mathrm{a}}) + \tfrac{1}{2}\, J(\psi_{\mathrm{a}} - \theta_{\mathrm{a}}, f_0\, h/H_{\mathrm{a}}) + \beta\, \frac{\partial \psi_{\mathrm{a}}}{\partial x} = -\tfrac{k_d}{2}\, \nabla^2(\psi_{\mathrm{a}} - \theta_{\mathrm{a}})\,, \tag{3.1}$$

$$\frac{\partial}{\partial t}\left(\nabla^2\theta_{\mathrm{a}}\right) + J(\psi_{\mathrm{a}}, \nabla^2\theta_{\mathrm{a}}) + J(\theta_{\mathrm{a}}, \nabla^2\psi_{\mathrm{a}}) - \tfrac{1}{2}\, J(\psi_{\mathrm{a}} - \theta_{\mathrm{a}}, f_0\, h/H_{\mathrm{a}}) + \beta\, \frac{\partial \theta_{\mathrm{a}}}{\partial x} = -2\, k_d' \nabla^2\theta_{\mathrm{a}} + \tfrac{k_d}{2}\, \nabla^2(\psi_{\mathrm{a}} - \theta_{\mathrm{a}}) + \frac{f_0}{\Delta p}\, \omega\,. \tag{3.2}$$

where ω is the verical velocity of the system. ψ_a is the barotropic streamfunction and θ_a is the baroclinic streamfunction of the atmosphere. The constants k_d and k_d' multiply the surface friction term and the internal friction between layers, respectively. The temperature equation of the baroclinic atmosphere and ground are :

$$\gamma_{\mathrm{a}}\left(\frac{\partial T_{\mathrm{a}}}{\partial t} + J(\psi_{\mathrm{a}}, T_{\mathrm{a}}) - \sigma\omega\frac{p}{R}\right) = -\lambda(T_{\mathrm{a}} - T_{\mathrm{g}}) + \epsilon_{\mathrm{a}}\sigma_{\mathrm{B}}T_{\mathrm{g}}^4 - 2\epsilon_{\mathrm{a}}\sigma_{\mathrm{B}}T_{\mathrm{a}}^4 + R_{\mathrm{a}} \tag{3.3}$$

$$\gamma_{\mathrm{g}}\,\frac{\partial T_{\mathrm{g}}}{\partial t} = -\lambda(T_{\mathrm{g}} - T_{\mathrm{a}}) - \sigma_{\mathrm{B}}T_{\mathrm{g}}^4 + \epsilon_{\mathrm{a}}\sigma_{\mathrm{B}}T_{\mathrm{a}}^4 + R_{\mathrm{g}} \tag{3.4}$$

where T_g and T_a are the ground and atmospheric temperature respectively. σ is the

static stability with p as the pressure. R is the gas constant for dry air. γ_a is the heat capacity of the atmosphere for a 1000-hPa deep column where as γ_g is the heat capacity of the active layer of the land for a mean thickness of 10 m [Monin, 1986]. λ is the heat transfer coefficient between the land and atmosphere. σ_B is the Stefan-Boltzmann constant and ϵ_a is the longwave emissivity of the atmosphere. R_a is the shortwave solar radiation directly absorbed by the atmosphere whereas R_g is the shortwave solar radiation absorbed by the land. The hydrostatic relation in pressure coordinates $\frac{\partial \Phi}{\partial p} = \frac{-1}{\rho_a}$ where the geopotential height $\Phi^i = f_0 \psi_a^i$ and the ideal gas relation $p = \rho_a R T_a$ allow one to write the spatially dependent atmospheric temperature anomaly $\delta T_a = \frac{2 f_0 \theta_a}{R}$, with θ_a as the baroclinic streamfunction. This can be used to eliminate the vertical velocity ω.This changes the independent dynamical field to the streamfunction field ψ_a and the spatially dependent temperatures δT_a and δT_g. The dimensional meridional differential shortwave solar radiation absorbed by the land and the atmosphere are given by $\delta R_g = \sqrt{2} C_g \cos \frac{y}{L}$ and $\delta R_a = \sqrt{2} C_a \cos \frac{y}{L}$ respectively. Hence we decide to provide $C_a = 0.4 C_g$. The variable C_g is a dimensional parameter, which is an indicator of the meridional difference in solar heating absorbed by the land between the walls, and it is the crucial parameter in our land atmosphere coupled model. As in Vannitsem et al. [2015] and De Cruz et al. [2016], quartic terms of the temperature equations are linearised. Upon nondimensionalization, the qgs framework represents the above equations as ordinary differential equations by projecting them on to a set of basis functions, a procedure which is also known as Galerkin expansion. We investigate the (2, 2) resolution configuration of the model for the current study, which means that basis functions up to wavenumber 2 in each coordinate of the model are used. Consequently, the following list of 10 basis functions was used for the study:

$$
\begin{aligned}
F_1(x,y) &= \sqrt{2}\,\cos(y), \\
F_2(x,y) &= 2\,\cos(nx)\,\sin(y), \\
F_3(x,y) &= 2\,\sin(nx)\,\sin(y), \\
F_4(x,y) &= \sqrt{2}\,\cos(2y), \\
F_5(x,y) &= 2\cos(nx)\sin(2y), \\
F_6(x,y) &= 2\sin(nx)\sin(2y), \\
F_7(x,y) &= 2\cos(2nx)\sin(y), \\
F_8(x,y) &= 2\sin(2nx)\sin(y), \\
F_9(x,y) &= 2\cos(2nx)\sin(2y), \\
F_{10}(x,y) &= 2\sin(2nx)\sin(2y),
\end{aligned}
\tag{3.5}
$$

Each basis function represent corresponding spatial patterns.Therefore this configuration yields a set of 30 variables, including 10 barotropic variables, 10 baroclinic variables, and 10 ground temperature variables. Note that as explained in the qgs documentation, the basis functions of the model can be easily altered.In the context of this model, the instability properties, i.e. the Lyapunov vectors, are affecting all the spatial modes at once, and are therefore characterizing the spatio-temporal chaotic evolution of small perturbations. The approach adopted here is similar to the one used for instance in Vannitsem and Nicolis [1997b].

Table 3.1: Typical values of the model used for the study

Parameter	Value	Parameter	Value
a	$6371\,\mathrm{km}$	σ_B	$5.67 \times 10^{-8}\,\mathrm{W\,m^{-2}\,K^{-4}}$
πL	$5000\,\mathrm{km}$	γ_a	$1.0 \times 10^{7}\,\mathrm{J\,m^{-2}\,K^{-1}}$
H	$8.5\,\mathrm{km}$	γ_g	$1.6 \times 10^{7}\,\mathrm{J\,m^{-2}\,K^{-1}}$
ϕ_o	$50°\mathrm{N}$	λ	$10\,\mathrm{W\,m^{-2}\,K^{-1}}$
n	1.3	f_o	$1.032 \times 10^{-4}\,\mathrm{s^{-1}}$
ϵ	0.76	R	$287.058\,\mathrm{J\,kg^{-1}\,K^{-1}}$
k_d	$1.2384 \times 10^{-5}\,\mathrm{s^{-1}}$	k_d'	$2.068 \times 10^{-6}\,\mathrm{s^{-1}}$
σ	$2.158 \times 10^{-6}\,\mathrm{m^2\,s^{-2}\,Pa^{-2}}$		

Values of λ, n, and k_d are varied beyond the displayed values to study model sensitivity.

3.2.2 Model Parameters

Even though the model that we are using is a highly truncated spectral model, its comparability towards the original atmosphere and ground coupling is of great importance. Simulations produced by the model will be more meaningful if it charecterizes *earthlike* properties. This can be obtained by tweaking and tuning the model parameters. In the present scenario, the parameters used are derived from Reinhold and Pierrehumbert [1982], where they specifically estimated realistic parameter ranges that result in mid-latitude terrestrial flow characteristics and regimes. The typical dimensional parameter values used for this study are displayed in Table 3.1.

3.2.3 Model trajectories and mean fields

Figure 3.1 displays the time evolution of the first barotropic ($\psi_{a,1}$) and baroclinic ($\theta_{a,1}$) streamfunction modes of the atmosphere and the ground temperature ($T_{g,1}$) for about 10 years starting after 10000 days of transient integration. Fluctuations are more erratic in the atmospheric part, which denotes its key role in the dynamics of the system. The variable representing the land component of the system is comparatively slower and less erratic. This difference suggests that the land component has a longer typical time scale than the atmosphere in this system.

Figure 3.2(a) emphasizes the observation above, where the autocorrelation of the first barotropic atmospheric mode and the first ground temperature mode for $C_g = 300$ Wm^{-2} and $k_d = 0.085$ are displayed. These, evaluated on a time series of 10000 days, helps us estimate the memory loss of the variables.

Indeed, the typical timescale of the processes at hand can be evaluated by the e-folding time which is the time beyond which the correlation has decreased by $1/e$. As expected the e-folding time of the atmospheric part is approximately 1.9 days which is comparitatively lower than that of the land part (≈ 7.6 days) indicating that the system is a multiscale model with a typical timescale ratio of 10 for the specific parameter values considered.

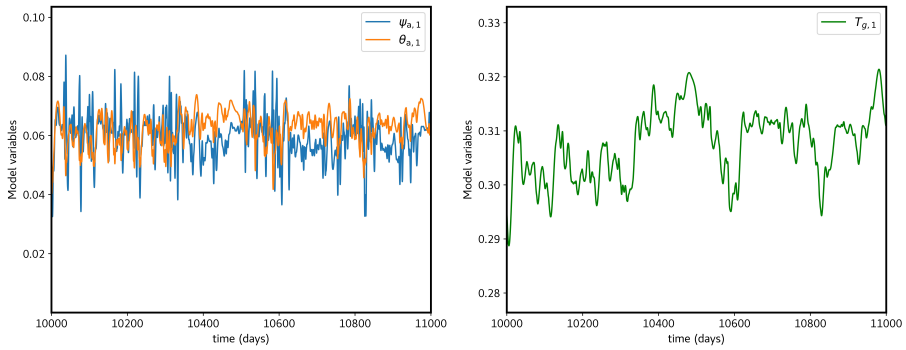


Figure 3.1: Temporal evolution of barotropic (ψ_{a1}) and baroclinic (θ_{a1}) atmospheric streamfunction and the ground temperature (T_{g1}) for $C_g = 300\ Wm^{-2}$ and $k_d = 0.085$.

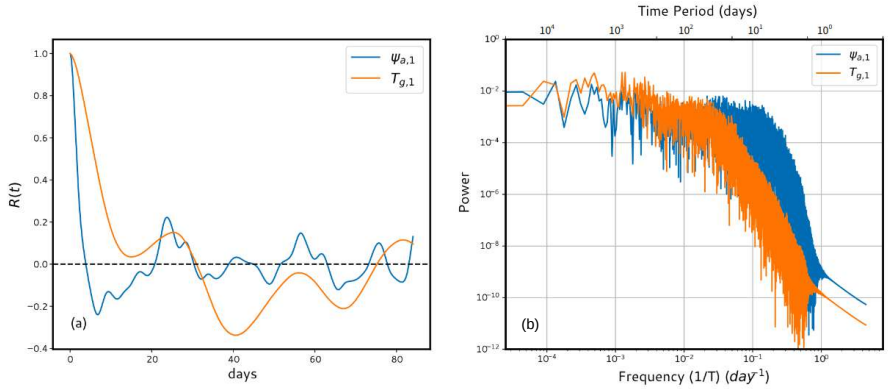


Figure 3.2: (a) Autocorrelation of barotropic (ψ_{a1}) atmospheric streamfunction and the ground temperature (T_{g1}) for $C_g = 300\ Wm^{-2}$ and $k_d = 0.085$. (b) Powerspectrum of the same variables.

Figure 3.2(b) is depicting the power spectra of modes $\psi_{a,1}$ and $T_{g,1}$ calculated by the Fourier transformation of the autocorrelation function using again timeseries of 10000 days. Atmospheric mode has a flat spectrum for lower frequencies and decays rapidly for higher frequencies. The spectrum for the ground mode is initially following the path of the atmosphere (lower frequencies up to 0.001) but starts to decay earlier which indicates more structured variabilities at lower frequencies than the atmosphere. The existence of a substantial continuous part in the spectrum is an indication of the complexity of the deterministic dynamics in time and suggests the presence of a chaotic dynamics [Arbabi and Mezić, 2017; Mezić, 2020].

3.3 Methodology

The objective of this research - besides introducing the basic equations, energy balance scheme and its sensitivity - is to explore the predictability of blocking and zonal weather regimes. By analyzing the peculiarities and the patterns of the land atmospheric coupled model, the study concludes that, when utilizing the parameters described in section 3.2.2, the system shows a qualitatively similar behaviour as the large scale actual atmosphere at midlatitudes (examples are illustrated in Appendix A.2). Moreover, varying the surface friction term, k_d, within the range of 0.06 to 0.12 yields numerous instances of realistic flow regimes, including blocking, zonal, and transition phases between these two states. To isolate between these flow regimes, a machine learning algorithm called Gaussian Mixture Clustering (GMC) is employed, which will be described in Appendix A.1. After classifying the data, the average geopotential height at 500 hPa of each cluster is calculated to identify different flow regimes. Through experimentation encompassing 2 to 6 clusters, discernible flow regimes emerged for 2 and 3 clusters, showcasing significant distinctions. However, as the cluster count reached 4, we noted convergence between two clusters, leading to identical structures and flow patterns. This trend persisted with additional cluster increments. Hence, we inferred that the attractor attained optimal clustering with evident and nearly uniform data point distribution when employing 3 clusters. Each flow regime is equally important due to its presence in the actual atmosphere. The cluster containing the lowest fraction of points in percentage being designated as the transition regime. The predictability horizon of each regime is evaluated by computing the inverse of the average largest local Lyapunov exponents of the clusters, which are calculated at each point of the attractor before clustering. Although the attractor exhibits multiple positive Lyapunov exponents, our investigation focused solely on the first exponent, as it governs the dynamics of the error and is therefore considered the most influential.

3.4 Regime stability and Lyapunov properties of the low order land atmospheric coupled model

Characterizing the instability properties of different flow regimes and their dependence with respect to important parameters are investigated as follows: The first part is exploring the sensitivity of the model about essential parameters which play a key role in structuring the output of the system. In the second part, the predictability properties of zonal, blocking and transition flow regimes using the Lyapunov exponents is investigated.

3.4.1 Stability properties of the model

Stability properties of the land-atmosphere coupled model at their equilibrium states are well depicted in Li et al. [2018]. They also defined high-index equilibria and low-index equilibria based on the value of the streamfunction in the upper and lower atmospheric layer when the model solutions are equilibrium states. Even though stability of the model's equilibrium states is interesting and insightful, the actual atmosphere displays time-dependent

solutions. Moreover, realistic atmospheric models are chaotic and acutely sensitive to the initial conditions. Hence in this section, we investigated the stability properties of the land atmosphere model when its behaviour is similar to *earthlike* situations with erratic dynamics.

Chaotic dynamical systems which exhibit sensitivity to the initial conditions can be qualitatively analysed by computing Lyapunov exponents and vectors.

3.4.2 Theory

Sensitivity to initial conditions is usually estimated using Lyapunov exponents. Let us consider an initial state, $\vec{x}(t_o) = \vec{x}_o$, a small perturbation $\delta\vec{x}_o$ is added to it which produces eventually a completely different trajectory. The dynamics of the error growth of the system can be linearized provided the perturbation is infinitesimally small as

$$\frac{d\delta\vec{x}}{dt} = \left.\frac{\partial\vec{f}}{\partial\vec{x}}\right|_{\vec{x}(t)} \delta\vec{x} \tag{6}$$

and its solution is

$$\delta\vec{x}(t) = \mathbf{M}(t, \vec{x}(t_o))\delta\vec{x}(t_o) \tag{7}$$

where $\mathbf{M}$ is known as the resolvent or propagator matrix. The Euclidean norm of the error can be computed as

$$\begin{aligned} E_t = |\delta\vec{x}(t)|^2 = \delta\vec{x}(t)^T\delta\vec{x}(t) \\ E_t = \delta\vec{x}(t_o)^T\mathbf{M}(t, \vec{x}(t_o))^T\mathbf{M}(t, \vec{x}(t_o))\delta\vec{x}(t_o) \end{aligned} \tag{8}$$

hence indicating that the error growth is provided by the eigenvalues of $\mathbf{M}^T\mathbf{M}$, where $\mathbf{M}^T$ denotes the transpose of the resolvent matrix $\mathbf{M}$. By the multiplicative ergodic theorem of Oseledec [Eckmann and Ruelle, 1985b; Kuptsov and Parlitz, 2012], a double limit is considered with perturbation amplitude going to 0 and time going to infinity. The logarithm of the eigenvalues of matrix $(\mathbf{M}^T\mathbf{M})^{2(t-t_o)}$ within these limits, which are known as Lyapunov exponents, quantifies the divergence of the initially close trajectories. The complete set of Lyapunov exponents that are usually represented in decreasing order constitutes the Lyapunov spectrum. Different types of Lyapunov vectors existed based on the method of calculation like forward Lyapunov vectors, backward Lyapunov vectors and covariant Lyapunov vectors whose properties are described in details in [Kuptsov and Parlitz, 2012; Legras and Vautard, 1996].

In the current study, we are using backward Lyapunov vectors (BLVs) which are obtained by considering the eigenvalues of the matrix $(\mathbf{M}^T\mathbf{M})^{2(t-t_o)}$ by taking initial state $t_o \to -\infty$. Several numerical techniques exist for the calculation of the Lyapunov exponents. The most common method is using Gram-Schmidt orthonormalization [Shimada and Nagashima, 1979; Parker and Chua, 2012]: A set of orthonormal random vectors are propagated in the tangent space of the trajectory, according to equation (6), frequently re-orthonormalizing this basis to avoid the collapse of all the vectors towards the most

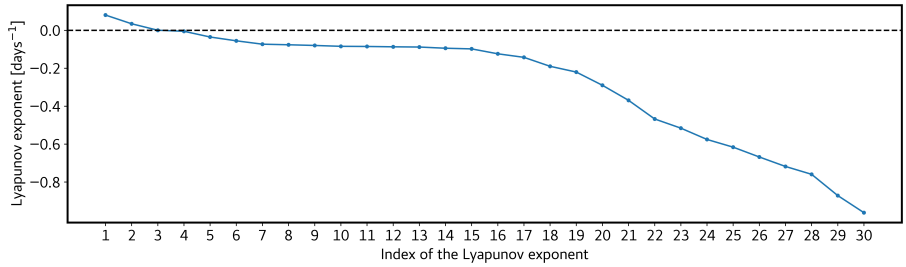


Figure 3.3: Lyapunov spectra of the land atmospheric coupled model for $C_g = 300\ Wm^{-2}$ and $k_d = 0.085$. The values of the Lyapunov exponents are given in days^{-1} .

unstable direction which is associated with the largest Lyapunov exponent. After a transient, these vectors provide the BLVs and concurrently the sought Lyapunov exponents. As Mentioned in section 3.4.2, Lyapunov exponents computed here consider both spatial and temporal chaos. The complete set of these vectors give the full picture of the instability of the trajectory in phase space.

3.4.3 Lyapunov spectra and averaged variance of the model

Figure 3.3 displays the Lyapunov spectrum of the land-atmosphere coupled model when $C_g = 300\ Wm^{-2}$ and $k_d = 0.085$. All other parameters are provided in Table 3.1. The system has 3 positive, 1 zero and 26 negative Lyapunov exponents. Similarly to the ocean-atmospheric coupled model [Vannitsem et al., 2015; Vannitsem and Lucarini, 2016; Vannitsem, 2017], the spectrum contains a set of Lyapunov exponents forming a plateau close to 0, but the amplitude of the Lyapunov exponents around this plateau is however quite substantial as compared to the coupled ocean-atmosphere model. This plateau is expected to be associated with the presence of the land whose typical time scales of variability are slower than the atmosphere.

The coupling between land and atmosphere plays a key role in the behaviour of the model. Hence quantifying the extent of this coupling and its instabilities is essential for interpreting the properties of the model. Therefore, the averaged variance of the Lyapunov vectors is displayed in figure 3.4 to elucidate this information along each variable.

The first ten variables represent the barotropic streamfunction of the atmosphere, the next ten represent the baroclinic streamfunction of the atmosphere, and the last ten represent the ground temperature. The variance of the BLVs is primarily residing in the atmospheric part, indicating that this part primarily contributes to the system's dynamics. It should also be noted that the atmospheric part includes the most unstable BLVs (corresponding to the first two Lyapunov exponents) as well as the most stable BLVs (21 to 30 corresponds to large negative LEs).

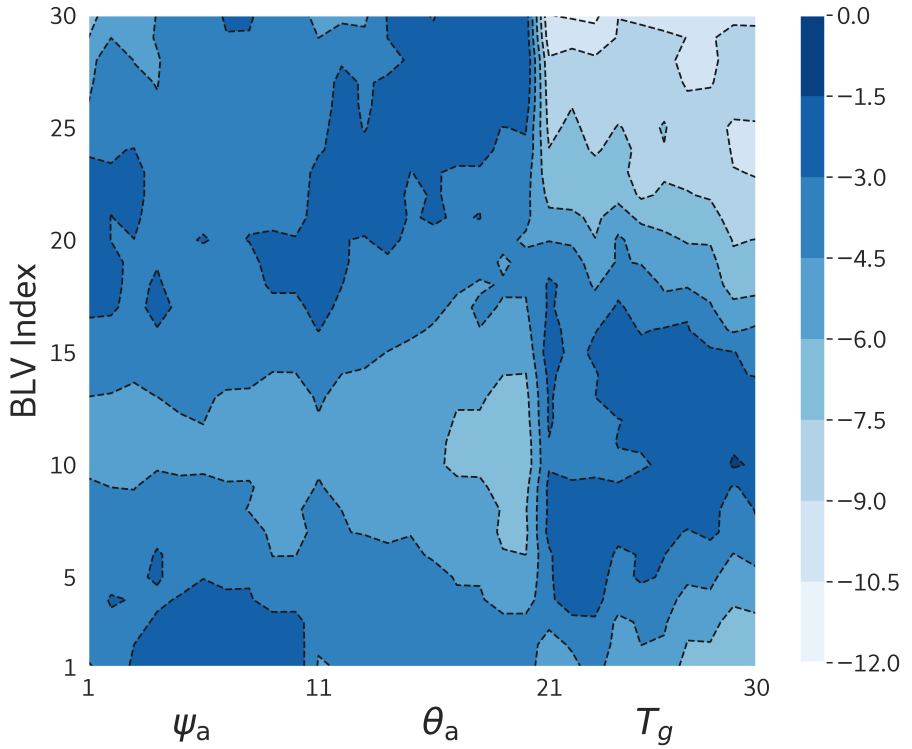


Figure 3.4: Values of the time-averaged and normalized variance of the BLVs as a function of the variables of the model (log_{10} scale). The 20 first modes correspond to the variables of the atmosphere and the next 10 ones correspond to the temperature of the ground. Parameters' value: $C_g = 300$ Wm^{-2} and $k_d = 0.085$. The Euclidean norm is used for all BLVs, and their squared norm is normalized to 1

Conversely, variance is predominantly projected on the temperature variables of the ground part for the BLVs 3 to 20. These BLVs are associated with the plateau formed by the near-zero LEs visible in Fig. 3.3. The observation of comparable variance in both the atmospheric and ground parts describes (horizontally) the coupling in the model, which is thus represented for BLVs 3-7. For BLVs 21 to 30, variance projection is almost non-existent in the ground part, indicating that the ground part makes almost no contribution to the stabilization of the system.

Figure 3.5 displays Lyapunov spectra calculated for various energy input levels (C_g) ranging from 300 to 400 Wm^{-2}.

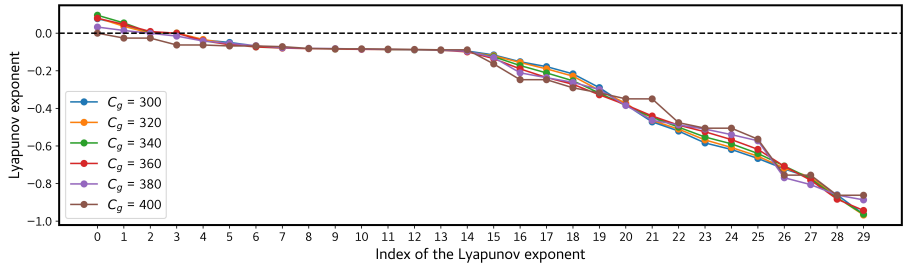


Figure 3.5: Lyapunov spectra of the land atmospheric coupled model for different values of C_g. Each color represents corresponding C_g values used for calculating the spectrum. The values of the Lyapunov exponents are given in days^{-1}

When C_g is lower, the model exhibits chaotic behavior, indicated by two positive exponents, one zero exponent, and 26 negative exponents. Surprisingly, the amount of incoming shortwave radiation doesn't significantly affect the spectrum between C_g values of 300 and 360 Wm^{-2}.

However, as C_g increases, the system shifts to periodic behavior, characterized by one zero exponent and 29 negative Lyapunov exponents, before switching back to chaos.

This is illustrated in Figure 3.6 where the first and second Lyapunov exponents are positive for the system for the lower values of C_g and then system enters in to a periodic window for the C_g values and revert back again to chaotic behaviour later.

The surface friction k_d is also affecting stability of the system to a great extent. In order to investigate the sensitivity of the model towards k_d, Lyapunov spectra were drawn with the parameter values exhibited in table 1 with different k_d values as displayed in Fig. 3.7.

The non-dimensional k_d values depicted in the figure were obtained from Reinhold and Pierrehumbert [1982], where they asserted that flow regimes generated using these values exhibit realistic midlatitude terrestrial properties. Among the system configurations with k_d values of 0.06, 0.075, 0.09, and 0.12, there are 3 positive, 1 zero, and 26 negative Lyapunov exponents. Up to the point of plateau formation, all these spectra display similar behavior. Note that the spectrum corresponding to $k_d = 0.12$ exhibits notably strong negative Lyapunov exponents, while the spectrum for $k_d = 0.06$ demonstrates comparatively weaker negative values, as expected from the increased associated dissipation.

From Figure 3.4, we identified that BLVs 20 - 30 are actually depicting the variance of temperature of the atmosphere. Given the significant variation in BLVs 20 - 30 within the current context, it can be inferred that the atmospheric temperature gradient, and hence baroclinic instability is becoming weaker and the system is stabilizing due to the changes in the surface friction.

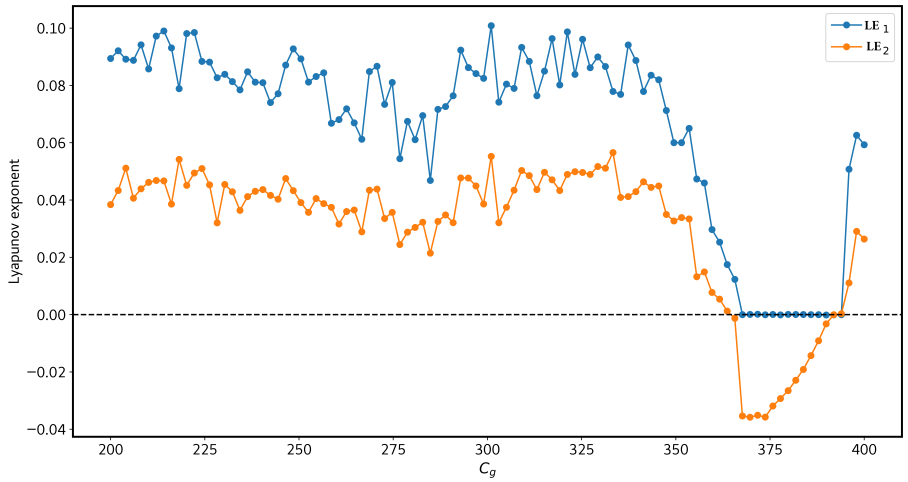


Figure 3.6: First and second Lyapunov exponents of the land atmospheric coupled model for different values of C_g for a fixed value of $k_d = 0.08$. blue line represents first and orange line represents second Lyapunov exponents respectively. The values of the Lyapunov exponents are given in days^{-1}

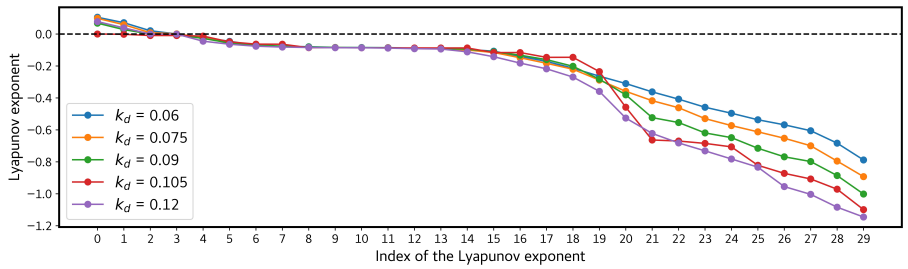


Figure 3.7: Lyapunov spectra of the land atmosphere coupled model for different values of k_d. Each color represents corresponding k_d values used for calculating the spectrum. The values of the Lyapunov exponents are given in days^{-1}.

As thoroughly explained in section 3.4.2, the largest Lyapunov exponent serves as an indicator of the system's highest degree of instability, while the second positive Lyapunov exponent represents the second most unstable characteristic, and so forth. In Fig. 3.8, the results demonstrate that at lower values of k_d, the system exhibits a highly chaotic nature. However, as we increase k_d towards higher values, the system stabilizes, revealing a periodic window. This can also be seen with the Lyapunov spectrum for $k_d = 0.105$ in Fig. 3.7.

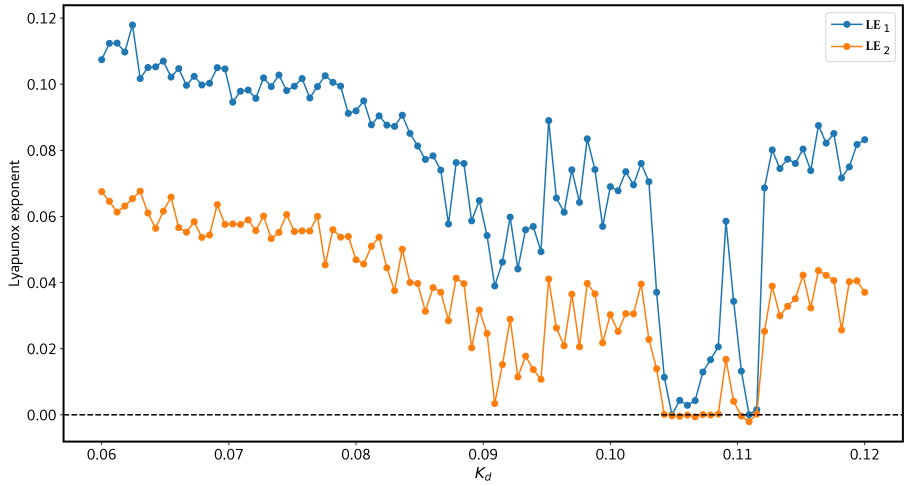


Figure 3.8: First and second Lyapunov exponents of the land-atmosphere coupled model for different non-dimensional values of k_d. Blue line represents the first and orange line represents the second Lyapunov exponents, respectively.$C_g = 300$ Wm^{-2}. The values of the Lyapunov exponents are given in days^{-1}

.

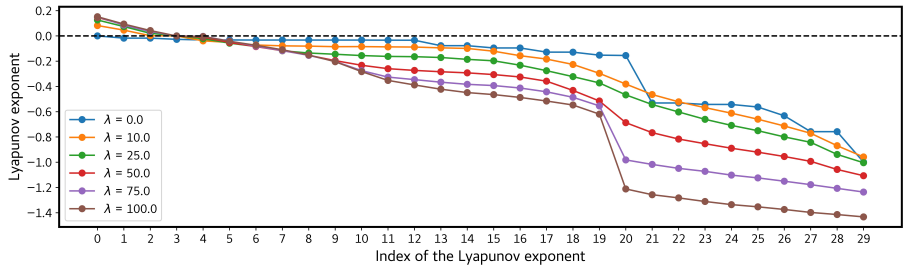


Figure 3.9: Lyapunov spectra of the land atmospheric coupled model for different values of λ. Each colour represents corresponding λ values used for calculating the spectrum. The values of the Lyapunov exponents are given in days^{-1}.

Subsequently, with further increment in k_d, the system returns to a more chaotic behavior, illustrating the complex role of dissipative features.

The primary interaction between land and atmosphere in the model is facilitated through heat exchange denoted by λ. Therefore, it is crucial to understand and analyze how alterations in the heat exchange mechanism influence the behavior of the model. This is illustrated in figure 3.9.

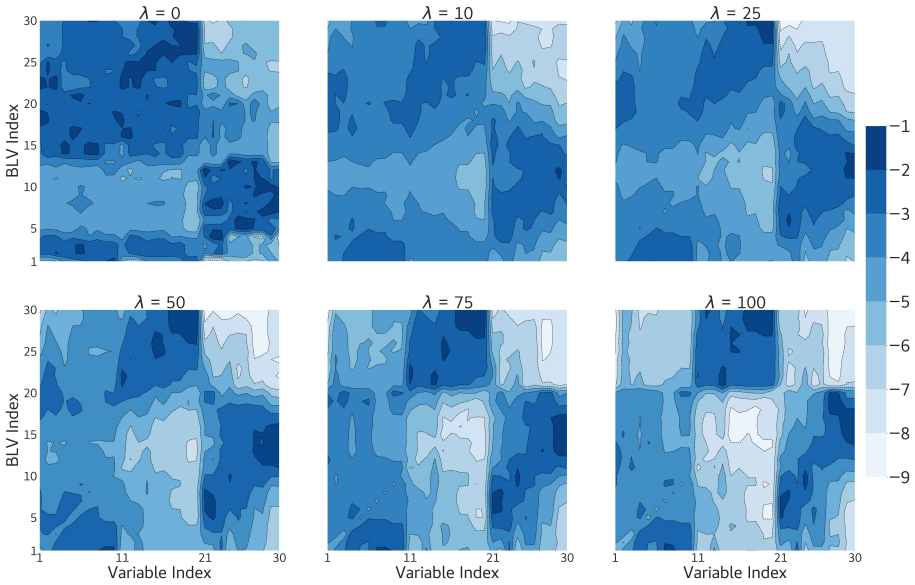


Figure 3.10: Values of the time-averaged and normalized variance of the BLVs as a function of the variables of the model (log_{10} scale) for different λ values in $\mathrm{Wm}^{-2}\mathrm{K}^{-1}$. The 20 first modes corresponds to the variables of the atmosphere and the next 10 ones corresponds to the temperature of the ground. Parameters' value: $C_g = 300$ Wm^{-2} and $k_d = 0.085$. The Euclidean norm is used for all BLVs, and their squared norm is normalized to 1.

When λ is set to zero, the system displays a periodic behavior characterized by one zero and 29 negative Lyapunov exponents. However, for all other non-zero λ values, the system exhibits chaos with 3 positive exponents, 1 zero, and 26 negative Lyapunov exponents. Smaller values of λ (e.g., $\lambda = 10, 25$, and 50) yield a smooth spectrum with a plateau which is similar to the typical Lyapunov spectrum encountered before. Note that with higher λ values, an anomalous bend is observed in the spectrum, specifically from the 20th exponent onward, indicating unrealistic stability. It is also interesting to note that the spectrum associated with the intersection of the land part (between 20th and 21st exponent) is becoming steeper with the increase of λ. The increased heat exchange leads to a reduced temperature difference between the atmosphere and the ground, thereby giving rise to this particular situation. This can be further explained by the averaged variance of Lyapunov exponents for different values of heat exchange λ in Figure 3.10.

A clear separation between land and atmosphere exists at $\lambda = 0$, when there is no exchange of heat between them, resulted in to respective spectrum. For $\lambda = 10$, 25, and 50, the distribution remains similar, with variances concentrated predominantly in the atmospheric component for the first three BLVs and the last ten BLVs. BLVs 3-

20 represent a plateau-like pattern, indicating a coupling between the atmosphere and the ground. Despite variance distribution, it's notable that there is a uniform spread rather than strong concentration or absence of variance. For $\lambda = 75$ and 100, the variance distribution becomes compartmentalized. Variance is now concentrated within the first 20 BLVs for the barotropic streamfunction and ground temperature, while the last 10 BLVs primarily represent atmospheric temperature or baroclinic streamfunction. In contrast to earlier cases, there is a clear absence of variance within the middle portion, specifically confined to BLVs 20-30. This compartmentalized energy distribution leads to a characteristic jump in the corresponding spectrum.

3.5 Predictability properties of zonal, blocking and transition flow regimes

Upon concluding our investigation of the land-atmosphere coupled model's utility in studying low-frequency variability in the atmosphere, we have identified zonal, blocking, and transition regimes concerning different k_d values, as explained in section 3.3. For the range of k_d values between 0.06 and 0.12, the lower values (0.06 to 0.075) encompass all three regimes: zonal, blocking, and transition. As we progress from 0.08 onward, we observe two blocking regimes and a transitional regime between them until $k_d = 0.10$. Subsequently, the system exhibits periodic behavior. At $k_d = 0.115$, two blocking regimes are observed, and further, at $k_d = 0.12$, three flow regimes are identified. These findings demonstrate the model's capability to capture various flow regimes and their transitions based on the selected range of k_d values.

The predictability horizon of the zonal regimes is found to be longer compared to the blocking regimes in the range of k_d values where all three regimes coexist ($k_d = 0.06$ to 0.075). This implies that the blocking regimes exhibit higher instability in agreement with previous findings[Schubert and Lucarini, 2016; Faranda et al., 2016, 2017; Lucarini et al., 2016]. The transition regimes, on the other hand, show notably lower predictability in comparison to the other regimes. Within the interval of k_d values encompassing only two blocking regimes and a transition regime ($k_d = 0.08$ to 0.10), both blocking regimes display significantly different predictability horizons. At the outset ($k_d = 0.08$), they demonstrate a predictability difference of approximately 1 day. Subsequently, this difference increases and reaches about 10 days at $k_d = 0.095$. However, it then decreases again to a difference of 1 day when $k_d = 0.10$. Moreover, it is observed that the stability of the transition regime surpasses that of one of the blocking regimes. This indicates the occurrence of a qualitative change in the predictability of the blocking regimes within this particular range of k_d values.

In these instances, it is noteworthy that situations characterized by lower predictability or significant instability tend to occur when atmospheric blocking takes place on the western side of topographical features. Conversely, when blocking occurs on the eastern side of such topography, it exhibits greater stability and a longer predictability horizon. This observation draws parallels with real-world scenarios, such as the persistence of North

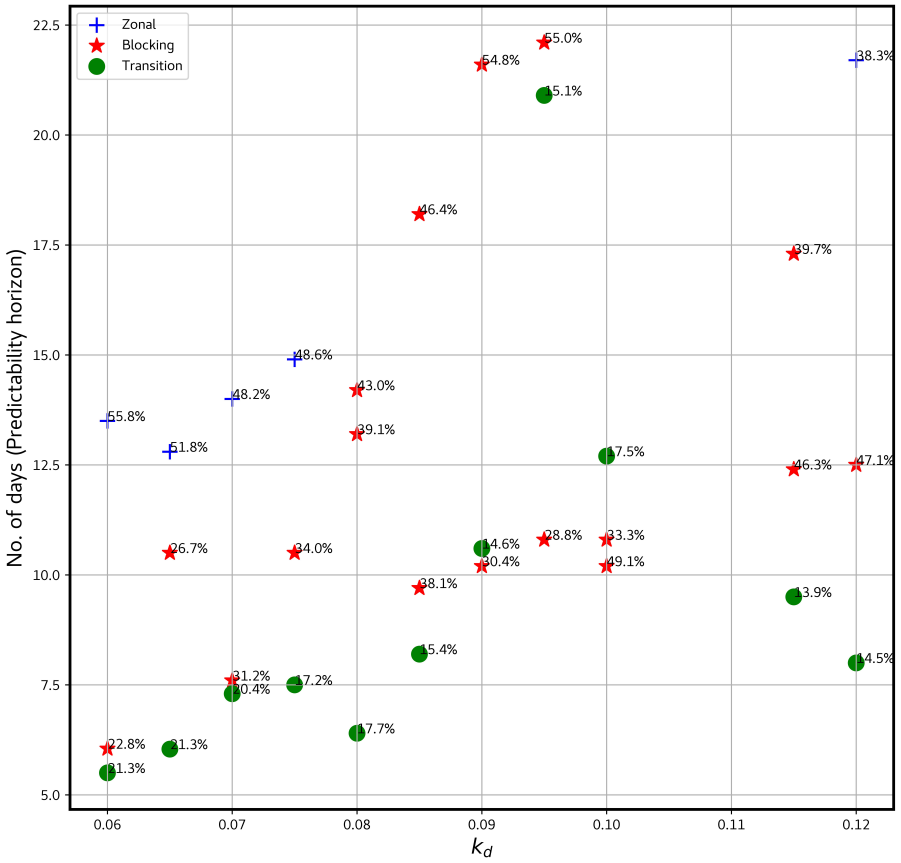


Figure 3.11: Predictability horizon of zonal, blocking and transition flow regimes for different non-dimensional k_d. The numbers represents the percentage of the total number of points included in the respective regime. Predictability horizon is depicted in days

Pacific blocking patterns [Breeden et al., 2020; Kim and Kim, 2019]. The morphology of the identified blocking events bears resemblance to North Pacific blocks, where a high-pressure system is situated either to the west or east of the underlying topography. These locations correspond to the windward and leeward sides of the mountain ranges in the model.

The system is entering a periodic window after $k_d = 0.10$. Then it again become chaotic with 2 blocking regimes and a transition regime and later on with 3 distinct regimes. Figure 3.11 depicts all the findings obtained from this study.

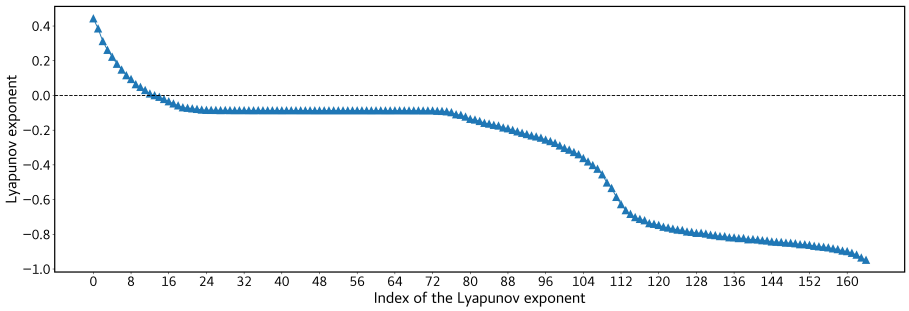


Figure 3.12: Lyapunov spectrum of the land-atmosphere coupled model for $C_g = 300$ Wm^{-2} and $k_d = 0.085$ in (5,5) model configuration. The values of the Lyapunov exponents are given in days^{-1}.

3.6 Impact of model resolution

As per Cehelsky and Tung [1987], resolution of the model can affect the output in various ways. For instance, the nonlinear interaction between the modes (as number of modes increases, resolution of the system increases) is quite altered if different number of modes are considered, resulting in entirely different dynamics for the same set of parameters. Hence, analysis of high resolution runs and its Lyapunov properties is inevitable. In this section, the system is ran with a higher resolution configuration (5,5) with 55 modes being used for both the atmospheric and land part, giving a system with a total of 165 variables. Parameter values are the same as that of the earlier analysis listed in Table 3.1. Figure 3.12 is depicting the Lyapunov spectrum and Figure 3.13 is representing the time-averaged variance of the BLVs of the high resolution run.

The Lyapunov spectrum exhibits structural similarity when compared to the low-resolution spectra, except that more positive exponents are present. Specifically, it comprises 12 positive, one zero, and 152 negative exponents. Notably, there is a distinctive plateau observable within the range of 20 to 75, which is a characteristic feature attributed to the interaction between the land and the atmosphere in the model. This plateau phenomenon arises due to the disparity in timescales resulting from the intricate interplay between land and atmosphere dynamics.

In Fig. 3.13, higher variances in the atmosphere are observed on first 40 BLVs and also at the BLVs greater than 70 indicating that the most chaotic and stable dynamics are resulting from the atmospheric component. Furthermore, it is noteworthy that a greater concentration of variance is observed to be shifted towards the variables that specifically represent the ground temperature, particularly within the range of BLVs 20 to 75. This shift is a key factor contributing to the formation of a plateau within the spectrum in question. It becomes evident that there is a distinct compartmentalization between each set of variables, including the barotropic, baroclinic, and ground temperature variables, which is more pronounced when compared to the variance illustration at lower resolutions.

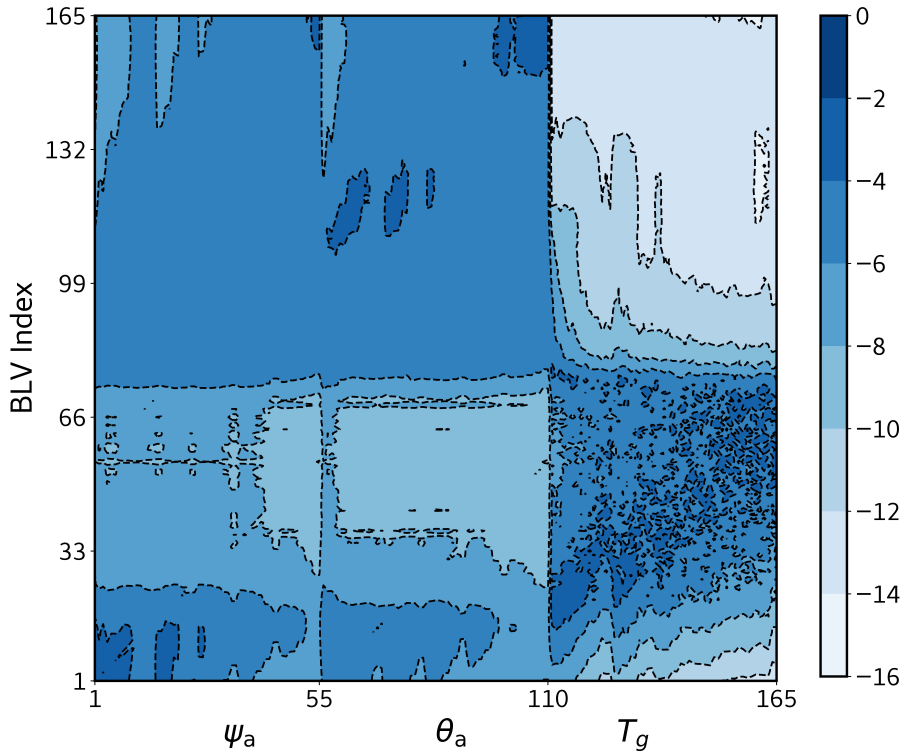


Figure 3.13: Values of the time-averaged and normalized variance of the BLVs as a function of the variables of the model (log_{10} scale) in (5,5) model configuration. The 110 first modes corresponds to the variables of the atmosphere and the next 55 ones corresponds to the temperature of the ground. Parameters' value: $C_g = 300$ Wm^{-2} and $k_d = 0.085$. The Euclidean norm is used for all BLVs, and their squared norm is normalized to 1.

The outcome of the clustering analysis has delineated two clearly defined patterns: one marked by zonal flow and the other by instances of blocking. The intermediate pattern that once existed between these two regimes is now absent. Notably, both the zonal and blocking events exhibit an identical predictability horizon, specifically spanning a period of two days. This feature is contrasting with what is found at the lower resolution and also in the current literature on this topic. This aspect is worth investigating further in the future by exploring other sets of parameters and other resolutions.

3.7 Discussions

This study focused on characterizing the variability and instability properties of different flow regimes and their dependence on important parameters in an idealized coupled model, namely the quasi-geostrophic land atmosphere coupled model. The investigation also aimed at exploring the predictability of zonal, blocking, and transition flow regimes using Lyapunov exponents.

The analysis revealed that the model is less sensitive to variations in meridional differences in solar heating absorbed by the land, represented by C_g. Based on observations, a fixed value of 300 Wm^{-2} for C_g was chosen for further analysis. The study found that the model's stability is significantly affected by surface friction k_d. Different values of k_d were explored, and it was observed that at lower k_d values, the system exhibits chaotic behavior, while at higher k_d values, periodic windows alternate with chaotic behaviors. Within this range, the systems solutions meander between various flow regimes, including zonal, blocking, and transition.

The heat exchange mechanism, represented by λ, was also analyzed, and it was found that when λ is set to zero, the system displays periodic behavior, while for non-zero λ values, the system exhibits considerable chaos. Overall, the model demonstrated the capability to capture various flow regimes and their transitions based on the selected range of k_d values, providing insights into the potential behavior of the atmosphere.

The predictability properties of three distinct flow regimes were investigated: zonal, blocking, and transition, which were the fundamental components of low-frequency variability (LFV) in the model. The predictability horizon of the zonal regimes was found to be longer compared to the blocking regimes which is consistent with earlier results [Schubert and Lucarini, 2016; Faranda et al., 2016, 2017; Lucarini et al., 2016], when all three regimes coexist. The transition regimes showed notably lower predictability compared to the other regimes. Within a specific range of k_d values, the blocking regimes displayed different predictability horizons, indicating the occurrence of a qualitative change in the predictability of the blocking regimes.

Weather patterns that involve atmospheric blocking to the west of a given topographical feature tend to have reduced predictability and show instability when contrasted with blocking occurrences situated to the east of such topographical elements. This finding aligns with actual meteorological occurrences, such as the persistence of North Pacific blocking patterns [Breeden et al., 2020; Kim and Kim, 2019]. The shape and characteristics of the identified blocking events closely resemble North Pacific blocks, where a high-pressure system exists either on the western or eastern side of the underlying topography. In the physical world, these positions correspond to the windward and leeward sides of mountain ranges composed of rocky terrain. Despite qgs models being regarded as less comprehensive, their utilization in this study allows for a more relevant impact, akin to real-world situations as described above.

Upon increasing the model resolution, Lyapunov properties exhibited a remarkable resemblance to those observed at lower resolutions. However, the distribution of points on the attractor gave rise to two distinct clusters, delineating the blocking and zonal regimes, thereby extinguishing the potential for the transition regime. Notably, both the blocking and zonal regimes displayed a predictability horizon limited to 2 days.

In the backdrop of rising global temperatures and the escalation of climate extremes, comprehending the intricate dynamics governing atmospheric blocking occurrences and their predictability becomes paramount, given that blocking events are consistently linked to extreme weather phenomena. The impact of climate change can also be explored in the current study by modifying the emissivity of the atmosphere. This will be explored in the future.

The knowledge acquired through this study holds potential significance for climate and weather prediction models, contributing to the advancement of our understanding of the crucial atmospheric dynamics shaping the Earth's climate system. In future investigations, we will assess the influence of the same parameters within more complex models, enabling us to conduct comparisons that will aid in identifying alterations in land-atmosphere interactions as atmospheric complexity intensifies. This undertaking will further our comprehension of how the interaction between land and the atmosphere evolves with increasing intricacies in atmospheric systems and how it affect the predictability of the weather regimes.

Chapter 4

Predictability of north Pacific blocking events : Analogue based analysis of historical MIROC6 simulations

---

This chapter is based on the following paper, under review in QJRMS:

Xavier, A. K., Hamilton, O., Faranda, D., and Vannitsem, S.: Predictability of North Pacific blocking events: Analogue based analysis of historical MIROC6 simulations, *Q. J. R. Meteorol. Soc.*, submitted, https://doi.org/10.48550/arXiv.2504.17691, 2025.

Abstract

Atmospheric blocking exerts a profound influence on mid-latitude circulation, yet its predictability remains elusive due to intrinsic non-linearities and sensitivity to initial-conditions. While blocking dynamics have been extensively studied, the impact of geographical positioning on predictability remains largely unexplored. This study provides a comparative assessment

of the predictability of Western and Eastern North Pacific blocking events, leveraging analogue-based diagnostics applied to CMIP6 MIROC6 simulations. Blocking structures are identified using geopotential height gradient reversal, with their temporal evolution analysed through trajectory tracking and error growth metrics. Results reveal that Eastern blocks exhibit lower predictability, characterized by rapid error divergence and heightened mean logarithmic growth rates, whereas Western blocks display dynamical stability. Persistence analysis gives no significant difference between eastern and western North Pacific blocking events. Sensitivity analyses across varying detection thresholds validate the robustness of these findings.

4.1 Introduction

Atmospheric blocking is a fundamental dynamical phenomenon that influences mid-latitude weather evolution by disrupting the typical westerly flow. Characterized by persistent, quasi-stationary high-pressure systems, these blocks can last from several days to weeks, leading to prolonged extreme weather conditions such as heatwaves, cold spells, and heavy precipitation events Rex [1950]; Tibaldi and Molteni [1990]; Masato et al. [2012]; Liu [1994b]; Nakamura and Huang [2018]. The North Pacific region is particularly prone to blocking events that play a key role in modulating weather and climate variability across North America and Eurasia Park et al. [2024]; Woollings et al. [2018].

Despite its recognized impact on regional climate and extreme weather, the predictability of atmospheric blocking remains a challenge in numerical weather prediction (NWP) and climate modeling. The inherent nonlinear nature of blocking dynamics, along with their sensitivity to initial conditions and complex interactions with large-scale atmospheric waves, contributes to forecast uncertainty Masato et al. [2012]; Matsueda and Palmer [2018]; Pelly and Hoskins [2003]. In the North Pacific, blocking events are typically categorized into two primary regions: Western North Pacific (WNP) and Eastern North Pacific (ENP) blocks Davini et al. [2012]. Given the substantial downstream effects on weather and climate variability, enhancing the understanding of the predictability of these blocking regimes is crucial for improving forecast skill and weather model performance Drouard et al. [2019]; Merryfield et al. [2020a]; Breeden et al. [2020].

Several studies have examined the predictability of North Pacific blocking using ensemble forecasting methods and model intercomparisons Matsueda [2009]; Schiemann et al. [2020a]; Leutbecher and Palmer [2008]. While advancements in global climate models (GCMs) and numerical weather prediction systems have led to some improvements in simulating blocking characteristics, significant biases persist in representing their frequency, persistence De Luca et al. [2024]; Schiemann et al. [2020a], and decay Palmer et al. [2008]; Davini and D'Andrea [2016]. The latest generation of Coupled Model Intercomparison Project Phase 6 (CMIP6) models still struggle to capture high-impact extreme events linked to blocking, highlighting a critical gap in understanding the mechanisms governing their predictability Davini and d'Andrea [2020].

An overlooked aspect in existing research is the potential influence of the geographical position of a blocking event on its predictability. To date, no systematic studies have been conducted to determine whether the location of blocking relative to major topographical features affects its predictability. Research by Xavier et al. [2024], based on a reduced-order atmosphere-land model Demaeyer et al. [2020], suggest that blocking events positioned to the west of a given topographical feature tend to exhibit lower predictability and greater instability compared to those occurring on the eastern side.

Building on the results of this idealized approach that suggest boundary constraints can modulate regime stability Xavier et al. [2024]), we ask whether the same predictability differences are evident in a comprehensive model. Using CMIP6 MIROC6 daily fields, we analyse North Pacific blocking events with an emphasis on how location relative to basin boundaries (continental margins) influences intrinsic predictability and stability. The spatial structures and geographical distributions reported by Xavier et al. [2024] closely resemble North Pacific blocks, which in practice occur either on the western or eastern side of major basin boundaries; in the physical world these correspond to the Asian (Russian) and North American (Alaska - west coast) margins of the Pacific. Accordingly, we define two objective boxes that hug these boundaries: an Eastern North Pacific box adjacent to Asia and a Western North Pacific box adjacent to North America (Fig. 1). Our hypothesis is that these blocks exhibit difference in predictability, owing to its geographical position and proximity to the continents which can be attributed to the differences in background flow and transient eddy activity.

The structure of the paper is as follows. Section 4.2 introduces the data and methodology used for the investigation. In Section 4.3, properties of the reference-analogue pair is discussed along with the predictability properties of identified blocking events. The conclusions drawn from the research are provided in Section 4.4, along with future perspectives for further studies.

4.2 Data and Methodology

In this section we outline the dataset and methodological framework that was used to analyze the predictability of atmospheric blocking in the North Pacific.

4.2.1 Data

This study uses the output of the Coupled Model Intercomparison Project Phase 6 - Model for Interdisciplinary Research on Climate, version 6 (CMIP6 MIROC6) experiment [Tatebe and Watanabe, 2018], in which the atmospheric component has a spatial resolution of approximately $1.4^\circ \times 1.4^\circ$ (T85 spectral resolution, 250 km), covering the period between 1850–2014, using the historical scenario. While reanalysis datasets such as ERA5 and 20th Century Reanalysis have been widely used to study blocking dynamics, we chose not to rely on them here because this type of analysis has already been extensively addressed in the literature. Moreover, MIROC6 provides a substantially longer historical record (1850–2014) than reanalyses, enabling a larger sample size of blocking events for robust

statistical evaluation. Importantly, MIROC6 has been shown to exhibit comparatively low bias over the North Pacific relative to both ERA5, 20th Century reanalysis and MIROC5 [Lohmann et al., 2024; Tatebe et al., 2019a], making it a suitable dataset for our analogue-based predictability analysis. The analysis is based on $500\mathrm{hPa}$ (Z_{500}) with a temporal resolution of one day. Although MIROC6 provides multiple ensemble members, only one member(r10i1p1f1) was used here, as the analogue - reference framework (detailed in 4.2.2) already samples diverse initial conditions in a way analogous to an ensemble. For model dependence sensitivity, we repeated the analysis with IPSL-CM6A-LR and MPI-ESM1 historical simulations (daily Z_{500}), processed identically to MIROC6 and results are shown in the supplementary information (Figs. S1 and S2)

4.2.2 Methodology

The initial step is to identify blocking events in the North Pacific region and classify these into eastern or western blocks based on the geographical location. The east and west domains were defined as boxes which is shown in Figure 4.1. Color gradient denotes the blocking frequency calculated using Davini et al. [2012] (detailed in section 4.2.2.1) index. Blocking frequency is spread out in the Eastern region where as it is less and concentrated in the western coast of North America.

4.2.2.1 Identifying Blocking Events

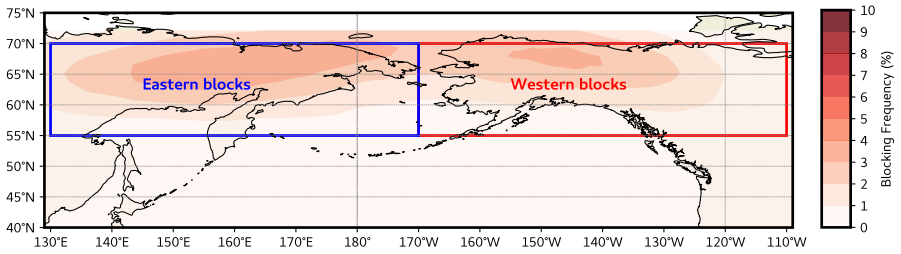


Figure 4.1: Geographical domains used to define the Eastern and Western North Pacific blocking regions in this study. Both domains span latitudes of $55°$N–$70°$N. The Western North Pacific (WNP) region (red) is bounded between longitudes of $10°$W to $130°$W ($190°$E - $250°$E), and the Eastern North Pacific (ENP) region (blue) between $70°$E to $10°$W ($130°$E–$190°$E). These regions are highlighted by boxes to facilitate the identification of atmospheric blocking events. Color gradient represents the blocking frequency over the study region

To identify atmospheric blocking events, we employ the meridional gradient reversal method using the $500\mathrm{hPa}$ (Z_{500}) (Z_{500}), following the approach introduced in Davini et al. [2012]. This method identifies reversals in the (Z_{500}) gradient between a northern latitude (denoted GHGN) and a southern latitude (GHGS), and is presented in Equation 4.1.

$$\begin{aligned} \text{GHGN}(t, \lambda_0, \Phi_0) &= \frac{Z_{500}(t, \lambda_0, \Phi_N) - Z_{500}(t, \lambda_0, \Phi_0)}{\Phi_N - \Phi_0} \\ \text{GHGS}(t, \lambda_0, \Phi_0) &= \frac{Z_{500}(t, \lambda_0, \Phi_0) - Z_{500}(t, \lambda_0, \Phi_S)}{\Phi_0 - \Phi_S} \end{aligned} \tag{4.1}$$

where λ_0 and Φ_0 represent the longitude and latitude of the grid cell, respectively, and t is the given time index. In this study we calculate blocking events at midday UTC on a daily basis, so the variable t is an integer daily index. Φ_0 ranges from 30° to 75°N. $\Phi_S = \Phi_0$ - 15°, $\Phi_N = \Phi_0 + 15°$ and $Z_{500}(t, \lambda_0, \Phi)$ denotes the (Z_{500}) at the specified latitude, on day t.

A grid cell is considered to be experiencing instantaneous blocking (IB) if both of the following conditions hold:

$$\text{GHGS}(t, \lambda_0, \Phi_0) > 0 \quad \text{GHGN}(t, \lambda_0, \Phi_0) < -10\text{m}(^\circ\text{lat})^{-1}$$

Davini et al. [2012] introduced additional conditions to isolate blocking events that occur over large spatial scales, and have temporal persistence. This criterion ensures that only regions that exhibit a strong reversal in the meridional (Z_{500}) gradient are considered blocking events, filtering out transient anomalies. To do this large scale blocks are identified by requiring that the IB condition is satisfied over a longitudinal span of at least 15°.

To include temporal persistence, a (BE) (Blocking Events) is detected if a cell that satisfies the large scale blocking condition occurs within a 5° latitude $\times$ 10° longitude box centred on that grid cell, for at least five consecutive days.

Secondly, to avoid low latitude blocks in order to focus on mid latitude blocks and to avoid detecting block like features from tropics, this criteria is included

$$\text{GHGS}_2(\lambda_0, \Phi_0) = \frac{Z_{500}(\lambda_0, \Phi_S) - Z_{500}(\lambda_0, \Phi_S - 15^\circ)}{15^\circ} \tag{4.2}$$

$$< -5 \text{ m}(^\circ\text{lat})^{-1}. \tag{4.3}$$

Hence a Blocking Event, $BE(t, x, y)$, is defined as follows

$$BE(t, x, y) = \begin{cases} 1 & \text{if meets criteria from Davini et al. [2012]} \\ 0 & \text{otherwise} \end{cases}$$

here t is the time index and x and y is the longitude and latitude of the grid cell.

Once the BE, are identified, the time-averaged blocking frequency at each grid cell over the entire analysis period is computed. This metric, denoted as $AB(x, y)$, represents the proportion of time steps that a given grid cell is classified as blocked:

$$AB(x,y) = \frac{\sum_{t\in T} BE(t,x,y)}{\#T},$$

where T is an index of all time steps, and $\#T$ represents the number of time steps considered.

To quantify the regional mean blocking frequency $BE_{\%}$, we compute the spatial average of $AB(x,y)$ over the entire study domain, which is given by:

$$BE_{\%} = \frac{\sum_{x,y} AB(x,y)}{\#x \cdot \#y}.$$

Here, $\#x$ and $\#y$ denote the total number of grid cells in the longitudinal and latitudinal directions, respectively. This metric provides an estimate of the overall blocking occurrence in the domain.

To retain only significant blocking occurrences, we apply a filtering step: grid cells are classified as part of a blocking region if their local blocking frequency exceeds a fraction α of the regional mean, i.e.,

$$F(x,y) = \begin{cases} 1, & \text{if } AB(x,y) > \alpha \cdot BE_{\%}, \\ 0, & \text{otherwise.} \end{cases}$$

The filtering coefficient α is a dimensionless sensitivity parameter that allows for the comparison of blocking characteristics across different study areas. It ensures that the detection methodology is not biased by the size of the analysis domain. By applying this filtering criterion, we effectively select blocks that occur over the defined geographical area and have a spatial spread above a given threshold.

A given day t is considered a blocked day if the number of grid cells meeting the blocking condition exceeds a prescribed threshold for the selected α:

$$\sum_{x,y} F(x,y) > N_{\alpha},$$

where N_{α} represents the threshold number of grid cells that must satisfy the blocking condition for the day to be classified as blocked. For further clarification of the definition, please refer to table 4.1. The use of an α-threshold is necessary because blocking systems are not uniformly distributed across the predefined ENP and WNP boxes (Fig. 4.1), but rather occupy portions of them. Distribution of blocking frequency (color gradient projected on fig 4.1)is denoting that the blocks identified is not concentrated rather spread all over the North Pacific region with a peaks over the ENP and WNP boxes The standard Davini index flags grid cells that satisfy the gradient-reversal condition, yet without an additional threshold, small or fragmented detections could be classified as regional blocks.

By requiring that at least a fraction α of the domain be blocked, we ensure that only events with a meaningful spatial footprint inside the region are retained. This criterion also normalizes differences between the ENP and WNP domains, making their comparison robust.

Sensitivity tests with α varying between 0 and 1 showed that the number of blocked days changes markedly with threshold choice. For instance, with $\alpha = 0.20$, we identify 532 ENP and 251 WNP blocked days, while with $\alpha = 0.25$, the sample reduces to 337 and 103 days, respectively. Higher thresholds (e.g., $\alpha = 0.30$) lead to an overly restrictive sample (105 ENP, 54 WNP). We therefore selected $\alpha = 0.20$ and $\alpha = 0.25$ as optimal values: they yield event counts consistent with reanalysis-based climatologies [Carrera et al., 2004; Barriopedro et al., 2006; Lupo et al., 2019; Hwang et al., 2020], while preserving the synoptic-scale coherence of the blocking structures. Conducting the analysis with both thresholds further allowed us to test the robustness of our conclusions.

Table 4.1: Summary of notations used for blocking detection and frequency measures.

Symbol	Definition
$IB(t, x, y)$	Instantaneous Blocking indicator (1 if gradient reversal condition is satisfied, 0 otherwise)
$BE(t, x, y)$	Blocking Event indicator (1 if IB satisfies large scale and persistence criteria, 0 otherwise)
$AB(x, y)$	Local blocking frequency: fraction of time steps when a grid cell is classified as blocked
$BE\%$	Regional mean blocking frequency: spatial average of $AB(x, y)$ over the study domain

4.2.2.2 Tracking Blocking Events

In the previous section we described how we identify Blocking Events $BE(t, x, y)$, however blocking events are defined on a particular day t and provide no information about how they evolve to the next day $t + 1$. To allow us to track the same blocking event through time we use the tracking methodology introduced in Schwierz et al. [2004b].

For each day in the study period the grid cells that experience a blocking event ($BE(t, x, y) = 1$) are grouped into connected clusters of grid cells. Two blocking events ($BE(t_0, x_1, y_1) = 1$ and $BE(t_0, x_2, y_2) = 1$) are defined as connected if a path exists between the two events which passes through grid cells (x_i, y_i), where for all transiting grid cells $BE(t_0, x_i, y_i) = 1$, and each grid cell shares an edge. In other words, two blocking events are in the same blocking cluster if they are connected to one another with other non-zero blocking events. These clusters were identified using the python library SciPy [Virtanen et al., 2020], which identifies connected regions in pixilated images [Steinfeld, 2020].

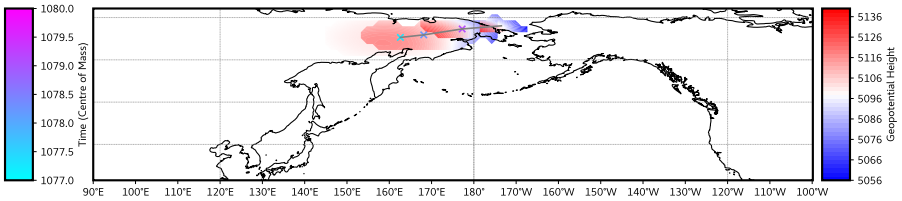


Figure 4.2: Schematic representation of tracking a blocking cluster identified on 1851-01-24 (index 1077). '$\times$' symbols indicate the centre of mass (CoM) of the cluster on each day, coloured by time progression (index) as shown by the left vertical colorbar. The background colour gradient represents (Z_{500}), with values indicated by the right vertical colorbar.

A blocking cluster at day $t+1$ is considered as the evolution of the cluster at day t if they overlap sufficiently in space. This overlap is calculated by taking the spatial intersection of the clusters from one day to the next. The threshold is calculated by comparing the number of grid cells in the intersection with the number of grid cells in the cluster on the first day t. If the intersection covers at least half of the original cluster, we consider the cluster at $t+1$ to be the evolution of the cluster from time t. More concretely, let $C_i(t)$ be a cluster of blocking events at time t, and $C_j(t+1)$ another cluster on the next day. If $|C_i(t) \cap C_j(t+1)|/|C_i(t)| > 0.5$ then we assume $C_i(t)$ evolves into $C_j(t+1)$. Here, we use $|\cdot|$ to denote the number of grid cells in each cluster. In this study we only track blocking clusters which have a single predecessor and a single successor cluster, thus removing any blocking clusters which split or merge from other blocks. An example of the process of tracking a particular blocking cluster is shown in Figure 4.2.

Lastly, we calculate the centre of mass of each cluster, which provides a representative location for each block, enabling the identification of displacement and persistence while minimizing the influence of irregular block shapes and fragmented patterns. The centre of mass is weighted using the (Z_{500}). We apply this weighting as the centre of the blocking cluster as in this study we are using the (Z_{500}) as the measure for identifying blocking events.

4.2.2.3 Finding Analogues

Once blocked days are identified, we determine one analogue for each blocked day based on a similarity criterion. The analogue search is performed using a distance metric to compare atmospheric states.

The fundamental concept of assessing atmospheric predictability through analogue-based error diagnostics has been widely discussed in the meteorological literature [Lorenz, 1969]. We build upon these foundational ideas to evaluate and compare the predictability of ENP and WNP blocking events. A key metric in those early analyses was the reference–

analogue error, often quantified with a (possibly weighted) root-mean-square height difference to measure deviations between two atmospheric states. Reference–analogue errors arise from inherent dynamical differences between effectively occurring atmospheric situations, in particular for blocking events that share similar large-scale structures but evolve differently in time [Yiou et al., 2007; Faranda et al., 2017, 2023]. The progression of analogue errors has been used as a diagnostic of blocking stability, helping to distinguish persistent from transient regimes [Plaut and Vautard, 1994], and, more broadly, as a data-driven alternative to ensemble approaches for studying flow recurrence [Yiou, 2014].

Following Lorenz [1969], an analogue is assumed to reproduce the spatial distribution of the reference state plus a small deviation. By selecting, for each blocked day, the analogue that minimizes the distance to its reference, the initial deviation is reduced, and comparing their subsequent evolutions provides a local (in phase space) estimate of predictability for that reference block.

For the reference block, on day t_r, its corresponding analogue day t_a is selected from the dataset based on a minimum distance criterion. The similarity between two atmospheric states is assessed using the spatial distribution of (Z_{500}). Here, X_t denotes the atmospheric state vector at time t, represented by the gridded (Z_{500}) over the selected spatial domain. It characterizes the synoptic-scale circulation pattern for a given day. The Euclidean distance is used to quantify the difference between the reference blocked day's (Z_{500}) field and that of any candidate day as follows:

$$d(X_{t_r}, X_t) = \|Z_{500}(t_r) - Z_{500}(t)\|\,, \tag{4.4}$$

where $d(X_{t_r}, X_t)$ represents the Euclidean distance between the (Z_{500}) fields at time t_r and t. The dataset consists of spatial distribution of (Z_{500}), and the goal is to identify analogue block on day,t_a such that:

$$t_a = \underset{|t-t_r|\geq\Delta t_{\min}}{\operatorname{argmin}} d(X_{t_r}, X_t), \tag{4.5}$$

where $\Delta t_{\min} = 5$, as in Davini et al. [2012], which ensures a minimum temporal separation of at least 5 days between the blocked day and its analogue [Diao et al., 2006]. This constraint prevents the selection of analogues that are too close in time with the original reference block, thereby avoiding redundancy due to short-term atmospheric persistence.

The analogue search procedure involves iterating over all available time steps, computing the Euclidean distance between the (Z_{500}) distributions, and selecting the time step t_a that satisfies both the minimum distance criterion and the temporal separation condition. This approach ensures that each blocked day is assigned an analogue day that exhibits the most similar large-scale (Z_{500}) distribution, providing insights into the recurrence of similar atmospheric circulation patterns.

The traditional analogue method for assessing error evolution Lorenz [1969] is not suitable in this context, as it fails to account for differences in predictability between eastern and western blocking regions due to the displacement of blocking events following their initial identification. Therefore, error evolution based on the center of mass is employed in the current study to better capture the spatial progression of blocking features.

After identifying the reference and analogue blocking pairs, we track their temporal evolution using the block tracking algorithm, as explained in Section **??**. The trajectories of the reference and analogue blocks are denoted by $\mathbf{X}_r(t)$ and $\mathbf{X}_a(t)$, respectively, representing the latitude and longitude coordinates of the blocking center over time. Unlike traditional analogue approaches that select several analogues per reference state (often with relatively large initial errors), we select only the single closest analogue for each blocked day. This reduces the initial mismatch and ensures that subsequent divergence reflects the intrinsic instability of the block rather than poor analogue choice. By applying this systematically to all identified blocked days, the methodology mimics an ensemble evaluation across hundreds of cases, providing a probabilistic measure of predictability for ENP and WNP blocks.

4.2.2.4 Measure of Predictability

To assess the predictability of ENP and WNP blocking events, we analyse the error evolution between the trajectories of the reference and analogue blocking pairs. The tracking of these blocking days is performed using a block tracking algorithm (Section **??**) that follows the movement of the centre of mass of each identified blocking system over time.

The error evolution between the reference and analogue blocking trajectories is computed using the Haversine distance, which measures the great-circle distance between two points on the Earth's surface:

$$d_H(\lambda_r, \phi_r, \lambda_a, \phi_a) = 2R \arcsin\left(\sqrt{\sin^2\left(\frac{\phi_a - \phi_r}{2}\right) + \cos(\phi_r)\cos(\phi_a)\sin^2\left(\frac{\lambda_a - \lambda_r}{2}\right)}\right), \tag{4.6}$$

where d_H is the Haversine distance, $R = 6371$ km is the Earth's radius, and (λ, ϕ) represent the longitude and latitude of the reference (λ_r, ϕ_r) and analogue (λ_a, ϕ_a) blocking centres.

For each pair of reference and analogue trajectories, we compute the error evolution at time t as:

$$E_i(t) = d_H\left(\mathbf{X}_{r,i}(t), \mathbf{X}_{a,i}(t)\right), \tag{4.7}$$

where $E_i(t)$ represents the displacement error for the i-th reference–analogue pair at time step t. The errors are recorded for all analogue pairs and stored in an error matrix, allowing for further statistical analysis.

For each region and threshold α, we rank all reference–analogue pairs by their initial Euclidean distance at t_0 and analyses the first 50 as the baseline set and the first 75 as a sensitivity set, a choice that controls the initial error so subsequent divergence reflects dynamics rather than analogue mismatch and that preserves equal sample sizes across ENP/WNP for robust bootstrap inference; we avoid a fixed-percentage selection because the total number of identified blocks varies markedly across regions and α, which would otherwise yield unequal sample sizes and heterogeneous uncertainty.This enhances the robustness of the error growth analysis by minimizing the influence of initial condition differences and allowing for a meaningful assessment of dynamical divergence over time.

The statistical distribution of errors is analyses by computing the mean and standard deviation of the error evolution across all reference-analogue pairs. To estimate the uncertainty in the error evolution, a bootstrap resampling technique is applied, and the 95% confidence interval (CI) is obtained.

To assess the exponential growth of initial uncertainties, we compute the logarithmic growth rate for each pair at lead time τ and increment $\Delta\tau$, which quantifies the sensitivity of blocking events to small initial perturbations:

$$\lambda_i(\tau) = \frac{1}{\Delta\tau} \ln\left(\frac{E_i(\tau + \Delta\tau)}{E_i(\tau)}\right), \tag{4.8}$$

where $E_i(\tau)$ is the displacement error for the i-th pair at lead time τ, and $\Delta\tau$ is the time increment.

The mean logarithmic growth rate at each lead time is then computed by averaging over all analogue pairs:

$$\bar{\lambda}(\tau) = \frac{1}{N} \sum_{i=1}^{N} \lambda_i(\tau), \tag{4.9}$$

where N is the total number of analogue realizations. Comparing $\bar{\lambda}$ for ENP and WNP North Pacific blocks reveals differences in their intrinsic predictability characteristics.

4.2.2.5 Persistence of Blocking Events

To quantify persistence, we define the lifetime of a blocking event based on its tracked trajectory over time. Given a blocking system that is identified at time t_0 and remains detectable until time t_f, its persistence P is given by $P = t_f - t_0 + 1$, where t_0 is the initial and t_f is the final time step where the block is detected.

This methodology enables the analysis of the persistence of blocking events, providing ideas into their stability and potential for long-term atmospheric impacts. Overall, the analysis above provides both a deterministic and probabilistic measure of stability through the persistence and mean logarithmic growth rate computation allowing for a comprehensive assessment of the stability and comparability of north Pacific blocking events. To ensure statistical robustness of the analogue-based predictability diagnostics, we analyse all months (annual sampling). Given the strict spatial and persistence criteria in the blocking definition, seasonal stratification (e.g., DJF vs. JJA) would substantially reduce the number of ENP or WNP blocking events and inflate sampling uncertainty of growth-rate estimates and their confidence intervals.

4.3 Results and Discussion

4.3.1 Composite of geopotential height, (Z_{500}) on ENP and WNP North Pacific Blocking Days

The figure 4.3 shows the composite (temporal mean) 500 hPa (Z_{500}) field on days classified as blocked, computed using the methodology detailed in Section 4.2 when $\alpha = 0.25$. The classification effectively distinguishes the ENP and WNP blocking patterns. The spatial distribution of Z_{500} reveals that ENP blocks are primarily concentrated over the Aleutian region of Russia. This indicates that the most identified ENP blocks exhibit blocking highs in this region. Conversely, WNP blocks exhibit a more extensive distribution, with blocking highs dispersed across Alaska. The WNP blocks are characterized by an intense high-pressure system, as evident from the deeper red-shaded regions, compared to the ENP blocks. While the ENP block presents a confined structure, the WNP block's influence extends over a broader region of the North America. This spatial distinction suggests potential differences in the dynamical characteristics and downstream impacts of these blocking patterns.

Results for $\alpha = 0.20$ (Appendix B.1, Fig A1) show similar spatial patterns but with a larger number of identified blocking days, consistent with the more lenient threshold. These are included as sensitivity tests to demonstrate robustness.

4.3.2 Persistence of ENP and WNP blocks

In this section, persistence of the ENP and WNP blocks were calculated for $\alpha = 0.20$ and $\alpha = 0.25$.

Figure 4.4 presents the probability density distribution of blocking persistence, with a fitted gamma distribution applied to the entire dataset. The initial portion of the distribution exhibits a strong overlap between ENP and WNP blocks, particularly for block lifetimes up to 10 days. Beyond this threshold, the tails of the distributions diverge significantly, indicating a higher occurrence of long-lived ENP blocks compared to WNP blocks. ENP blocks demonstrate a tendency to persist beyond 10 days, whereas WNP blocks exhibit a sharper decline in frequency for extended durations.

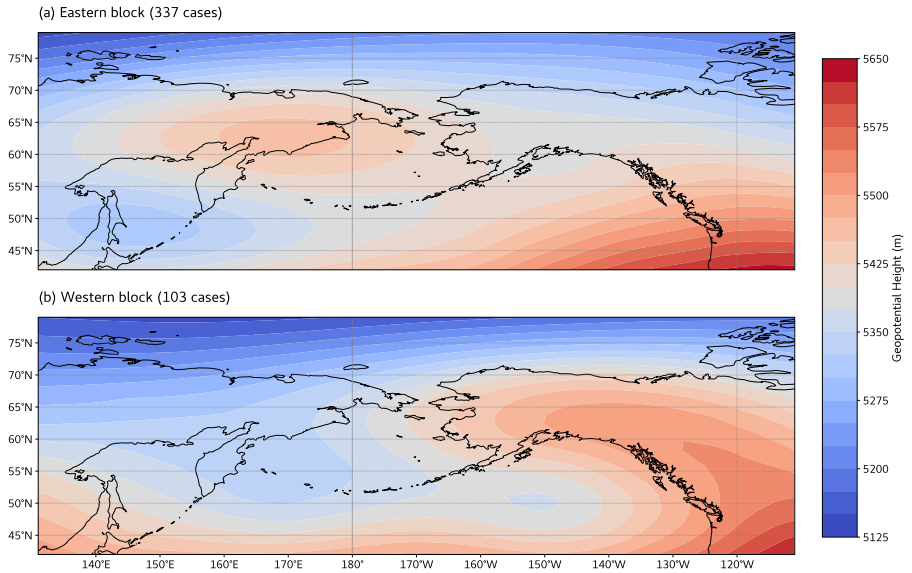


Figure 4.3: Composite (temporal mean) of (Z_{500}) (m) conditioned on blocked days for **(a)** ENP blocks and **(b)** WNP blocks, obtained using the methodology described in section **??** with $\alpha = 0.25$. The composite is computed over the base period from 1850 to 2014. 337 ENP blocks and 103 WNP blocks is identified with this threshold

When the sample size is increased by reducing the selection threshold to $\alpha = 0.20$ (Figure A2), the initial portion of the distribution remains substantially unchanged. However, the disparity in long-lived blocking events diminishes, with ENP and WNP blocks displaying a more balanced distribution of extended persistence.

The observed changes with decreasing α can be attributed to the inclusion of a broader range of blocking events, incorporating shorter-lived and less persistent blocks that were previously excluded under a stricter selection criterion. Given the constraints of our methodology, we did not identify notable differences in the persistence between ENP and WNP blocking events.

4.3.3 Structural Comparison of Reference and Analogue Blocks

This section presents a representative case illustrating the (Z_{500}) fields for a typical ENP and WNP block and their nearest - neighbor analogues. In Figure 4.5 spatial distribution of (Z_{500}) of a selected ENP and WNP block and its corresponding analogues were depicted. In order to identify the difference in the distribution, anomaly between them is also computed.

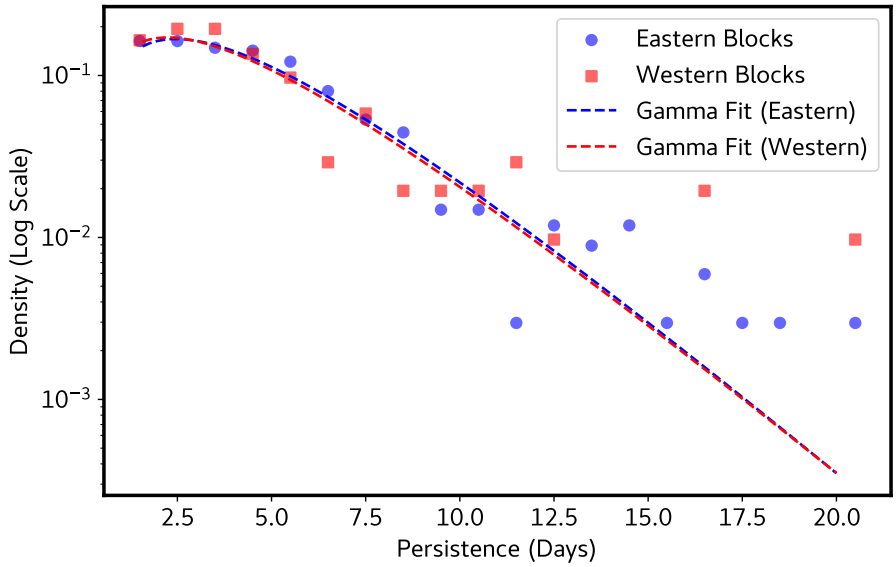


Figure 4.4: Log-scaled density distribution of blocking persistence (in days) for ENP and WNP blocks with $\alpha = 0.25$. The fitted gamma distributions for both cases are also shown.

Figure 4.5a and Figure 4.5c represent the typical-analogue pair for the ENP block, while Figure 4.5b and Figure 4.5d correspond to the WNP block pair. Both reference-analogue pairs exhibit a high degree of similarity in their (Z_{500}) distributions, indicating that the analogue blocks effectively capture the large-scale structure of the reference blocks. The differences between the selected reference and analogue blocks, depicted in Figures 4.5e and 4.5f, reveal anomalies within a range of $\pm 720\mathrm{m}$, which is significantly smaller than the typical anomaly range of $\pm 1000\mathrm{m}$ observed between two randomly selected blocking days. This suggests that the analogue blocks resemble their respective reference blocks much more closely, with only minor variations in intensity and spatial extent. The anomaly patterns highlight localized differences, which may be attributed to transient synoptic-scale features or differences in block persistence. These findings reinforce the reliability of the analogue approach in identifying predictability and stability of atmospheric blocking patterns.

4.3.4 Stability and predictability of identified blocks

Figure 4.6a illustrates the evolution of the average error for the first 50 reference-analogue pairs, quantifying the divergence between their trajectories. The shaded regions denote the standard deviation, capturing the variability in error growth across different blocking

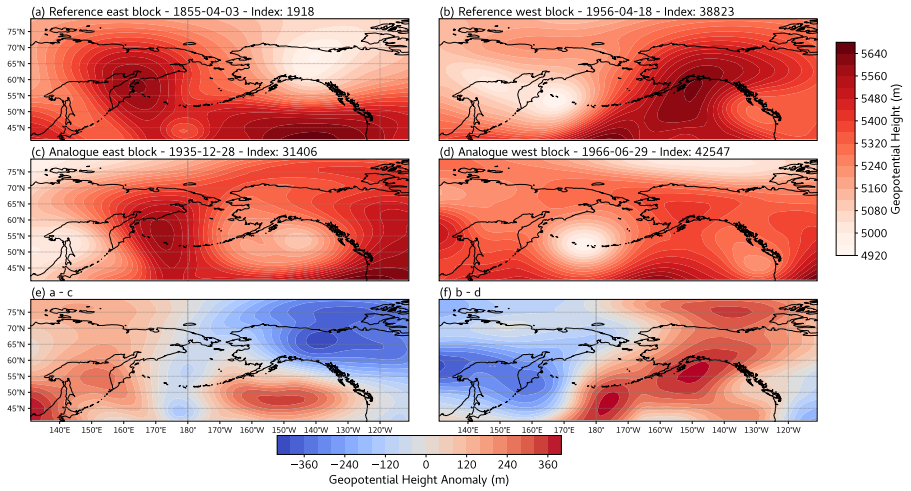


Figure 4.5: Z_{500} distribution of the reference ENP and WNP blocks, respectively is represented in **(a)** and **(b)**, while **(c)** and **(d)** correspond to their analogue blocks. **(e)** and **(f)** depict the (Z_{500}) anomalies between the typical and analogue blocks for the ENP and WNP cases, respectively.This example is randomly drawn from the $\alpha = 0.25$ first-50 subset.

cases. The results indicate that the trajectories of ENP blocks diverge more rapidly than those of WNP blocks, suggesting that ENP blocks exhibit lower stability.

Figure 4.6b presents the bootstrap mean error for both ENP and WNP blocks, along with their respective 95% CIs. The use of the bootstrap method (with replacement) enhances statistical robustness by resampling the data to estimate uncertainty. The widening confidence intervals over time reflect an increasing separation between reference and analogue blocks, reinforcing the idea that blocking predictability diminishes with lead time. This decline is pronounced for ENP blocks, indicating a greater rate of divergence compared to WNP blocks. Curves end when too few pairs remain because one or both blocks terminate or splits, so the valid sample becomes small. The bootstrap shading shows the 95% CI of the mean, naturally narrower (scaling as $\propto 1/\sqrt{n}$) than the $\pm 1\,\sigma$ shading in panel4.6(a), which reflects the spread across individual cases and it terminates earlier because we require a minimum effective sample size for stable intervals; by contrast, the $\pm 1\,\sigma$ shading can be shown for smaller samples and therefore may extend further in lead.

Figure 4.6c depicts the averaged growth rate of the logarithm of the error, which is equivalent to the definition of the Lyapunov exponents, which characterizes how quickly small perturbations in initial conditions amplify, offering insight into the chaotic behavior of atmospheric blocking. Higher values correspond to increased instability and reduced predictability. Note that in the case of a pure exponential behavior along the dominant

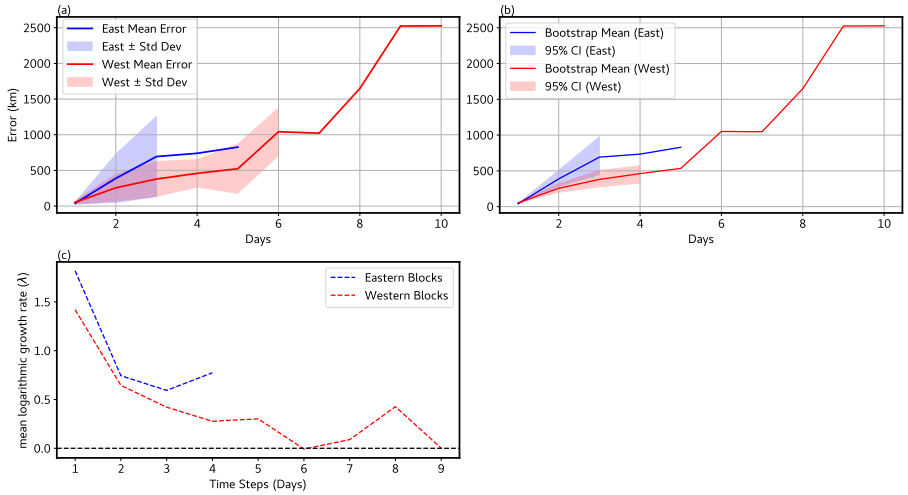


Figure 4.6: Evolution of error and logarithmic growth rate for ENP and WNP blocks, considering $\alpha = 0.25$ and the first 50 reference-analogue pairs with the smallest initial error. **(a)** Mean error growth over time for ENP and WNP blocks, with shaded regions representing the standard deviation. **(b)** Bootstrap mean error with 95% confidence intervals for both block types. Curves terminate where too few pairs remain because one or both blocks cease or splits.**(c)** Mean logarithmic growth rate over time, comparing the stability characteristics of ENP and WNP blocks.

local instability, this averaged growth rate would have been constant as a function of time.

The results suggest that ENP blocks exhibit larger logarithmic growth rate, implying a larger sensitivity to initial perturbations and, consequently, lower predictability compared to WNP blocks. Over time, the growth rate decreases for both cases, that could indicate either the progressive saturation of the error as expected when the error becomes large Nicolis et al. [1995]; Vannitsem and Nicolis [1997a], or the increase of predictability of the blocking after its onset. Disentangling one from the other would need to make model experiments with very small initial condition errors at different stages of the development of blocking. The analysis above however indicates the strong instability of ENP blocks over WNP blocks.

A key clarification is warranted regarding the nature of positional error growth in the blocking events shown. As discussed in details in Bohr et al. [1998], one should distinguish between the Eulerian and Lagrangian Lyapunov instabilities. The first one is associated with the difference in the initial state of the background flow, while the second related with the spatial difference between the positions of the structures under interest, i.e the

blocking events. Here both Lagrangian and Eulerian errors are affecting the dynamics, and one cannot distinguish between the two here as these are intertwined. In Bohr et al. [1998], it is also shown that in the presence of both errors, the largest exponent among the Lagrangian and Eulerian Lyapunov instabilities is controlling the error evolution. We thus suspect that in our case the maximum Lyapunov exponent between the Eulerian and Lagrangian approaches is at play. The first value of Figure 4.6c can then be viewed as an estimate of the dominant local (in physical space) Lyapunov instability of the blocking events.

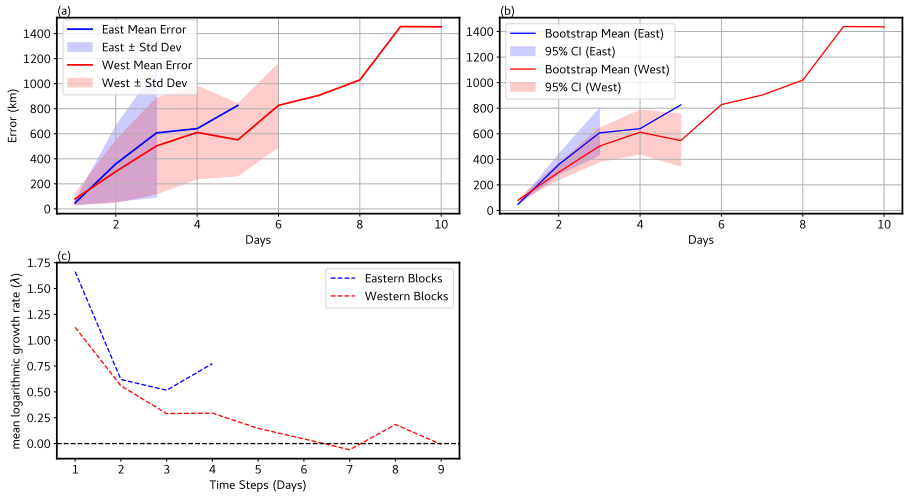


Figure 4.7: Same as Figure 4.6 but with $\alpha = 0.25$ considering first 75 reference-analogue pairs

The same analysis was repeated for the first 75 reference–analogue pairs, as shown in Figure 4.7. In Figures 4.7a and b, the average error evolution for ENP and WNP blocks appears nearly indistinguishable, indicating reduced contrast compared to Figures 4.6a and b. However, a slight difference remains, with ENP blocks still exhibiting a marginally higher rate of error growth than their WNP counterparts. The variability, quantified as the spread in error evolution across the reference–analogue pairs calculated using both the standard deviation and the bootstrap 95% confidence interval overlaps for both cases. This reduction in the difference between the average error evolution suggests that increasing the sample size introduces greater diversity in blocking characteristics with larger initial condition errors, leading to a broader representation of stability and transition behaviours. As a result, the initially observed contrast between ENP and WNP blocks diminishes, highlighting the influence of sample selection on assessing blocking predictability. Mean logarithmic growth rate in Figure 4.7 shows comparable difference for both cases by highlighting lower predictability for ENP blocks as same as in Figure 4.6. Despite increasing the sample size from 50 to 75 cases, the logarithmic growth rate continue to exhibit significantly different values for ENP and WNP blocks. This suggests

that the inherent instability of ENP blocks is a fundamental characteristic, less dependent on the number of selected cases.

The analysis was repeated for $\alpha = 0.20$ (figures are included in the appendix **??**), and the resulting error evolution and mean logarithmic growth rate for the first 50 cases are presented in Figure A3. The mean error evolution exhibits a similar pattern to previous analyses, with higher values for ENP blocks, reaffirming their lower stability. However, the logarithmic error growth rate (Figure A3c) shows a distinct behaviour: initial differences between ENP and WNP blocks gradually diminish, leading to an overlap on day 2. As time progresses, the divergence becomes significant again, particularly on days 3, 4, and 5, further supporting the conclusion that ENP blocks are inherently more unstable than WNP blocks.

For the first 75 cases (Figure A4), a similar pattern emerges. Initially, ENP blocks exhibit higher error values, but beyond the fifth day, the error evolution of ENP and WNP blocks becomes more comparable, leading to an overlap. The logarithmic error growth rate follows a non-monotonic behavior: higher initial values for ENP blocks, followed by relatively lower values on days 3 and 4, and a subsequent increase on day 5.

Reducing the threshold α from 0.25 to 0.20 increases sensitivity to smaller-scale variability by allowing a broader range of blocking events. This broader inclusion introduces greater variability in error growth patterns, as reflected in the non monotonic behavior of logarithmic error on days 3 and 4. With a less stringent analogue selection, initial differences between reference and analogue blocks are slightly larger, which may explain overlapping growth phases—such as day 2 for the 50-case scenario and day 5 for the 75-case scenario—before divergence occurs. These effects are further amplified in larger samples, where a mix of more persistent and less stable blocks leads to alternating phases of stronger and weaker error growth.

In contrast, using a stricter threshold of $\alpha = 0.25$ ensures the selection of only the most structurally similar blocking events, making the differences in their instability characteristics more apparent. Despite the added variability introduced at $\alpha = 0.20$, the underlying instability of ENP blocks remains evident, as they consistently exhibit higher error values and larger mean logarithmic growth rates over time.

4.4 conclusion

This study investigates the predictability of Eastern and Western North Pacific atmospheric blocking events using an analogue - based approach. Our results provide a dynamical complement to established descriptions of North Pacific blocking occurrence and structure. Prior studies have documented robust blocked day climatologies and regional preferences based on gradient-reversal indices and related diagnostics [e.g. Davini et al., 2012; Barriopedro et al., 2006; Lupo et al., 2019], including over the Kuroshio - Oyashio extension and Gulf of Alaska sectors. The composite Z_{500} fields conditioned on blocked days (Fig. 4.3) align with these preferred locations, while our analogue - based

metrics quantify how quickly initially similar states diverge, thereby translating structural preferences into a finite-time predictability perspective.

The east - west asymmetry we find, systematically faster divergence (larger mean logarithmic growth rates) for ENP blocks fits with well-known contrasts in the background flow. In the northwest Pacific near the Russian coast and the Kuroshio - Oyashio Extension (ENP), the jet entrance region, sharp SST fronts, and strong baroclinicity favour frequent wave packet genesis, active transient eddy forcing, and Rossby wave breaking, all of which enhance sensitivity to small perturbations and shorten intrinsic predictability [Masato et al., 2012; Woollings et al., 2018; Qiu et al., 2017; O'Reilly and Czaja, 2015; Che et al., 2021; Hwang et al., 2020]. By contrast, many WNP blocks occur in the downstream of the jet core, where ridges can be more quasi-stationary and sometimes anchored by coastal or orographic influences, yielding slower error growth and longer predictability horizons [Breeden et al., 2020; Neal et al., 2022; Woollings et al., 2018]. In this view, background wave dispersion and transient eddy forcing modulate blocking stability in a way that naturally produces lower predictability for ENP than for WNP, even when initial structures are similar [Woollings et al., 2018; Hwang et al., 2020].

Methodologically, our analogue framework complements persistence based descriptors and ensemble-forecast evaluations of blocking predictability [Plaut and Vautard, 1994; Matsueda, 2009]. Persistence distributions quantify how long blocks last but do not directly capture sensitivity to small perturbations. Ensemble forecasts provide such sensitivity but can be model and configuration dependent. By contrast, the analogue growth rate diagnostic we employ computed from reference - analogue pairs in Z_{500} and summarized across many cases offers a model agnostic, data driven estimate of local (phase-space) predictability, in the spirit of classical analogue ideas [Lorenz, 1969; Yiou, 2014] and more recent dynamical-systems applications to midlatitude regimes [Yiou et al., 2007; Faranda et al., 2017, 2023].

These findings also speak to model evaluation. MIROC6 exhibits relatively small biases over the North Pacific blocking sector compared with commonly used reanalyses [Lohmann et al., 2024], and our east - west contrast persists across reasonable thresholds ($\alpha = 0.20, 0.25$) and sample choices (first 50 or first 75). This indicates that analogue-based growth rates provide a compact benchmark for assessing whether climate models reproduce not only the occurrence of blocks but also their intrinsic predictability, complementing standard blocked-day counts and persistence metrics. As a model-dependence sensitivity, we repeated the full pipeline with IPSL-CM6A-LR and MPI-ESM1 ($\alpha = 0.25$; first 50 nearest pairs; see Figs.S1 and S2 in the supplementary material), MIROC6 retains a clear ENP $>$ WNP early-time divergence where as IPSL-CM6A-LR shows only a weak ENP - WNP contrast; and in MPI-ESM1 the reference - analogue pair's initial separation for ENP block is substantially larger (≈ 693 km), which raises mean error levels, yet the Mean logarithmic growth rate which evaluates finite time divergence relative to the initial mismatch still yields lower predictability for ENP, consistent with MIROC6. This model dependence aligns with independent assessments of North Pacific blocking biases [Lohmann et al., 2024], suggesting that analogue based predictability diagnostics are most informative when applied to models with realistic blocking occurrence and structure.

Our results show that blocks adjacent to the Asian boundary (ENP) exhibit systematically faster early-time divergence than blocks adjacent to the North American boundary (WNP), implying shorter intrinsic predictability for ENP. This east west contrast persists across thresholds and sample sizes and is consistent with the view that basin - scale boundary constraints modulate regime stability, extending the idealized finding of Xavier et al. [2024] to a comprehensive GCM.

Looking ahead, several extensions can deepen and broaden our findings. First, a seasonal decomposition (e.g., DJF vs. JJA) can be pursued when event counts permit, complementing our annual sampling that was chosen to ensure robust uncertainty quantification. Beyond Z_{500} fields and center of mass tracking, incorporating dynamical diagnostics (e.g., potential-vorticity gradients, wave activity fluxes, and Rossby wave breaking metrics) will help attribute the east–west contrast to specific mechanisms. We also intend to test alternative blocking indices, thresholds, and modest spatial smoothing to assess metric dependence. Together, these extensions will further quantify and explain the east - west predictability contrast, building on the robust result that ENP exhibits larger early-time growth rates than WNP across thresholds and sample sizes.

Chapter 5

Beyond the mechanistic view of the Lorenz energy cycle of blocking events

5.1 Introduction

Atmospheric blocking refers to large-scale, quasi-stationary, high-pressure anomalies often in the form of anticyclonic systems that disrupt the prevailing westerly flow for several days to weeks, sometimes exceeding two weeks in duration [Rex, 1950; Woollings et al., 2018].These systems are typically associated with the splitting or strong meandering of the jet stream, which can divert storm tracks and lead to persistent and extreme weather anomalies such as heatwaves, droughts, flooding events, and cold-air outbreaks in the mid-latitudes [Barriopedro et al., 2011; Pfahl and Wernli, 2012; Sousa et al., 2018]. Blocking events are particularly impactful because of their ability to maintain anomalous circulation patterns over a region for extended periods, thereby amplifying the intensity and duration of associated extremes [Trigo et al., 2004; Sillmann et al., 2011]. From a dynamical perspective, blocking is often characterized by the formation of a quasi-stationary Rossby wave pattern that resists the typical eastward progression of synoptic disturbances [Shutts, 1983; Nakamura and Huang, 2018]. The onset, maintenance, and decay of blocking involve complex multi-scale interactions between transient eddies, planetary waves, and mean flow, and remain a subject of active research [Matsueda, 2011; Woollings et al., 2010]. Despite decades of study, blocking remains one of the most challenging phenomena for numerical weather prediction (NWP) and climate models to simulate accurately models often underestimate blocking frequency and persistence, especially over the Euro-Atlantic and North Pacific sectors [Davini and D'Andrea, 2020; Matsueda, 2009]. Model biases have been linked to systematic errors in representing large scale circulation, storm track activity, and Rossby wave breaking processes [Scaife et al., 2010; Matsueda, 2009].

A deeper dynamical understanding of blocking can be achieved by examining the interactions among the principal atmospheric energy reservoirs, kinetic energy (KE), available potential energy (APE), and their conversions as well as their coupling with surface thermal conditions such as ground temperature [Peixoto and Oort, 1992]. The Lorenz Energy Cycle (LEC) provides a classical framework for diagnosing these processes, quantifying how diabatic heating, radiative processes, and surface fluxes generate APE, how APE is converted into KE through baroclinic processes, and how KE is dissipated through friction [Lorenz, 1955; Ulbrich and Speth, 1991]. In the LEC formalism, energy is partitioned into zonal mean and eddy components, allowing the identification of large-scale circulation features and transient disturbances that contribute to climate variability [Oort and Peixóto, 1983; Marques et al., 2009].

Blocking events interact strongly with the Lorenz cycle by altering the efficiency of energy conversions between mean and eddy reservoirs. For example, the persistence of a blocking anticyclone tends to suppress transient eddy activity, leading to reduced baroclinic conversion from eddy APE to eddy KE, while simultaneously enhancing conversions within the zonal mean component [Shutts, 1983; Luo, 2005]. Studies have shown that the onset of blocking is often associated with anomalous energy accumulation in the eddy APE reservoir, followed by a reorganization of conversion pathways that sustains the high pressure anomaly [Nakamura and Huang, 2018; Pfahl et al., 2015]. This modulation of the energy cycle not only influences the longevity of blocking but also shapes the intensity of associated extreme events, such as prolonged heatwaves and cold-air outbreaks [Trigo et al., 2004; Sillmann et al., 2011].

In chapter 3 we used a reduced order land atmosphere coupled model [Li et al., 2018; Demaeyer et al., 2020] to show that blocking predictability depends on the position of the block relative to the topographic features, with blocks west of such features exhibiting lower predictability and greater instability than those to the east. Building on this, Xavier et al. [2025] and chapter 4 we analyzed CMIP6 MIROC6 simulations [Tatebe et al., 2019b] to assess whether these predictability asymmetries also arise in more realistic model contexts. Surprisingly, their results indicated the opposite behavior in the North Pacific: eastern blocks were generally less predictable and more unstable than their western counterparts. While these studies confirmed that substantial predictability differences exist, the physical mechanisms behind them remained unresolved.

In the present study, we focus on understanding whether the variability of eastern and western blocking events differs in terms of their directional causal interactions among the Lorenz Energy Cycle (LEC) reservoirs, namely kinetic energy (KE), available potential energy (APE), and the associated ground temperature anomalies. While the predictability of these regimes, examined earlier, quantifies the deterministic error growth and thus the predictability, the information flow framework of Liang and Kleeman provides a complementary, probabilistic perspective by quantifying how uncertainty or information is exchanged between system components [Liang and Kleeman, 2005; Liang, 2014]. The Liang - Kleeman causality measure, derived rigorously from the governing equations of dynamical systems, estimates the net rate of information transfer from one variable to another. It is inherently asymmetric, allowing one to identify directionality in causal influence even

in the presence of stochastic forcing [Liang, 2016]. This framework has been successfully applied in climate science to unravel causal dependencies in ocean–atmosphere variability, Arctic sea-ice changes, and tropical rainfall dynamics [Dörr et al., 2024; Docquier et al., 2024; Stips et al., 2016], making it a powerful tool to investigate the energetic linkages and causal structures underlying the variability of atmospheric blocking.

The paper is organized as follows: Section 5.2 describes the models employed and the methodological framework adopted for the analysis. Section 5.3 presents and interprets the main findings of the study. Finally, Section 5.4 summarizes the key conclusions and outlines potential directions for future research.

5.2 Data and Methodology

For the information transfer index analysis, we used the output of the QGS land - atmosphere coupled model described in [Xavier et al., 2024], adopting all parameter values specified therein. For the analysis of more realistic scenarios, we employed CMIP6 MIROC6 historical simulations [Tatebe et al., 2019b; Xavier et al., 2025]. Since the aim of the study is to identify differences in the information transfer among selected parameters according to a blocking event's geographical position and its proximity to topographical features, we separated the events into *eastern* and *western* blocks.

In the QGS experiments, eastern blocks are defined as those in which the blocking high occurs *downstream* of the underlying topography, whereas western blocks occur *upstream* of the applied topography. This classification was performed using Gaussian mixture clustering, as described in detail by Xavier et al. [2024]. In the MIROC6 simulations, we focused on the North Pacific sector, which is dynamically comparable to the applied topography in the QGS setup, the mountains on either side and the valley in between in QGS can be analogized to the North American continent and part of Russia on either side of the Pacific, with the ocean basin acting as the valley. Eastern and western North Pacific blocks were identified using the well established two dimensional blocking index proposed by Davini et al. [2012], with the separation methodology adapted from Xavier et al. [2025]. Here, eastern North Pacific blocks are defined as those occurring downstream of the topography (i.e., east of Russia), while western North Pacific blocks occur upstream of the topography (i.e., west of North America).

To examine and compare the typical characteristics and information transfer between the selected parameters during blocking and non-blocking periods, we further calculated indices for both blocked and non-blocked conditions in the same geographical regions. For this, all days identified as blocking regardless of whether they were eastern or western events were combined into a set of "blocked" days, while all other days without blocking were classified as "non-blocked" days.

An essential step in the information transfer index analysis is the identification of crucial parameters that influence the phenomenon of interest (here, atmospheric blocking), its stability, and its maintenance. Following the strategy of the Lorenz energy cycle

[Lorenz, 1955], we selected and computed the kinetic energy (KE) and available potential energy (APE) from the outputs of the QGS and MIROC6 simulations, as described below.

Kinetic Energy (KE):

$$u = -\frac{\partial \psi}{\partial y}, \quad v = \frac{\partial \psi}{\partial x}, \quad \mathrm{KE} = \frac{1}{2}\left(u^2 + v^2\right) \tag{5.1}$$

where ψ is the streamfunction from QGS diagnostics or (u, v) are directly taken from MIROC6 horizontal wind outputs.

Available Potential Energy (APE):

$$\mathrm{APE} \approx \frac{g^2}{2\,N^2}\left(\frac{T'}{\overline{T}}\right)^2 \tag{5.2}$$

where T' is the temperature anomaly in QGS or temperature anomaly computed from air temperature at 500 hPa from MIROC6 outputs), $\overline{T}$ is the mean state, and N^2 is the Brunt–Väisälä frequency squared.

For QGS, (u, v) are derived from ψ using horizontal derivatives on the model grid and T' is computed from the middle-atmospheric temperature field. For MIROC6, (u, v) are taken directly from model wind outputs and T' is computed from air temperature at 500 hPa anomalies. In this study, APE was computed in normalized form, proportional to the Lorenz [1955] definition, omitting constant multiplicative factors such as g^2 and N^2, since the Liang - Kleeman information transfer measure is invariant under constant scaling and depends only on the temporal variability and directional coupling between variables.

Since atmospheric blocking events are often associated with pronounced fluctuations in near-surface temperature due to persistent anomalies in radiative and advective heat fluxes [Pfahl and Wernli, 2012; Seneviratne et al., 2010; Woollings et al., 2018], the third parameter selected for the information transfer analysis is *ground temperature* (GT) in the QGS model, whereas in the MIROC6 simulations it is represented by the `tas` - near-surface air temperature field, which provides a standard approximation of temperature near the surface.

After computing KE, APE, and ground temperature time series for each category (Eastern blocks, Western blocks, blocked, and non-blocked periods), we calculate the Liang - Kleeman information transfer index [Liang and Kleeman, 2005; Liang, 2014, 2016], which measures the net directional causality from variable X to variable Y as

The rate of information transfer from variable X_j to variable X_i is computed using the multivariate linear form of the Liang - Kleeman information flow framework [Liang and Kleeman, 2005; Liang, 2014, 2021b]:

$$T_{j\to i} = \frac{1}{\det(\mathbf{C})}\sum_{k=1}^{d}\Delta_{jk}\,C_{k,di}\,\frac{C_{ij}}{C_{ii}}, \tag{5.3}$$

where $\mathbf{C}$ is the covariance matrix of all variables under consideration, d is the number of variables, Δ_{jk} represents the cofactors of $\mathbf{C}$, $C_{k,di}$ is the sample covariance between variable X_k and the time derivative of X_i, C_{ij} is the sample covariance between X_i and X_j, and C_{ii} is the variance of X_i. Positive values of $T_{j\to i}$ indicate that X_j increases the uncertainty (or entropy rate) of X_i, whereas negative values imply a stabilizing or constraining influence. This formulation follows the linear model with additive noise assumption proposed by Liang [2021b].

5.3 Results and Discussions

5.3.1 QGS land atmosphere coupled model

Figure 5.1 summarizes the dependence structure among kinetic energy (KE), available potential energy (APE), and ground temperature (GT) in the QGS land - atmosphere coupled model across four regimes: blocked days, non-blocked days, western-blocks, and eastern-blocks. The first column (panels **a**, **d**, **g**, **j**) shows the correlation matrices R for each regime. The second column (panels **b**, **e**, **h**, **k**) displays the Liang - Kleeman information transfer rates τ (in %), with matrix entries interpreted row $\to$ column; colors indicate the sign (red $=$ increases the variability; blue $=$ negative, decreases the variability), and the magnitude reflects the strength of the influence. The third column (panels **c**, **f**, **i**, **l**) provides directed graphs of statistically significant causal links, where arrowheads denote direction and line width is proportional to $|\tau|$. In the matrix panels, black contours highlight links that are significant at the $\alpha = 0.05$ level.

As seen in the second column matrices, the self–influence terms on the diagonals are statistically significant in all four regimes (Fig. 5.1**b**,**e**,**h**,**k**), with magnitudes ranging from about 13% to 80%. In the Liang - Kleeman framework, a significant diagonal term indicates that the time tendency of a variable depends on its own state (i.e., intrinsic memory or auto feedback; Liang, 2021b). The self-influence indeed depends on the process and the situation considered, and is here dominating the evolution of the uncertainty or variability of each individual process, but what is more interesting is the influence of the other variables, the non diagonal terms.

Beyond the diagonals, there are robust, bidirectional causal interactions among KE, APE, and GT in both blocked and non blocked states (Fig. 5.1**c**,**f**,**i**,**l**). During blocking, KE exerts a strong influence that *increases the uncertainty or variability* of GT (Fig. 5.1**c**; $\tau_{\mathrm{KE}\to\mathrm{GT}} \approx +65.52\%$), with a slight increase in GT (Fig. 5.1**a**; $R \approx +0.14$) consistent with the notion that persistent, quasi stationary flow anomalies modulate surface temperature via advective and radiative effects when baroclinic activity is suppressed. In the non–blocked regime, the dominant exchange emerges between KE and APE (Fig. 5.1**f**; $\tau_{\mathrm{KE}\to\mathrm{APE}} \approx +32.06\%$ and $\tau_{\mathrm{APE}\to\mathrm{KE}} \approx -57.43\%$), indicating that KE fluctuations enhance APE variability while APE acts to *reduce variability* in KE. This pattern aligns with Lorenz–cycle expectations: in more baroclinically active (non–blocked) conditions, KE - APE coupling is enhanced through eddy processes and baroclinic adjustment, whereas in

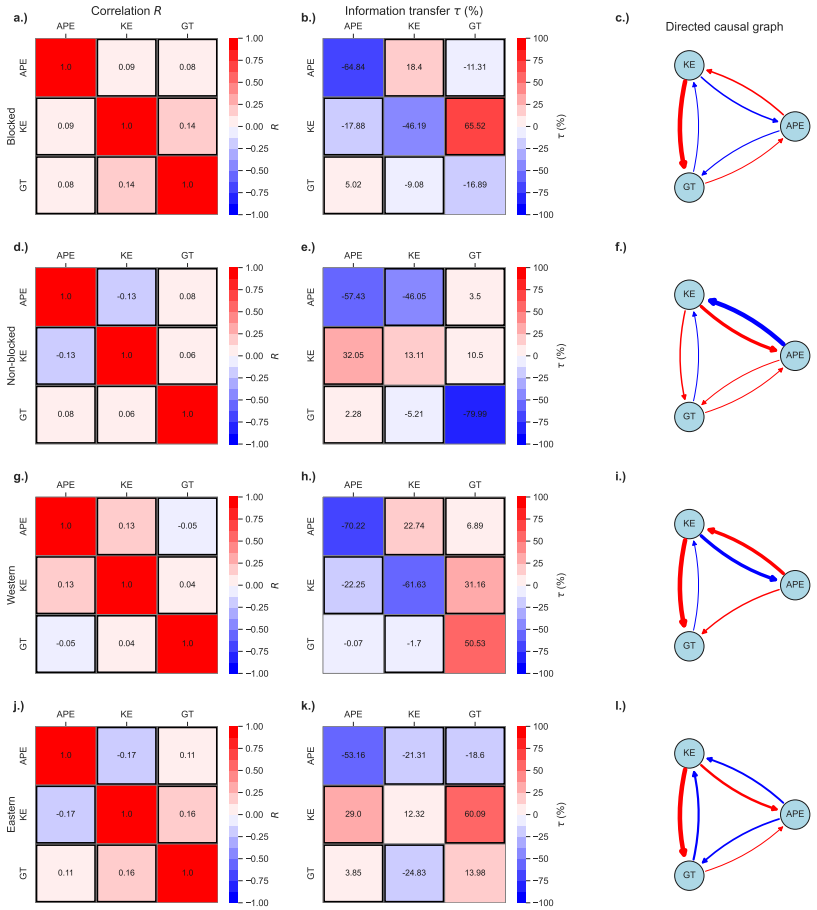


Figure 5.1: Causality and correlation among kinetic energy (KE), available potential energy (APE), and ground temperature (GT) in the QGS land - atmosphere coupled model. The first column, panels **(a)**, **(d)**, **(g)**, and **(j)**, shows the correlation matrices R for, respectively, blocked days, non-blocked days, western-blocks, and eastern-blocks conditions. The second column, **(b)**, **(e)**, **(h)**, and **(k)** shows the Liang - Kleeman rate of information transfer τ (in %; rows $\rightarrow$ columns). Colors indicate the sign (red $=$ positive, increases the variability; blue $=$ negative, decreases the variability), and magnitude reflects strength. The third column, **(c)**, **(f)**, **(i)**, and **(l)** displays directed graphs of statistically significant causal links; arrowheads indicate direction and line width is proportional to $|\tau|$. Black contours in the matrices mark links whose two-sided 95% confidence intervals.

blocked conditions reduced eddy conversions shift influence toward surface - atmosphere coupling and KE→GT pathways.

Both eastern and western blocks exhibit a pronounced, positive information transfer from KE to GT (here interpreted as a hallmark of the blocking regime) with a larger magnitude in the eastern blocks (Fig. 5.1**l**; $\tau_{\mathrm{KE}\to\mathrm{GT}} \approx +60.09\%$) than in the western blocks (Fig. 5.1**i**; $\tau_{\mathrm{KE}\to\mathrm{GT}} \approx +31.16\%$). Beyond this shared surface impact pathway, the KE - APE coupling differs markedly across the two regimes. In western blocks, KE acts to *reduce variability* in APE ($\tau_{\mathrm{KE}\to\mathrm{APE}} \approx -22.25\%$) while APE acts to *increase variability* in KE ($\tau_{\mathrm{APE}\to\mathrm{KE}} \approx +22.74\%$), a pattern consistent with the blocked-state behavior.

5.3.2 CMIP6 MIROC6 simulations

Repeating the analysis with MIROC6 (Fig. 5.2) yields a markedly different causal structure, consistent with the distinct underlying dynamics of a full-physics GCM versus the dry QG framework. Diagonal (self-influence) terms remain statistically significant across all four regimes, with magnitudes of roughly 9 - 53%, somewhat lower than in the QGS land - atmosphere model. In MIROC6, both KE and APE generally act to *reduce their own variability* in all regimes, except that APE exhibits a tendency to *increase its own variability* in the non-blocked state. Beyond the diagonals, blocked and non-blocked composites display broadly similar cross-interactions: GT tends to *increase variability* in APE (i.e., GT→APE is positive) and to *reduce variability* in KE, while KE reduces variability in both GT and APE; APE exerts a weak influence that *increases variability* in KE but reduces variability in GT. The key difference between these two regimes is the absence of a significant GT→APE link during blocked conditions, whereas it is present in the non-blocked state. Consequently, for MIROC6 the most diagnostic separation between blocked and non-blocked composites lies in the sign of APE's self-influence and the absence of information transfer from GT to APE (blocking: $\tau_{\mathrm{APE}\to\mathrm{APE}} \approx -8.84\%$ vs. non-blocked: $\tau_{\mathrm{APE}\to\mathrm{APE}} \approx +26.25\%$), rather than in wholesale changes of cross-reservoir couplings.

A pronounced east - west asymmetry emerges within the blocking regime. Eastern blocks resemble the blocked composite in most respects but exhibit a near complete decoupling between GT and APE (no significant transfer in either direction). Western blocks, by contrast, are dynamically more active from the surface upward (Fig. 5.2**i**): GT strongly *increases variability* in both KE and APE (GT→KE $\tau \approx +37.77\%$, GT→APE $\tau \approx +34.85\%$), with GT→KE notably stronger than in any other regime. Taken together, these results suggest that, in MIROC6, the dominant blocking signature is most clearly expressed by the *eastern* blocks (reduced GT - APE coupling and more internally variability-limiting energetics), while western blocks display enhanced surface-to-energetics pathways indicative of stronger boundary-layer or diabatic control. We note that statistical power for western blocks is limited by sample size (fewer blocked days over 150 years), which may bias significance assessments.

In the Lorenz energy cycle (LEC) perspective [Lorenz, 1955; Peixoto and Oort, 1992; Holton and Hakim, 2013; Wallace and Hobbs, 2006], QGS results align closely with the

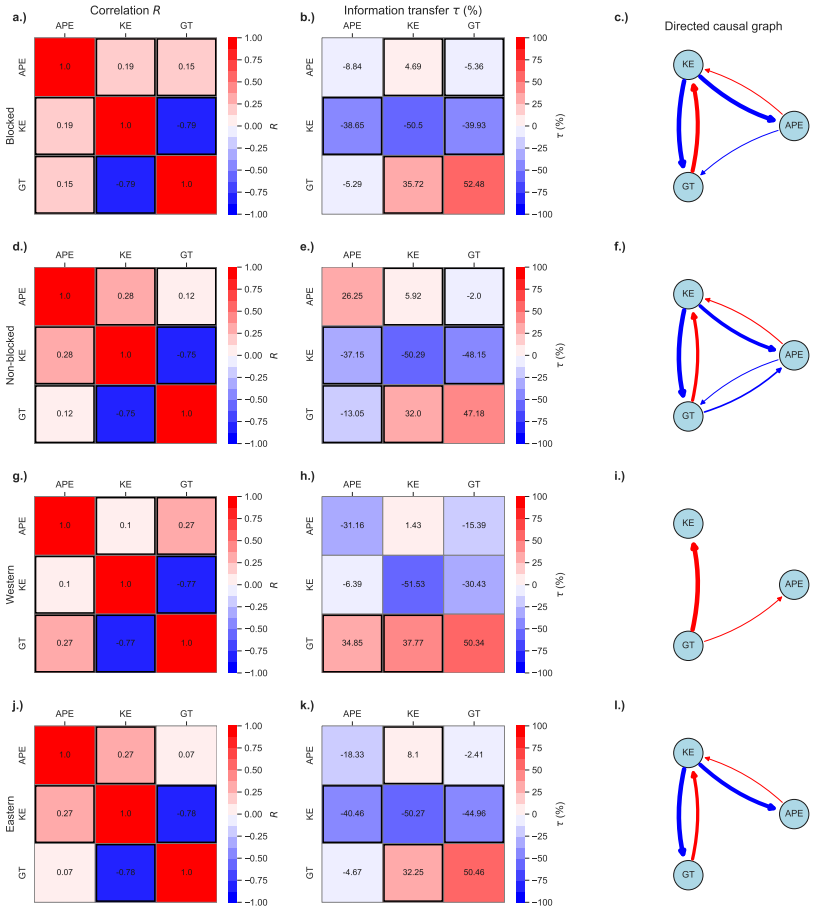


Figure 5.2: Causality and correlation among kinetic energy (KE), available potential energy (APE), and ground temperature (GT) in the MIROC6 same as figure 5.1 .

canonical picture in which reduced baroclinic conversion during blocking suppresses eddy KE production and redirects influence toward surface temperature anomalies maintained by anomalous advection and radiative persistence. The MIROC6 behavior departs in two ways that are physically plausible in a moist, fully coupled GCM: (i) diabatic heating and boundary-layer processes modulate the effective APE reservoir and its conversions, altering apparent KE $\leftrightarrow$ APE pathways; and (ii) surface fluxes and land - atmosphere coupling (reflected in GT) can directly feed back on free-tropospheric energetics, especially in western blocks where GT$\rightarrow$KE and GT$\rightarrow$APE are strongest [see, e.g., Seneviratne et al., 2010; Pfahl and Wernli, 2012; Woollings et al., 2018]. These differences help explain why the QGS model, closer to dry dynamics, quasi-geostrophic energetics exhibits LEC-consistent causal patterns more cleanly, whereas MIROC6 integrates additional moist and boundary processes that complicate the direct mapping between statistical causality and idealized LEC conversions.

5.4 Conclusions

This study aims to investigate whether the variability of eastern and western atmospheric blocking regimes differs in terms of their underlying energetic couplings among kinetic energy (KE), available potential energy (APE), and near-surface temperature (GT). To this end, we apply the Liang–Kleeman information flow (LKIF) framework [Liang and Kleeman, 2005; Liang, 2014, 2016, 2021b], which quantifies directional information exchange among interacting variables based on first principles of information theory. The analysis is conducted using both an idealized quasi-geostrophic (QGS) land–atmosphere model and historical simulations from the CMIP6 MIROC6 dataset [Tatebe et al., 2019b], allowing a comparative assessment of how blocking variability and its associated energy pathways are represented across model hierarchies.

In summary, applying the Liang - Kleeman information-flow framework to both the idealized QGS land atmosphere model and the CMIP6 MIROC6 simulations reveals that blocking variability is characterized by distinct patterns of directional energetic coupling. A robust, positive KE$\rightarrow$GT pathway emerges as a consistent hallmark of blocked regimes across both models, indicating that surface temperature variability is strongly driven by kinetic energy fluctuations during persistent flow anomalies. The strength and structure of KE–APE coupling, however, vary markedly across regimes and model hierarchies. In the QGS model, non blocked states exhibit strong, bidirectional KE–APE interactions (KE$\rightarrow$APE and APE$\rightarrow$KE), reflecting more dynamically active and energetically connected conditions, whereas blocked states show a weakening of this coupling and a shift toward enhanced KE$\rightarrow$GT influence. MIROC6, by contrast, displays smaller contrasts between blocked and non–blocked composites, with the main diagnostic differences arising from changes in APE's self-influence and the presence or absence of GT$\rightarrow$APE. These features likely reflect the additional role of moist processes, boundary-layer physics, and ocean coupling in redistributing variability among reservoirs in the coupled GCM.

East - west asymmetries further clarify the nature of variability control. In QGS, western blocks exhibit stronger APE$\rightarrow$KE influence, while eastern blocks retain more active

KE↔APE coupling, consistent with distinct dynamical modes of variability within the blocking regime. In MIROC6, eastern blocks most closely resemble the canonical blocked composite, whereas western blocks display enhanced GT→KE and GT→APE pathways, pointing to a greater role of diabatic and surface driven processes in modulating variability. Together, these results suggest that directional information flow provides a new, process aware framework for diagnosing how blocking regimes differ in their internal energetic organization and surface linkages across model hierarchies, without invoking explicit assumptions about deterministic predictability or energy conversion efficiency. Methodologically, the analysis employs linear multivariate LKIF with bootstrap confidence intervals at $\alpha = 0.05$ [Liang, 2021b], using normalized APE definitions invariant to constant rescaling. Future work should extend this framework to additional models and reanalyses, incorporate explicit moist or eddy energy partitions, and explore time-resolved (sliding-window) or nonlinear causality diagnostics to capture the evolving variability structure during blocking onset, maintenance, and decay.

Chapter 6

Conclusions

Atmospheric blocking and related large scale circulation regimes remain among the most challenging features of the midlatitude climate system to understand and predict. These quasi stationary flow anomalies strongly modulate storm tracks and drive extreme events such as heatwaves, cold spells, and flooding, making them of great societal relevance. Yet, their inherent variability, sensitivity to initial conditions, and dependence on background circulation continue to limit forecast skill beyond two weeks.

Motivated by these challenges, in this thesis we sought to investigate whether the variability and predictability of blocking can be systematically explained across model hierarchies, from low - order quasi geostrophic systems to comprehensive CMIP6 climate simulations. We asked how regime stability differs between zonal, blocking, and transitional flows, whether the location of blocking relative to topography influences predictability; and which energetic and thermodynamic pathways indigate these differences. By combining simplified models with complex GCMs and introducing information transfer tools to diagnose causal interactions, our work aimed to build a coherent framework that bridges theoretical understanding and real world relevance.

The sections below summarize the specific conclusions of each chapter in detailing and real world relevance.

6.1 Specific Conclusions

6.1.1 Can a low order land - atmosphere coupled model capture the variability and predictability large scale flow regimes in the atmosphere?

To answer this question, chapter3 has provided a detailed exploration of how variability and predictability of large - scale atmospheric flow regimes can be understood through a low order land atmosphere coupled model [Demaeyer et al., 2020; Li et al., 2018]. By

systematically varying the parameters of this quasi geostrophic framework and applying clustering techniques to isolate distinct regimes, we demonstrated that the model is capable of capturing the fundamental dynamical contrasts between zonal, blocking, and transitional states. Despite its reduced complexity, the model succeeds in reproducing essential aspects of *earthlike* circulation patterns, allowing us to identify the interplay between dynamical instability, topographic forcing, and the predictability of large scale flow regimes in existing in the model.

Our analysis confirmed that when the system have the coexistence of three regimes (w.r.t specific K_d), zonal, blocking, and transitional, the zonal flows emerge as the stable and predictable regime. This result is consistent with both theoretical expectations and prior empirical studies, underscoring that the quasi - linear nature of zonal patterns is less prone to rapid error growth than the more nonlinear, wave dominated blocking configurations [Charney and DeVore, 1979; Legras and Ghil, 1985; Reinhold and Pierrehumbert, 1982]. In contrast, blocking regimes were found to be more unstable, characterized by a shorter predictability horizon [Schubert and Lucarini, 2016; Lucarini et al., 2016; Lucarini and Gritsun, 2020]. These results reinforce the long standing view that blocking events are inherently harder to forecast, not only because of their rarity but also because of their larger heightened dynamical instability [Shutts, 1983; Nakamura and Huang, 2018].

In a certain K_d range where the system no longer supports a zonal regime but instead oscillates between two blocking regimes and a transitional state, the two blocking regimes exhibited entirely distinct predictability horizons, despite their similarity in their structure. Upon closer inspection of their morphology and spatial positioning of blocking highs relative to the model's imposed topography, we identified a key determinant: blocks forming on the windward (western) side of the topography tended to have lower predictability, whereas blocks forming on the leeward (eastern) side exhibited greater persistence and predictability. This geographical sensitivity highlights that the predictability of blocking is not an intrinsic property of the phenomenon alone but is strongly modulated by the relative positioning of the block with respect to orographic features.

We also investigated the behaviour of model dynamics by increasing its resolution. We observed a contraction of the regime space: only two regimes, zonal and blocking, remained distinct, both with predictability horizons of about two days. While this reduction in regime richness at higher resolution highlights the limitations of the simplified framework, it also points to the robustness of the core finding: blocking regimes, irrespective of their configuration, remain systematically less predictable than their zonal counterparts.

Taken together, these results demonstrate that low - order coupled models provide a powerful tool to unravel how variability and predictability of atmospheric regimes emerge from the interaction between internal dynamics and external constraints such as topography. The study emphasizes two central conclusions:

1. Zonal flow regimes are consistently more stable and predictable than blocking regimes in a multi - regime environment

2. During the situations where two blocking regime co-exists, predictability depends critically on their geographic positioning relative to topographic features, with leeward blocks showing higher persistence.

This second conclusion serves as a conceptual bridge to the next stage of the thesis. Having established within the reduced order framework that the location and morphology of blocking relative to topographical features can modulate predictability, the subsequent analysis explores whether such differences are also present in comprehensive climate models. Specifically, the next paper examines CMIP6 simulations, focusing on the North Pacific basin, to determine whether eastern and western blocks, situated relative to the Asian and American continents exhibit analogous variability structures to those identified in the idealized system. It is important to note, however, that no direct comparison is drawn between the two model hierarchies: the quasi-geostrophic model and the CMIP6 Earth system simulations represent fundamentally different atmospheric dynamics and levels of physical complexity. The goal is therefore not to evaluate their quantitative consistency but to assess whether the qualitative processes inferred from the idealized framework manifest in more realistic, coupled climate simulations.

6.1.2 Can the location of atmospheric blockings relative to topography affect their predictability in complex climate models such as CMIP6?

To address this question, we investigated North Pacific blocking events using an analogue-based framework applied to CMIP6 simulations, with particular emphasis on the MIROC6 model and supplementary analyses with IPSL-CM6A-LR and MPI-ESM1. Building on earlier findings from an idealized quasi geostrophic land atmosphere coupled model [Xavier et al., 2024], this study aims to assess whether the spatial positioning of blocking relative to continental boundaries in comprehensive climate models influences the predictability of North Pacific blocks. The objective is not to draw a direct comparison between the idealized and CMIP6 frameworks, which represent fundamentally different atmospheric dynamics, but rather to examine whether the qualitative relationships between blocking location and predictability identified in the reduced-order setting also emerge in the more realistic, coupled model environment.

The results provide a clear and consistent answer: yes, the predictability of blocking events differs depending on their geographical positioning, morphology, and structural relation to topographical features. Eastern North Pacific (ENP) blocks, located adjacent to the Asian boundary, systematically exhibit lower predictability than Western North Pacific (WNP) blocks, situated downstream near Alaska and the Gulf of Alaska coastlines. This east - west asymmetry was evident across multiple predictability diagnostics, including error growth in reference - analogue pairs and the mean logarithmic growth rate, and proved robust across sensitivity tests involving event thresholds (α= 0.20,0.25) and analogue sample sizes (first 50 and 75 pairs).

These findings indicate that background circulation conditions play a central role in modulating blocking stability. ENP blocks form in an environment dominated by strong baroclinicity, active transient eddies, and recurrent Rossby wave breaking near the jet entrance region [Masato et al., 2012; Woollings et al., 2018]. Such dynamical conditions enhance sensitivity to small perturbations, leading to rapid error divergence and a reduced intrinsic predictability. By contrast, WNP blocks often occur in the downstream jet exit region, where ridges are more quasi stationary and can be partially anchored by coastal orographic features. This context supports slower error growth, consistent with the longer predictability horizon of WNP blocks. Thus, the morphology and placement of blocking relative to basin boundaries emerge as key determinants of predictability in CMIP6 class climate simulations.

A second important result concerns the comparison between idealized and comprehensive frameworks. In the quasi geostrophic land–atmosphere model explored in Chapter3, we found that blocks forming on the western (upstream) side of topography were less predictable, while those on the eastern (downstream) side were more stable [Xavier et al., 2024]. In contrast, the CMIP6 simulations analysed here revealed the opposite asymmetry: ENP blocks (adjacent to Asia) were less predictable than WNP blocks (adjacent to North America). This apparent contradiction highlights the differing physics represented in the two modelling frameworks. The QGS system is a dry, low - order model where the regime dynamics are shaped primarily by topographic constraints and land - atmosphere coupling, whereas MIROC6 and other CMIP6 models include moist processes, boundary condition variability, and ocean atmosphere interactions. These additional processes profoundly alter the background state in which blocking develops, emphasizing that the mechanisms of predictability are model dependent and conditioned by the complexity of the climate system being represented.

But main results elucidated here is that the predictability of blocking is not uniform but strongly dependent on its spatial structure and proximity to topographical features. This indicates that blocking is not a singular regime but a family of dynamical states whose stability properties depend on both internal nonlinearities and the larger scale environment. The analogue framework employed here extends this understanding by translating spatial contrasts into measurable predictability differences, complementing existing descriptors such as persistence distributions [Tibaldi and Molteni, 1990; Schiemann et al., 2020b] and ensemble forecast skill metrics [Matsueda, 2009; Merryfield et al., 2020b].

Finally, our results demonstrate that CMIP6 models are capable of capturing not only the climatological distribution of blocking but also its predictability differences across regions, at least in models such as MIROC6 where blocking biases are relatively small [Tatebe et al., 2019b; Lohmann and *et al.*, 2024]. This underlines the value of analogue based diagnostics we developed can be used as a benchmark for model evaluation: they quantify regime dependent stability in a way that is independent of ensemble configuration and directly comparable across models.

Recognizing the pronounced differences in the predictability of Eastern and Western North Pacific (ENP and WNP) blocks naturally raises a related, but distinct, question:

do these regimes also differ in their intrinsic variability and energetic organization? The analogue framework established that ENP and WNP blocks possess distinct predictability horizons, yet it does not reveal how the internal dynamics and thermodynamic couplings governing these regimes differ. Building on this, the subsequent chapter investigates whether the variability characteristics of blocking, in terms of directional information flow among key dynamical and thermodynamic variables differ across regions and model hierarchies. To this end, the Liang–Kleeman information flow (LKIF) framework [Liang and Kleeman, 2005; Liang, 2014, 2021b] is applied to blocking events identified within the CMIP6 environment, with a focus on the MIROC6 model. This method, grounded in information theory, quantifies the probabilistic exchange of information among variables such as kinetic energy (KE), available potential energy (APE), and ground temperature (GT), offering a complementary view to deterministic predictability by characterizing how variability is dynamically organized. By tracing these directional couplings, the analysis examines whether the variability structure of blocking and its associated energy pathways differs between eastern and western regimes, thereby extending the idealized insights into a more realistic climate-model framework.

6.1.3 Can directional energetic couplings between kinetic energy, available potential energy, and ground temperature explain differences in blocking variability across regions and models?

To answer this question, we applied the Liang–Kleeman information flow (LKIF) framework to both an idealized quasi geostrophic land - atmosphere coupled model and the CMIP6 MIROC6 climate model, focusing on how energy pathways differ between blocked and non blocked states and between eastern and western North Pacific blocking events. By quantifying the causal directionality of interactions between the main Lorenz energy cycle (LEC) reservoirs and near surface thermal anomalies, we aimed to uncover the dynamical and thermodynamical processes underpinning the stability and variability of atmospheric blocking.

The results reveal a coherent set of signatures underscoring the role of directional energetics in shaping blocking variability. Across both modelling frameworks, a positive causal influence of kinetic energy (KE) on ground temperature (GT) emerged as a robust hallmark of blocking, reflecting how persistent, quasi-stationary flow anomalies modulate near-surface temperatures through advective and radiative processes. This finding aligns with established conceptual and observational studies [Pfahl and Wernli, 2012; Woollings et al., 2018; Seneviratne et al., 2010]. Beyond this shared surface impact, however, the coupling between KE and available potential energy (APE) exhibited pronounced regime- and model-dependence, highlighting how different dynamical contexts shape variability patterns.

In the QGS framework, blocked states displayed weakened mutual coupling between KE and APE, with APE acting as a stabilizing reservoir that limits KE variability, while KE exerted a strong positive influence on GT variability. Non-blocked states, by contrast, were characterized by reciprocal KE–APE interactions, where KE enhanced APE variability and

APE acted to constrain KE fluctuations. This distinction is consistent with the canonical Lorenz Energy Cycle (LEC) interpretation of blocked versus unblocked regimes [Lorenz, 1955; Holton and Hakim, 2013], indicating that blocking reorganizes energy pathways by suppressing baroclinic activity and strengthening surface coupling. Importantly, eastern and western blocks diverged in their variability structure: western blocks followed a more dominantly blocked pattern with reduced KE–APE exchange, whereas eastern blocks retained more active KE↔APE interactions and a notable GT→APE link, pointing to distinct energetic organization within the blocking regime.

When extended to the CMIP6 MIROC6 simulations, the LKIF analysis revealed a more nuanced structure consistent with the greater physical complexity of a fully coupled climate model. Differences between blocked and non-blocked composites were weaker than in the QGS framework, with diagnostic separation primarily associated with changes in APE self-influence and the presence or absence of GT→APE pathways. These patterns would probably reflect the modulation of variability by moist processes, boundary-layer dynamics, and ocean–atmosphere coupling in MIROC6. An east–west asymmetry again emerged, albeit with a different structure: eastern blocks resembled the canonical blocked regime, whereas western blocks exhibited stronger GT→KE and GT→APE pathways, emphasizing the enhanced role of surface and diabatic processes in shaping variability. Together, these findings demonstrate that while the specific expression of blocking energetics depends on model physics, the broader principle that directional couplings differ systematically between eastern and western blocks holds across model hierarchies.

These findings indicate that distinct variability asymmetries exist between blocking regimes, arising from differences in how kinetic energy (KE), available potential energy (APE), and ground temperature (GT) exchange information. Regimes with strong and reciprocal KE–APE coupling exhibit more balanced variability, consistent with efficient baroclinic adjustment, whereas those with weaker coupling and enhanced surface pathways display more pronounced and persistent surface impacts. Thus, directional information exchange among energetic reservoirs provides a dynamical basis for understanding how the internal variability structure of blocking differs across regions and regimes.

From a methodological standpoint, this chapter demonstrates the the potential of the Liang - Kleeman framework as a diagnostic tool in climate dynamics. Unlike correlations, which are symmetric and often misleading, information flow measures and capture the direction and sign of influence, allowing us to identify increase or decrease of different parameter variability in processes. By applying it consistently across idealized and complex models, we showed that causality analysis can reveal regime dependent mechanisms that are otherwise obscured in traditional energy budgets.

6.2 General Conclusions

In this thesis, we set out to advance the understanding of the variability and predictability of large scale flow regimes in the atmosphere, with particular focus on atmospheric blocking. By combining low-order, idealized frameworks with state-of-the-art CMIP6 cli-

mate simulations and novel analytical techniques, we systematically explored how blocking emerges, how its stability depends on location and morphology, and what dynamical and thermodynamical processes underlie its variability and predictability.

Across the chapters, several key findings emerge. First, in a reduced-order land–atmosphere coupled model, we showed that zonal regimes are more stable and predictable than blocking or transitional regimes, confirming long-standing theoretical expectations. Within blocking itself, predictability was found to depend strongly on geographical positioning: blocks forming downstream of topography exhibited higher stability than those upstream, emphasizing that proximity to orographic features exerts a critical influence on regime predictability.

Second, when these ideas were extended to comprehensive climate models—particularly MIROC6 within CMIP6, we identified a clear east - west asymmetry in North Pacific blocking. Eastern blocks were systematically less predictable than western blocks, a result that diverged from the idealized model probably reflecting the added complexity of moist processes, boundary layer feedbacks, and ocean - atmosphere coupling in GCMs. This demonstrated that while idealized models capture essential mechanisms, comprehensive models reorganize the sources and expression of predictability, underscoring the importance of cross-hierarchy analysis.

Third, to move beyond descriptive contrasts, we employed the Liang–Kleeman information flow (LKIF) framework to diagnose directional interactions among kinetic energy (KE), available potential energy (APE), and ground temperature (GT). This probabilistic, information-theoretic approach revealed that the structure and strength of energetic couplings differ systematically across blocking regimes and locations. In the QGS framework, western blocks displayed variability patterns resembling classical blocked states with weaker KE–APE coupling and stronger KE$\rightarrow$GT influence, whereas eastern blocks retained more dynamically active KE$\leftrightarrow$APE interactions and GT$\rightarrow$APE feedbacks. In MIROC6, eastern blocks resembled the canonical blocked energetics, while western blocks exhibited stronger surface-to-troposphere couplings, indicative of enhanced boundary-layer and diabatic control. Together, these results showed that variability asymmetries between blocking regimes can be traced to differences in directional energetics, offering a process-aware perspective that complements deterministic predictability diagnostics without implying direct equivalence.

By synthesizing these findings, this thesis makes two central contributions:

1. The predictability of blocking is not an intrinsic property of the regime alone but depends critically on its geographical context, morphology, and the representation of physical processes within the model.

2. Information-theoretic approaches, such as the Liang - Kleeman framework, provide a powerful and complementary lens for uncovering the dynamical and thermodynamical pathways that govern blocking variability.

6.3 Future Perspectives

A natural extension of this work lies in examining how the *East–West asymmetry in North Pacific blocking* shapes the occurrence, intensity, and persistence of extreme weather events. While this thesis has established clear differences in the intrinsic predictability and energetics of Eastern and Western blocks, their associated extremessuch as cold air outbreaks, heavy precipitation, heatwaves, and persistent dry spells,remain comparatively unexplored. Previous studies have demonstrated that blocking is a dominant driver of midlatitude extremes [Pfahl et al., 2015; Woollings et al., 2018], but the role of block location and morphology has received far less attention. Future research could combine high-resolution reanalysis datasets with event-based diagnostics to determine whether the dynamical and thermodynamical signatures identified here translate into systematic differences in the frequency, severity, and spatial structure of extremes downstream of each blocking subtype.

A second promising direction involves analysing the *life cycle evolution of extreme events conditioned on block location*, with particular focus on how synoptic-scale eddies, moisture transport pathways, and jet stream configurations interact differently with Eastern versus Western blocks. The results of this thesis suggest that Eastern blocks evolve in a more unstable dynamical environment, which may predispose them to rapid transitions that amplify extreme outcomes. Conversely, Western blocks exhibit more persistent structures that may modulate extremes differently, potentially favouring extended-duration events rather than sharp, high amplitude anomalies. Methodologies such as Lagrangian moisture tracking [Sprenger and Wernli, 2015], jet-regime composites [Barnes and Polvani, 2013], and extreme-value clustering analysis [Faranda et al., 2017] could be applied to uncover the physical pathways through which blocking structures modulate impact-relevant weather.

Another important research avenue concerns the *response of blocking asymmetry and associated extremes to climate change*. Projecting how warming, Arctic amplification, and changes in land ocean thermal contrasts reshape the occurrence and characteristics of Eastern and Western blocks remains an open challenge. Several studies have highlighted the sensitivity of blocking to background state changes [Dunn-Sigouin and Son, 2016; Strain et al., 2020; Davini and d'Andrea, 2020], yet the regional asymmetries revealed here have not been systematically explored in future climate scenarios. The model hierarchy adopted in this thesis spanning idealised QG systems to comprehensive CMIP6 simulations, provides a foundation on which targeted climate-change experiments can be built. Perturbation experiments or storyline approaches [Shepherd, 2019] could be used to evaluate whether the predictability gap between Eastern and Western blocks widens or narrows under different warming states, and how this affects subseasonal forecasting systems.

Finally, the methodological framework introduced in this thesis opens the possibility of analysing blocking related extremes using *causal and dynamical diagnostics*, including information transfer [Liang, 2014], regime stability metrics, and analogue based divergence measures. Extending these tools would allow future studies to quantify not only how

blocks evolve, but also how they *transmit* influence to the surrounding flow and thereby shape hazardous weather patterns. Combining dynamical-systems tools with event-based extremes analysis provides a pathway toward a more integrated understanding of blocking and its impacts, ultimately improving risk assessments and operational forecast guidance in midlatitude regions.

In conclusion, this thesis demonstrates that the variability and predictability of blocking are profoundly shaped by geographical context, model physics, and energetic coupling structures. By combining idealized models, comprehensive climate simulations, and advanced diagnostic tools, I believe that it helped in advancing both the theoretical and methodological understanding of blocking. The integration of analogue based finite time predictability metrics with causality based energetics, framed within topographic and dynamical constraints, yields a pathway to a better understanding of the blocking dynamics.

Appendix A

Appendix to Chapter 1

A.1 Gaussian Mixture Clustering (GMC)

Gaussian Mixture Clustering (GMC) is a prevalent unsupervised machine learning technique utilized for partitioning data points into clusters by modeling their underlying distribution.While the distribution of data points on the attractor may not align with a Gaussian distribution, the algorithm proceeds by approximating the distribution as Gaussian and subsequently identifies clusters based on this approximation. Each cluster is characterized by a Gaussian component, and the primary objective is to accurately estimate the parameters of these components to optimally describe the data. It comprises several steps.

- **Initialization:** GMC starts by randomly selecting K initial centers (means) μ_i for each cluster. Additionally, it initializes the covariance matrices Σ_i and the mixing coefficients π_i, which represent the probabilities of data points belonging to each cluster, where $i = 1, 2, ..., K$. The mixing coefficients must sum up to 1, and each must be between 0 and 1.
- **Expectation - Maximization (EM) Algorithm:** GMC employs the EM algorithm (Dempster et al., 1977) to iteratively estimate the parameters of the Gaussian components. The algorithm comprises two steps, the Expectation step (E-step) and the Maximization step (M-step).
  - **Expectation Step (E-Step):** During this step, the algorithm computes the responsibility ($\gamma_{i,j}$) of each data point x_j for each cluster i. The responsibility represents the probability that data point x_j belongs to cluster i, given the current parameters. This is calculated using Bayes' theorem:

$$\gamma_{i,j} = \frac{\pi_i \cdot \mathcal{N}(x_j; \mu_i, \Sigma_i)}{\sum_{k=1}^{K} \pi_k \cdot \mathcal{N}(x_j; \mu_i, \Sigma_i)} \tag{A.1}$$

    where $\gamma_{i,j}$ is the responsibility of cluster i for data point x_j, π_i is the mixing coefficient for cluster i. μ_i and Σ_i are the mean and covariance matrix for

cluster i, respectively. $\mathcal{N}(x_j; \mu_i, \Sigma_i)$ is the Gaussian probability density function for data point x_j with mean μ_i and covariance Σ_i.

– **Maximization Step (M-Step):** In this step, the algorithm updates the parameters of the Gaussian distributions (mean, covariance, and mixing coefficients) based on the responsibilities calculated in the E-step:

$$\text{New mean }, \mu_i = \frac{\sum_{j=1}^{N} \gamma_{i,j} \cdot x_j}{\sum_{j=1}^{N} \gamma_{i,j}} \tag{A.2}$$

$$\text{New covariance matrix }, \Sigma_i = \frac{\sum_{j=1}^{N} \gamma_{i,j} \cdot (x_j - \mu_i) \cdot (x_j - \mu_i)^T}{\sum_{j=1}^{N} \gamma_{i,j}} \tag{A.3}$$

$$\text{New mixing coefficient }, \pi_i = \frac{1}{N} \sum_{j=1}^{N} \gamma_{i,j} \tag{A.4}$$

where N is the number of data points. μ_i, Σ_i, and π_i are the updated mean, covariance matrix, and mixing coefficient for cluster i, respectively. $\gamma_{i,j}$ is the responsibility of cluster i for data point x_j (computed in the E-step). x_j is the j-th data point.

- **Convergence:** The E-step and M-step are repeated iteratively until the algorithm converges. Convergence happens when the change in the likelihood of the data between iterations becomes very small or when a predefined number of iterations is reached.
- **Cluster Assignment:** Once the algorithm converges, each data point is assigned to the cluster with the highest probability (highest responsibility).
- **Number of Clusters (K):** The number of clusters, K, is typically determined either by the user based on prior knowledge or by using techniques like the Bayesian Information Criterion (BIC) or cross-validation to find the optimal number of clusters.

In our study, we used cross-validation method and decided K as 3 for obtaining realistic results. Further explanation regarding the clustering algorithm can be obtained from recent literature on that subject [Hastie et al., 2009; Bishop and Nasrabadi, 2006; Dempster et al., 1977; Smyth et al., 1999].

A.2 Examples of blocking and zonal patterns evolved from the study

As previously indicated, employing the parameter configuration outlined in Table 3.1, we have successfully generated *earthlike* flow patterns. These flow regimes are visually

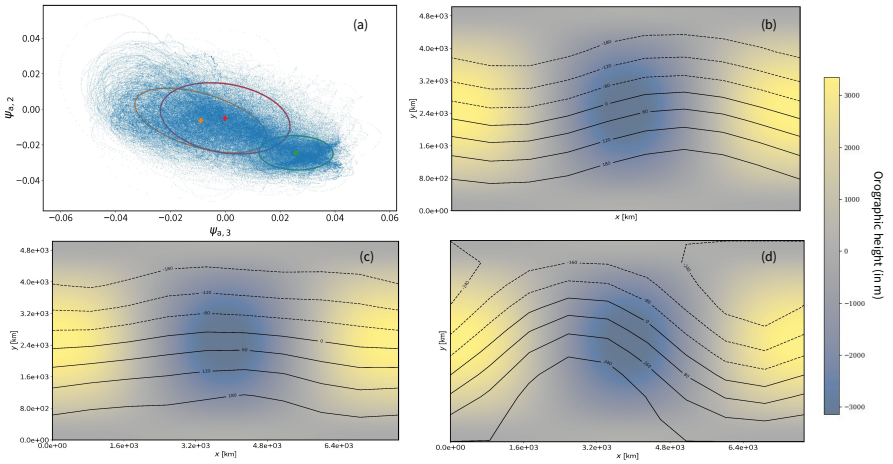


Figure A1: Phase space dynamics of the model projected on the ($\psi_{\mathrm{a},3}$, $\psi_{\mathrm{a},2}$)-plane is shown in panel (a) for $k_d = 0.065$. Gaussian mixture clusters covariance are represented with orange, green and red ellipsis. Orange cluster is associated with a zonal regime which can be identified by the geopotential height at 500 hPa in panel (b). Red and green clusters are respectively transition and blocking regimes attributed in panel (c) and (d), also at 500hPa geopotential height. The orographic profile of the domain is depicted in panels (b), (c) and (d).

represented in figures A2 and A1, corresponding to different values of the parameter k_d. Specifically, for lower values of k_d, we observe the coexistence of zonal, blocking, and transitional flow regimes, as depicted in figure A1. Conversely, when k_d assumes higher values, we observe the emergence of two blocking flow regimes along with a transition regime, as illustrated in figure A2.

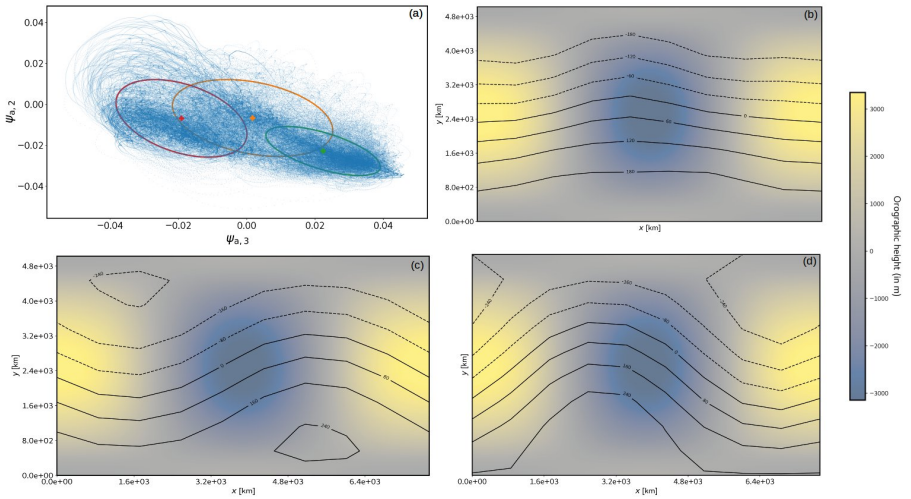


Figure A2: Same as Fig. A1 but for $k_d = 0.08$. Here the red (panel (c)) and green clusters (panel (d)) are both blocking regimes and the orange one (panel (b)) is a transition regime.

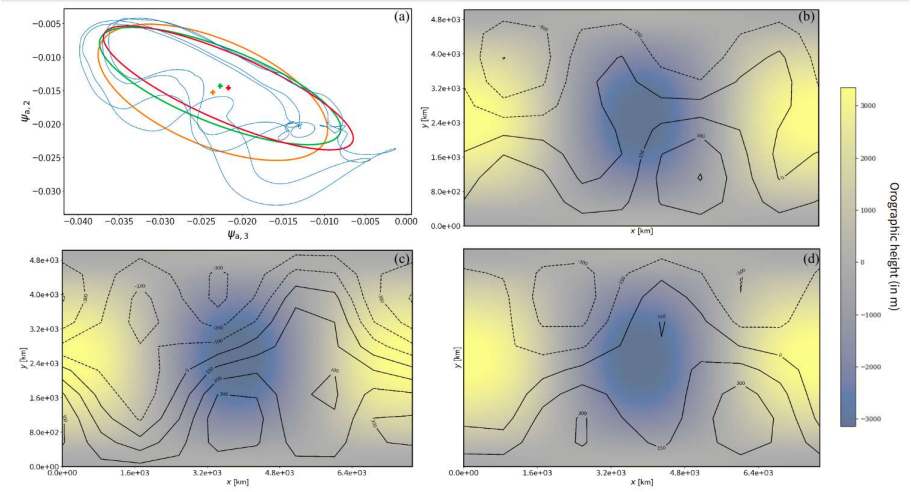


Figure A3: Same as Fig. A1 but for $k_d = 0.105$ where the system exhibits periodic behaviour results in to non identifiable flow regimes and indistinguishable clusters

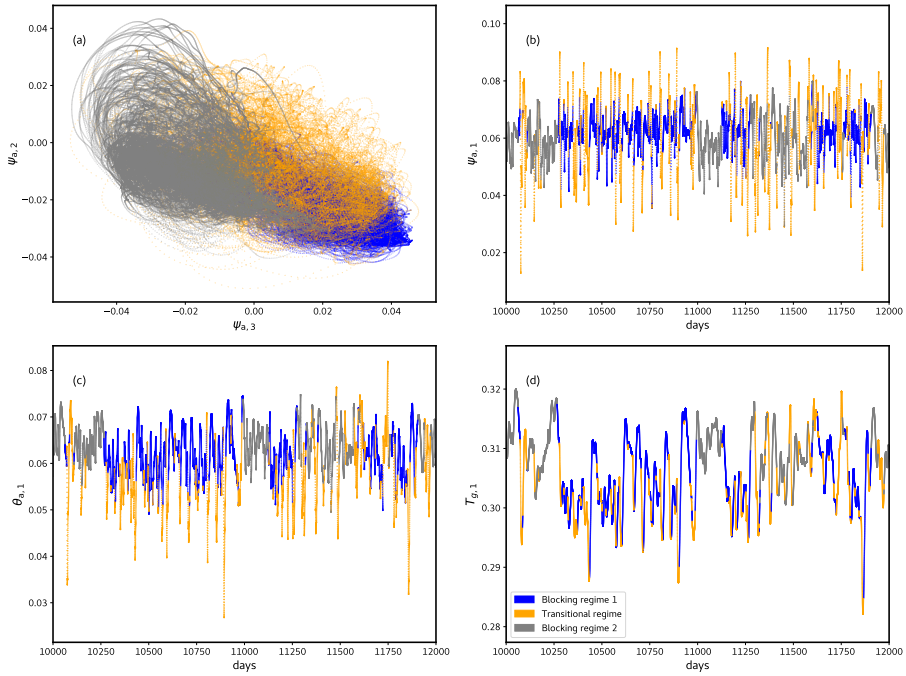


Figure A4: Phase space dynamics of the model projected on the ($\psi_{\mathrm{a},3}$, $\psi_{\mathrm{a},2}$)-plane is shown in panel (a) for $k_d = 0.08$. The figure illustrates the Gaussian mixture clustering results, where each data point is colored according to its corresponding cluster or flow regime. Panels (b), (c), and (d) depict the temporal evolution of barotropic ($\psi_{a,1}$) and baroclinic ($\theta_{a,1}$) atmospheric streamfunction, along with ground temperature ($T_{g,1}$) for $C_g = 300\ Wm^{-2}$ and $k_d = 0.08$, with colors corresponding to their respective clusters.

Appendix B

Appendix to Chapter 2

B.1 Predictability analysis ($\alpha = 0.20$)

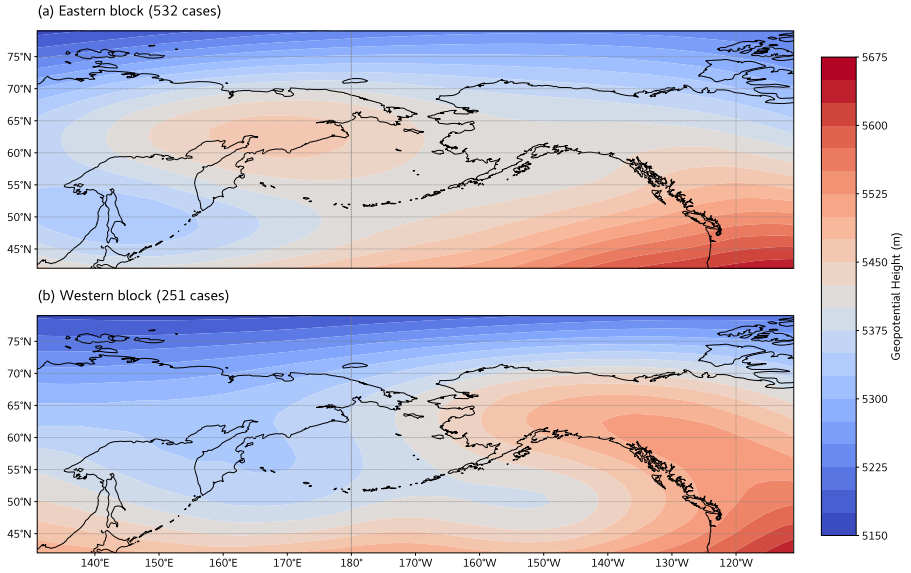


Figure A1: Same as fig 4.3 but with $\alpha = 0.20$. 532 Eastern blocks and 251 Western blocks are identified with this threshold

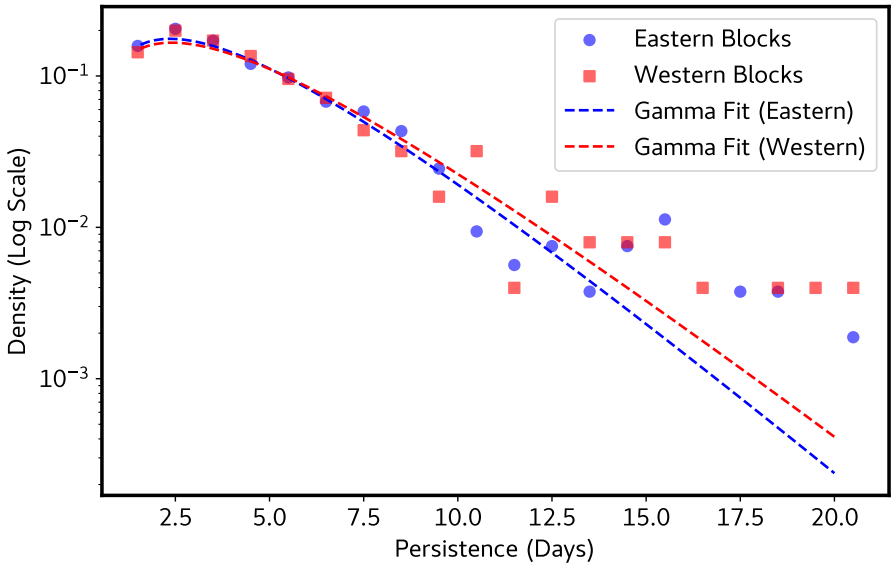


Figure A2: Same as Figure 4.4 but with $\alpha = 0.20$

B.2 Sensitivity test to analyze model dependence

This Supporting Information documents a targeted model dependence sensitivity analysis designed to test the robustness of the main paper's stability results for North Pacific blocking. We repeat the experiment across three CMIP6 historical simulations MIROC6 (in the main paper), IPSL-CM6A-LR, and MPI-ESM1 while holding the detection algorithm, spatial domains, verification metric, and threshold fixed ($\alpha = 0.25$).

As a model-dependence sensitivity check ($\alpha = 0.25$; first 50 ENP and 50 WNP cases per model), we repeated the analysis in three CMIP6 historical simulations: MIROC6, IPSL-CM6A-LR, and MPI-ESM1. MIROC6 reproduces a clear east–west contrast in early-time divergence (ENP $>$ WNP), with regime differences exceeding 95% bootstrap confidence intervals. IPSL-CM6A-LR shows only a weak ENP $>$ WNP signal; the differences are small and frequently lie within the confidence intervals. MPI-ESM1 exhibits a substantially larger reference - analogue initial separation for ENP (≈693 km), which inflates the raw mean error curves and complicates direct comparison, however after normalizing by the initial mismatch using the mean logarithmic growth rate, ENP still appears less predictable than WNP, consistent with MIROC6. These model-dependent outcomes align with Lohmann et al. [2024], who report smaller North Pacific blocking frequency biases for MIROC6 and larger regional biases for IPSL and MPI relative to reanalyses (ERA5, 20CR). We therefore present IPSL and MPI as targeted sensitivity checks to quantify model uncertainty without expanding the scope to a full multi model study.

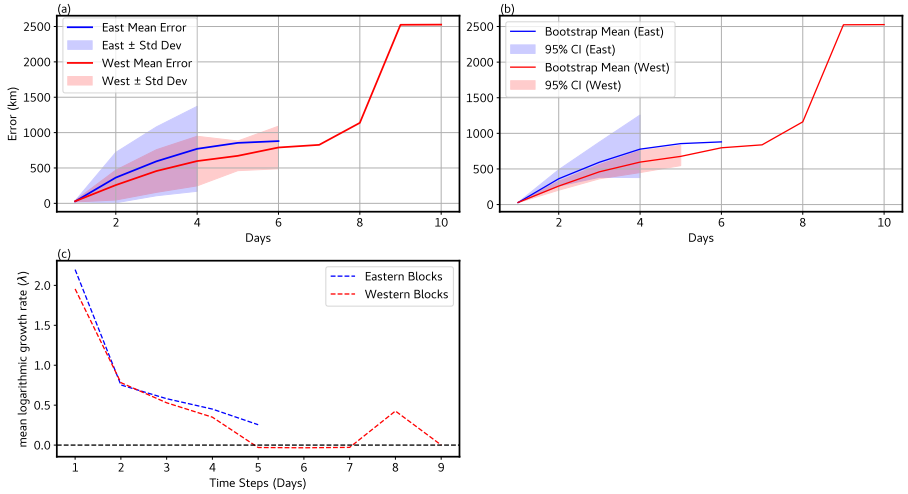


Figure A3: Same as Figure 4.6 but with $\alpha = 0.20$ considering first 50 reference-analogue pairs

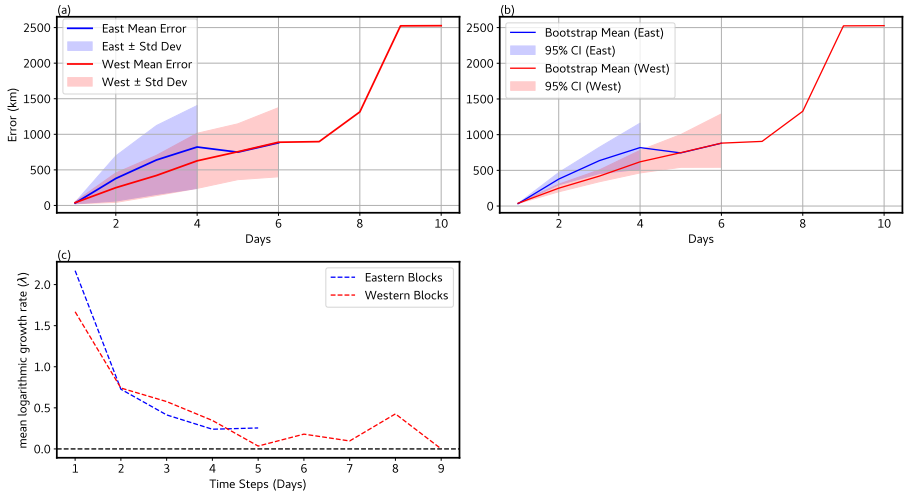


Figure A4: Same as Figure 4.6 but with $\alpha = 0.20$ considering first 75 reference-analogue pairs

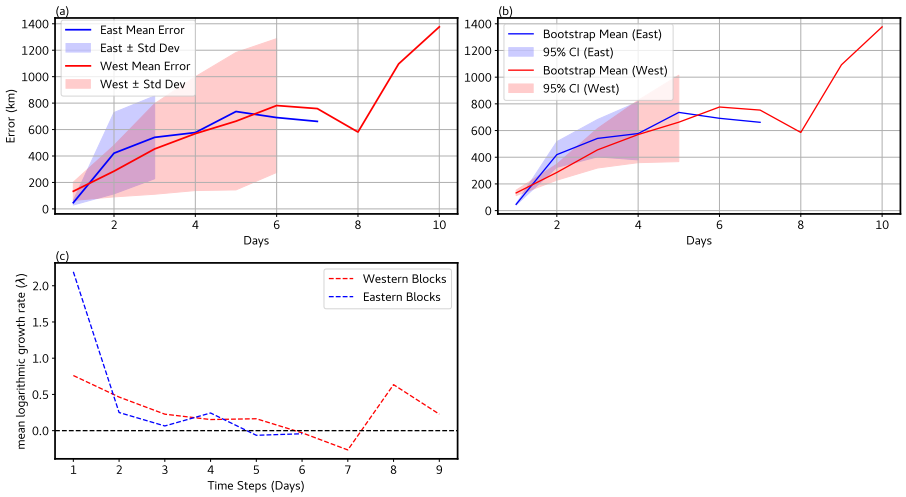


Figure A5: Evolution of error and logarithmic growth rate for ENP and WNP blocks in IPSL- CM6A-LR historical simulations, considering $\alpha = 0.25$ and the first 50 reference-analogue pairs with the smallest initial error. **(a)** Mean error growth over time for ENP and WNP blocks, with shaded regions representing the standard deviation. **(b)** Bootstrap mean error with 95% confidence intervals for both block types. Curves terminate where too few pairs remain because one or both blocks cease or splits.**(c)** Mean logarithmic growth rate over time, comparing the stability characteristics of ENP and WNP blocks.

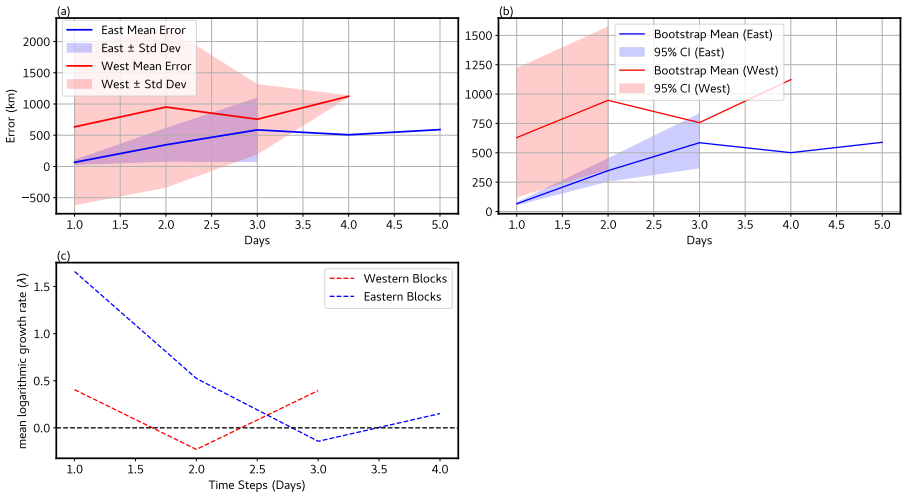


Figure A6: Evolution of error and logarithmic growth rate for Eastern and Western blocks in MPIM-ESM1 historical simulations same as figure A5

Appendix C

List of Publications Related to the Thesis

First author

Xavier, A. K., Doquier, D., and Vannitsem, S.: Linking Lorenz Energy Cycle Interactions and Ground Temperature to Blocking Variability in Idealized and Realistic CMIP6 Models, in preparation; to be submitted to *Geophys. Res. Lett.* (Chapter 5)

Xavier, A. K., Hamilton, O., Faranda, D., and Vannitsem, S.: Predictability of North Pacific blocking events: Analogue based analysis of historical MIROC6 simulations, *Q. J. R. Meteorol. Soc.*, https://doi.org/10.48550/arXiv.2504.17691, 202, under revision, (Chapter 4).

Xavier, A. K., Demaeyer, J., and Vannitsem, S.: Variability and predictability of a reduced-order land–atmosphere coupled model , *Earth Syst. Dynam.*, 15, 893–912, https://doi.org/10.5194/esd-15-893-2024, 2024 (Chapter 3).

Bibliography

Adewumi, A., Kagamba, J., and Alochukwu, A. (2016). Application of chaos theory in the prediction of motorised traffic flows on urban networks. *Mathematical Problems in Engineering*, 2016(1):5656734.

Andrews, D. G., Leovy, C. B., and Holton, J. R. (1987). *Middle atmosphere dynamics*, volume 40. Academic press.

Arbabi, H. and Mezić, I. (2017). Study of dynamics in post-transient flows using Koopman mode decomposition. *Physical Review Fluids*, 2(12):124402.

Athanasiadis, P. J., Bellucci, A., Hermanson, L., Scaife, A. A., MacLachlan, C., Arribas, A., Materia, S., Borrelli, A., and Gualdi, S. (2014). The representation of atmospheric blocking and the associated low-frequency variability in two seasonal prediction systems. *Journal of Climate*, 27(24):9082–9100.

Barnes, E. A. and Polvani, L. M. (2013). Jet stream variability and midlatitude weather extremes. *Nature Geoscience*, 6:489–495.

Barnes, E. A., Slingo, J., and Woollings, T. (2012). A methodology for the comparison of blocking climatologies across indices, models and climate scenarios. *Climate dynamics*, 38:2467–2481.

Barnston, A. G. and Livezey, R. E. (1987). Classification, seasonality and persistence of low-frequency atmospheric circulation patterns. *Monthly weather review*, 115(6):1083–1126.

Barriopedro, D., Fischer, E. M., Luterbacher, J., Trigo, R. M., and García-Herrera, R. (2011). The hot summer of 2010: redrawing the temperature record map of europe. *Science*, 332(6026):220–224.

Barriopedro, D., García-Herrera, R., Lupo, A. R., and Hernández, E. (2006). A climatology of northern hemisphere blocking. *Journal of climate*, 19(6):1042–1063.

Barriopedro, D., García-Herrera, R., Ordóñez, C., Miralles, D., and Salcedo-Sanz, S. (2023). Heat waves: Physical understanding and scientific challenges. *Reviews of Geophysics*, 61(2):e2022RG000780.

Barsugli, J. J. and Battisti, D. S. (1998). The basic effects of atmosphere–ocean thermal coupling on midlatitude variability. *Journal of the Atmospheric Sciences*, 55(4):477–493.

Benettin, G., Galgani, L., Giorgilli, A., and Strelcyn, J. (1980a). Lyapunov characteristic exponents for smooth dynamical systems and for hamiltonian systems; a method for computing all of them. part 1: Theory. *Meccanica*, 15:9–20.

Benettin, G., Galgani, L., Giorgilli, A., and Strelcyn, J.-M. (1980b). Lyapunov characteristic exponents for smooth dynamical systems and for hamiltonian systems; a method for computing all of them. part 1: Theory. *Meccanica*, 15:9–20.

Benzi, R., Hansen, A. R., and Sutera, A. (1984). On stochastic perturbation of simple blocking models. *Quarterly Journal of the Royal Meteorological Society*, 110(464):393–409.

Bishop, C. M. and Nasrabadi, N. M. (2006). *Pattern recognition and machine learning*. Springer.

Boffetta, G., Cencini, M., Falcioni, M., and Vulpiani, A. (2002). Predictability: a way to characterize complexity. *Physics reports*, 356(6):367–474.

Boffetta, G. and Musacchio, S. (2002). Predictability: a way to characterize complexity in dynamical systems. *Physics Reports*, 356(6):367–474. 10.1016/S0370-1573(01)00094-2.

Bohr, T., Jensen, M. H., Paladin, G., and Vulpiani, A. (1998). *Dynamical systems approach to turbulence*.

Branstator, G. (2002). Circumglobal teleconnections, the jet stream waveguide, and the north atlantic oscillation. *Journal of Climate*, 15(14):1893–1910. 10.1175/1520-0442(2002)015<1893:CTTJSW>2.0.CO;2.

Branstator, G. and Teng, H. (2017). Tropospheric waveguide teleconnections and their seasonality. *Journal of the Atmospheric Sciences*, 74(5):1513–1532. 10.1175/JAS-D-16-0305.1.

Breeden, M. L., Hoover, B. T., Newman, M., and Vimont, D. J. (2020). Optimal north pacific blocking precursors and their deterministic subseasonal evolution during boreal winter. *Monthly Weather Review*, 148(2):739–761.

Brunner, L., Schaller, N., Anstey, J., Sillmann, J., and Steiner, A. K. (2018). Dependence of present and future european temperature extremes on the location of atmospheric blocking. *Geophysical research letters*, 45(12):6311–6320.

Carrera, M., Higgins, R., and Kousky, V. (2004). Downstream weather impacts associated with atmospheric blocking over the northeast pacific. *Journal of Climate*, 17(24):4823–4839.

Cassou, C. (2008). Intraseasonal interaction between the madden–julian oscillation and the north atlantic oscillation. *Nature*, 455(7212):523–527.

Cehelsky, P. and Tung, K. K. (1987). Theories of multiple equilibria and weather regimes—a critical reexamination. part ii: Baroclinic two-layer models. *J. Atmos. Sci*, 44(21):3282–3303.

Charney, J. G. (1948). On the scale of atmospheric motions. In *The atmosphere—a challenge: The science of Jule Gregory Charney*, pages 251–265. Springer.

Charney, J. G. and DeVore, J. G. (1979). Multiple flow equilibria in the atmosphere and blocking. *Journal of the atmospheric sciences*, 36(7):1205–1216.

Charney, J. G. and Straus, D. M. (1980). Form-drag instability, multiple equilibria and propagating planetary waves in baroclinic, orographically forced, planetary wave systems. *Journal of Atmospheric Sciences*, 37(6):1157–1176.

Che, Z., Yao, Y., and Zhong, L. (2021). Wintertime sea surface temperature front around the kuroshio extension and its impact on north pacific blocking. *International Journal of Climatology*, 41(3):1905–1926.

Crommelin, D. T. (2004). Observed nondiffusive dynamics in large-scale atmospheric flow. *Journal of the atmospheric sciences*, 61(19):2384–2396.

d'Andrea, F., Provenzale, A., Vautard, R., and De Noblet-Decoudré, N. (2006). Hot and cool summers: Multiple equilibria of the continental water cycle. *Geophysical Research Letters*, 33(24).

Davini, P., Cagnazzo, C., Gualdi, S., and Navarra, A. (2012). Bidimensional diagnostics, variability, and trends of northern hemisphere blocking. *Journal of Climate*, 25(19):6496–6509.

Davini, P. and D'Andrea, F. (2020). From cmip3 to cmip6: Northern hemisphere atmospheric blocking in current and future climate models. *Journal of Climate*, 33(10):6923–6942. 10.1175/JCLI-D-19-0862.1.

Davini, P. and D'Andrea, F. (2016). Northern hemisphere atmospheric blocking representation in global climate models: twenty years of improvements? *Journal of Climate*, 29(24):8823–8840.

Davini, P. and D'Andrea, F. (2017). Climate model biases in blocking and associated moisture processes. *Climate Dynamics*, 48:3157–3173.

Davini, P. and d'Andrea, F. (2020). From cmip3 to cmip6: Northern hemisphere atmospheric blocking simulation in present and future climate. *Journal of Climate*, 33(23):10021–10038.

De Cruz, L., Demaeyer, J., and Vannitsem, S. (2016). The modular arbitrary-order ocean-atmosphere model: Maooam v1. 0. *Geoscientific Model Development*, 9(8):2793–2808.

De Luca, P., Jiménez-Esteve, B., Degenhardt, L., Schemm, S., and Pfahl, S. (2024). Enhanced blocking frequencies in very-high resolution idealized climate model simulations. *Geophysical Research Letters*, 51(22):e2024GL111016.

Demaeyer, J., De Cruz, L., and Vannitsem, S. (2020). qgs: A flexible python framework of reduced-order multiscale climate models. *Journal of Open Source Software*, 5(56):2597.

Demaeyer, J. and Hamilton, O. (2025). auto-auto: A python layer for automatically running the auto-07p continuation software. *Journal of Open Source Software*, 10(113):8079. 10.21105/joss.08079.

Dempster, A. P., Laird, N. M., and Rubin, D. B. (1977). Maximum likelihood from incomplete data via the em algorithm. *Journal of the royal statistical society: series B (methodological)*, 39(1):1–22.

Diao, Y., Li, J., and Luo, D. (2006). A new blocking index and its application: Blocking action in the northern hemisphere. *Journal of Climate*, 19(19):4819–4839.

Dieci, L. and Van Vleck, E. S. (2002). Lyapunov spectral intervals: theory and computation. *SIAM Journal on Numerical Analysis*, 40(2):516–542.

Dijkstra, H. A. (2013). *Nonlinear climate dynamics*. Cambridge University Press.

Docquier, D., Massonnet, F., Ragone, F., Sticker, A., Fichefet, T., and Vannitsem, S. (2024). Drivers of summer arctic sea-ice extent at interannual time scale in cmip6 large ensembles revealed by information flow. *Scientific Reports*, 14(1):24236.

Dole, R. M. and Gordon, N. D. (1983). Persistent anomalies of the extratropical northern hemisphere wintertime circulation: Geographical distribution and regional persistence characteristics. *Monthly Weather Review*, 111(8):1567–1586.

Dörr, J., Årthun, M., Docquier, D., Li, C., and Eldevik, T. (2024). Causal links between sea-ice variability in the barents-kara seas and oceanic and atmospheric drivers. *Geophysical Research Letters*, 51(7):e2024GL108195.

Dorrington, J. and Palmer, T. (2023). On the interaction of stochastic forcing and regime dynamics. *Nonlinear Processes in Geophysics*, 30(1):49–62.

Drouard, M., Kornhuber, K., and Woollings, T. (2019). Disentangling dynamic contributions to summer 2018 anomalous weather over europe. *Geophysical Research Letters*, 46(21):12537–12546.

Drouard, M. and Woollings, T. (2018). Contrasting mechanisms of summer blocking over western eurasia. *Geophysical Research Letters*, 45(21):12–040.

Dunn-Sigouin, E. and Son, S.-W. (2016). Evaluating extremes in blocking and storm tracks as indicators of climate change. *Climate Dynamics*, 47:3271–3285.

Eckmann, J.-P. and Ruelle, D. (1985a). Ergodic theory of chaos and strange attractors. *Reviews of Modern Physics*, 57(3):617–656. 10.1103/RevModPhys.57.617.

Eckmann, J.-P. and Ruelle, D. (1985b). Ergodic theory of chaos and strange attractors. *Reviews of modern physics*, 57(3):617.

Egger, J. (1981). Stochastically driven large-scale circulations with multiple equilibria. *Journal of Atmospheric Sciences*, 38(12):2606–2618.

ERCOT (2021). Review of february 2021 extreme cold weather event – texas energy crisis report. Technical report, Electric Reliability Council of Texas, Austin, TX. Available at: `https://www.ercot.com/files/docs/2021/03/05/February_2021_Weather_Event_Report.pdf`.

Eyring, V., Bony, S., Meehl, G. A., Senior, C. A., Stevens, B., Stouffer, R. J., and Taylor, K. E. (2016). Overview of the coupled model intercomparison project phase 6 (cmip6) experimental design and organization. *Geoscientific Model Development*, 9(5):1937–1958. 10.5194/gmd-9-1937-2016.

Faranda, D., Masato, G., Moloney, N., Sato, Y., Daviaud, F., Dubrulle, B., and Yiou, P. (2016). The switching between zonal and blocked mid-latitude atmospheric circulation: a dynamical system perspective. *Climate Dynamics*, 47:1587–1599.

Faranda, D., Messori, G., Jezequel, A., Vrac, M., and Yiou, P. (2023). Atmospheric circulation compounds anthropogenic warming and impacts of climate extremes in europe. *Proceedings of the National Academy of Sciences*, 120(13):e2214525120.

Faranda, D., Messori, G., and Yiou, P. (2017). Dynamical proxies of north atlantic predictability and extremes. *Scientific reports*, 7(1):41278.

Feldstein, S. B. and Dayan, U. (2008). Circumglobal teleconnections and wave packets associated with israeli winter precipitation. *Quarterly Journal of the Royal Meteorological Society*, 134(630):455–467. 10.1002/qj.225.

Ferranti, L., Corti, S., and Janousek, M. (2015). Flow-dependent verification of the ecmwf ensemble over the euro-atlantic sector. *Quarterly Journal of the Royal Meteorological Society*, 141(688):916–924.

Frederiksen, J. S., Collier, M. A., and Watkins, A. B. (2004). Ensemble prediction of blocking regime transitions. *Tellus A: Dynamic Meteorology and Oceanography*, 56(5):485–500.

Ghil, M. (1987). Dynamics, statistics and predictability of planetary flow regimes. In *Irreversible Phenomena and Dynamical Systems Analysis in Geosciences*, pages 241–283. Springer.

Ghil, M. (2008). Climate stability for a broader public. In von Storch, H. and Payne, T. J., editors, *Hamburg 50 Years: Change, Adaptation and the Self*, pages 31–63. Elsevier, Oxford. 10.1016/B978-0-08-045261-0.00003-1.

Ghil, M. and Robertson, A. W. (2002a). "waves" vs."particles" in the atmosphere's phase space: A pathway to long-range forecasting? *Proceedings of the National Academy of Sciences*, 99(suppl_1):2493–2500.

Ghil, M. and Robertson, A. W. (2002b). "waves" vs."particles" in the atmosphere's phase space: A pathway to long-range forecasting? *Proceedings of the National Academy of Sciences*, 99(suppl_1):2493–2500.

Gill, A. E. (1982). *Atmosphere—ocean dynamics*. Elsevier.

Giorgetta, M. A., Jungclaus, J., Reick, C. H., Legutke, S., Bader, J., Böttinger, M., and et al. (2013). Climate and carbon cycle changes from 1850 to 2100 in mpi-esm simulations for the coupled model intercomparison project phase 5. *Journal of Advances in Modeling Earth Systems*, 5(3):572–597. 10.1002/jame.20038.

Golub, G. H. and Van Loan, C. F. (2013). *Matrix Computations*. Johns Hopkins University Press, Baltimore, 4th edition.

Haiden, T., Janousek, M., Vitart, F., Ferranti, L., Prates, F., and Richardson, D. (2019). The ecmwf integrated forecasting system: Model description. Technical Memorandum 859, ECMWF. 10.21957/ifde1v8p.

Hamill, T. M. and Kiladis, G. N. (2014). Skill of the mjo and northern hemisphere blocking in gefs medium-range reforecasts. *Monthly Weather Review*, 142(2):868–885.

Harnik, N., Messori, G., Caballero, R., and Feldstein, S. B. (2016). The circumglobal north american wave pattern and its relation to cold events in eastern north america. *Geophysical Research Letters*, 43(22):11,458–11,466. 10.1002/2016GL070760.

Hastie, T., Tibshirani, R., Friedman, J. H., and Friedman, J. H. (2009). *The elements of statistical learning: data mining, inference, and prediction*, volume 2. Springer.

Held, I. M. (2005). The gap between simulation and understanding in climate modeling. *Bulletin of the American Meteorological Society*, 86(11):1609–1614.

Held, I. M. and Ting, M. (1990). Orographic versus thermal forcing of stationary waves: The importance of the mean low-level wind. *Journal of Atmospheric Sciences*, 47(4):495–500.

Henderson, S. A. and Maloney, E. D. (2018). The impact of the madden–julian oscillation on high-latitude winter blocking during el niño–southern oscillation events. *Journal of Climate*, 31(13):5293–5318.

Henderson, S. A., Maloney, E. D., and Barnes, E. A. (2016). The influence of the madden–julian oscillation on northern hemisphere winter blocking. *Journal of Climate*, 29(12):4597–4616.

Hersbach, H., Bell, B., Berrisford, P., Hirahara, S., Horányi, A., Muñoz-Sabater, J., Nicolas, J., Peubey, C., Radu, R., Schepers, D., Simmons, A., Soci, C., Abdalla, S., Abellan, X., Balsamo, G., Bechtold, P., Biavati, G., Bidlot, J.-R., Bonavita, M., De Chiara, G., Dahlgren, P., Dee, D., Diamantakis, M., Dragani, R., Flemming, J., Forbes, R., Fuentes, M., Geer, A., Haimberger, L., Healy, S., Hogan, R. J., Hólm, E., Janisková, M., Keeley, S., Laloyaux, P., Lopez, P., Lupu, C., Radnoti, G., Rosnay, P., Rozum, I., Vamborg, F., Villaume, S., and Thépaut, J.-N. (2020). The era5 global reanalysis. *Quarterly Journal of the Royal Meteorological Society*, 146(730):1999–2049. 10.1002/qj.3803.

Holton, J. and Hakim, G. (2012). An introduction to dynamic meteorology. 245 (vol. 88).

Holton, J. R. and Hakim, G. J. (2013). *An introduction to dynamic meteorology*, volume 88. Academic press.

Hourdin, F., Grandpeix, J.-Y., Rio, C., Bony, S., Jam, A., Cheruy, F., Rochetin, N., Fairhead, L., Idelkadi, A., Musat, I., et al. (2013). Lmdz5b: The atmospheric component of the ipsl climate model with revisited parameterizations for clouds and convection. *Climate Dynamics*, 40:2193–2222.

Hurrell, J. W. (1995). Decadal trends in the north atlantic oscillation: Regional temperatures and precipitation. *Science*, 269(5224):676–679.

Hurrell, J. W., Holland, M. M., Gent, P. R., Ghan, S., Kay, J. E., Kushner, P. J., Lamarque, J.-F., Large, W. G., Lawrence, D., Lindsay, K., Lipscomb, W. H., Long, M. C., Mahowald, N., Marsh, D. R., Neale, R. B., Rasch, P. J., Vavrus, S., Vertenstein, M., Bader, D., Collins, W. D., Hack, J. J., Kiehl, J., and Marshall, S. (2013). The community earth system model: A framework for collaborative research. *Bulletin of the American Meteorological Society*, 94(9):1339–1360. 10.1175/BAMS-D-12-00121.1.

Hwang, J., Martineau, P., Son, S.-W., Miyasaka, T., and Nakamura, H. (2020). The role of transient eddies in north pacific blocking formation and its seasonality. *Journal of the Atmospheric Sciences*, 77(7):2453–2470.

Kalnay, E. (2003). *Atmospheric modeling, data assimilation and predictability*. Cambridge university press.

Kautz, L.-A., Martius, O., Pfahl, S., Pinto, J. G., Ramos, A. M., Sousa, P. M., and Woollings, T. (2021). Atmospheric blocking and weather extremes over the euro-atlantic sector–a review. *Weather and Climate Dynamics Discussions*, 2021:1–43.

Kautz, L.-A., Martius, O., Pfahl, S., Pinto, J. G., Ramos, A. M., Sousa, P. M., and Woollings, T. (2022). Atmospheric blocking and weather extremes over the euro-atlantic sector–a review. *Weather and climate dynamics*, 3(1):305–336.

Kim, S.-H. and Kim, B.-M. (2019). In search of winter blocking in the western north pacific ocean. *Geophysical Research Letters*, 46(15):9271–9280.

Kornhuber, K., Coumou, D., Vogel, E., Lesk, C., Donges, J. F., Lehmann, J., and Horton, R. M. (2020). Amplified rossby waves enhance risk of concurrent heatwaves in major breadbasket regions. *Nature Climate Change*, 10(1):48–53.

Kucharski, F., Molteni, F., King, M. P., Farneti, R., Kang, I.-S., and Feudale, L. (2013). On the need of intermediate complexity general circulation models: A "speedy" example. *Bulletin of the American Meteorological Society*, 94(1):25–30.

Kuptsov, P. V. and Parlitz, U. (2012). Theory and computation of covariant lyapunov vectors. *Journal of nonlinear science*, 22:727–762.

Kwasniok, F. (2019). Fluctuations of finite-time lyapunov exponents in an intermediate-complexity atmospheric model: a multivariate and large-deviation perspective. *Nonlinear Processes in Geophysics*, 26(3):195–209.

Lau, W. K. and Kim, K.-M. (2012). The 2010 pakistan flood and russian heat wave: Teleconnection of hydrometeorological extremes. *Journal of Hydrometeorology*, 13(1):392–403.

Leathers, D. J., Yarnal, B., and Palecki, M. A. (1991). The pacific/north american teleconnection pattern and united states climate. part i: Regional temperature and precipitation associations. *Journal of Climate*, 4(5):517–528.

Legras, B. and Ghil, M. (1985). Persistent anomalies, blocking and variations in atmospheric predictability. *Journal of Atmospheric Sciences*, 42(5):433–471.

Legras, B. and Vautard, R. (1996). A guide to liapunov vectors. In *Proceedings 1995 ECMWF seminar on predictability*, volume 1, pages 143–156.

Leutbecher, M. and Palmer, T. N. (2008). Ensemble forecasting. *Journal of computational physics*, 227(7):3515–3539.

Li, D., He, Y., Huang, J., Bi, L., and Ding, L. (2018). Multiple equilibria in a land–atmosphere coupled system. *Journal of Meteorological Research*, 32(6):950–973.

Liang, X. S. (2008). Information flow within stochastic dynamical systems. *Physical Review E*, 78(3):031113.

Liang, X. S. (2014). Unraveling the cause-effect relation between time series. *Physical Review E*, 90(5):052150.

Liang, X. S. (2016). Information flow and causality as rigorous notions ab initio. *Physical Review E*, 94(5):052201.

Liang, X. S. (2021a). Normalized multivariate time series causality analysis and causal graph reconstruction. *Entropy*, 23(6):679. 10.3390/e23060679.

Liang, X. S. (2021b). Normalized multivariate time series causality analysis and causal graph reconstruction. *Entropy*, 23(6):679.

Liang, X. S. and Kleeman, R. (2005). Information flow within stochastic dynamical systems. *Physical Review Letters*, 95(24):244101.

Liu, J. S. (1994a). The collapsed gibbs sampler in bayesian computations with applications to a gene regulation problem. *Journal of the American Statistical Association*, 89(427):958–966.

Liu, Q. (1994b). On the definition and persistence of blocking. *Tellus A*, 46(3):286–298.

Lohmann, G. and *et al.* (2024). Northern hemisphere atmospheric blocking in cmip6 climate projections using a hybrid index. *Journal of Climate*. Discusses projected changes in blocking frequency across Northern Hemisphere seasons.

Lohmann, R., Purr, C., and Ahrens, B. (2024). Northern hemisphere atmospheric blocking in cmip6 climate projections using a hybrid index. *Journal of Climate*, 37(24):6605–6625.

Lorenz, E. N. (1955). Available potential energy and the maintenance of the general circulation. *Tellus*, 7(2):157–167.

Lorenz, E. N. (1960). Maximum simplification of the dynamic equations. *Tellus*, 12(3):243–254.

Lorenz, E. N. (1962). Simplified dynamic equations applied to the rotating-basin experiments. *Journal of the Atmospheric Sciences*, 19(1):39–51.

Lorenz, E. N. (1963a). Deterministic nonperiodic flow. *Journal of atmospheric sciences*, 20(2):130–141.

Lorenz, E. N. (1963b). The mechanics of vacillation. *Journal of Atmospheric Sciences*, 20(5):448–465.

Lorenz, E. N. (1969). Atmospheric predictability as revealed by naturally occurring analogues. *Journal of Atmospheric Sciences*, 26(4):636–646.

Lucarini, V., Faranda, D., de Freitas, J. M. M., Holland, M., Kuna, T., Nicol, M., Todd, M., Vaienti, S., et al. (2016). *Extremes and recurrence in dynamical systems*. John Wiley & Sons.

Lucarini, V. and Gritsun, A. (2020). A new mathematical framework for atmospheric blocking events. *Climate Dynamics*, 54(1):575–598.

Luo, D. (2005). A barotropic envelope rossby soliton model for block–eddy interaction. part i: Effect of topography. *Journal of the Atmospheric Sciences*, 62(1):5–21.

Lupo, A. R. and Bosart, L. F. (1999). An analysis of a relatively rare case of continental blocking. *Quarterly Journal of the Royal Meteorological Society*, 125(553):107–138.

Lupo, A. R., Jensen, A. D., Mokhov, I. I., Timazhev, A. V., Eichler, T., and Efe, B. (2019). Changes in global blocking character in recent decades. *Atmosphere*, 10(2):92.

Lupo, A. R. and Smith, P. J. (1995). Planetary and synoptic-scale interactions during the life cycle of a mid-latitude blocking anticyclone over the north atlantic. *Tellus A*, 47(5):575–596.

Marques, C. A., Rocha, A., Corte-Real, J., Castanheira, J. M., Ferreira, J., and Melo-Goncalves, P. (2009). Global atmospheric energetics from ncep-reanalysis 2 and ecmwf-era40 reanalysis. *international Journal of Climatology*, 29(2):159.

Marshall, J. and Molteni, F. (1993). Toward a dynamical understanding of planetary-scale flow regimes. *Journal of the atmospheric sciences*, 50(12):1792–1818.

Martius, O., Pfahl, S., and Chevalier, C. (2013). The role of atmospheric rivers and warm conveyor belts in the formation of blocking. *Geophysical Research Letters*, 40:5485–5490.

Masato, G., Hoskins, B., and Woollings, T. J. (2012). Wave-breaking characteristics of midlatitude blocking. *Quarterly Journal of the Royal Meteorological Society*, 138(666):1285–1296.

Matsueda, M. (2009). Blocking predictability in operational medium-range ensemble forecasts. *Sola*, 5:113–116.

Matsueda, M. (2011). Predictability of euro-russian blocking in summer of 2010. *Geophysical Research Letters*, 38(6).

Matsueda, M. and Palmer, T. (2018). Estimates of flow-dependent predictability of wintertime euro-atlantic weather regimes in medium-range forecasts. *Quarterly Journal of the Royal Meteorological Society*, 144(713):1012–1027.

Merryfield, W. J., Baehr, J., Batté, L., Becker, E. J., Butler, A. H., Coelho, C. A., Danabasoglu, G., Dirmeyer, P. A., Doblas-Reyes, F. J., Domeisen, D. I., et al. (2020a). Current and emerging developments in subseasonal to decadal prediction. *Bulletin of the American Meteorological Society*, 101(6):E869–E896.

Merryfield, W. J., Baehr, J., Batté, L., Becker, E. J., Butler, A. H., Coelho, C. A. S., Danabasoglu, G., Doblas-Reyes, F. J., Domeisen, D. I. V., Ferranti, L., Ilyina, T., Kumar, A., Müller, W. A., Rixen, M., Robertson, A. W., Smith, D., Takaya, Y., Tuma, M., Vitart, F., and White, C. J. (2020b). Current and emerging developments in subseasonal to decadal prediction. *Bulletin of the American Meteorological Society*, 101(6):E869–E896. 10.1175/BAMS-D-19-0037.1.

Meurer, A., Smith, C. P., Paprocki, M., Čertík, O., Kirpichev, S. B., Rocklin, M., Kumar, A., Ivanov, S., Moore, J. K., Singh, S., et al. (2017). Sympy: symbolic computing in python. *PeerJ Computer Science*, 3:e103.

Mezić, I. (2020). Spectrum of the Koopman operator, spectral expansions in functional spaces, and state-space geometry. *Journal of Nonlinear Science*, 30(5):2091–2145.

Miralles, D. G., Gentine, P., Seneviratne, S. I., and Teuling, A. J. (2019). Land–atmospheric feedbacks during droughts and heatwaves: state of the science and current challenges. *Annals of the New York Academy of Sciences*, 1436(1):19–35.

Miralles, D. G., Teuling, A. J., Van Heerwaarden, C. C., and Vilà-Guerau de Arellano, J. (2014). Mega-heatwave temperatures due to combined soil desiccation and atmospheric heat accumulation. *Nature geoscience*, 7(5):345–349.

Monin, A. S. (1986). An introduction to the theory of climate. *Hingham, MA USA: Sold and distributed in the USA and Canada by Kluwer Academic Publishers, c1986*, 261.

Müller, W. A. and Roeckner, E. (2015). Diabatic heating and blocking maintenance in the euro-atlantic sector. *Climate Dynamics*, 45:1715–1731.

Nakamura, N. and Huang, C. S. (2018). Atmospheric blocking as a traffic jam in the jet stream. *Science*, 361(6397):42–47.

Neal, E., Huang, C. S., and Nakamura, N. (2022). The 2021 pacific northwest heat wave and associated blocking: Meteorology and the role of an upstream cyclone as a diabatic source of wave activity. *Geophysical Research Letters*, 49(8):e2021GL097699.

Nicolis, C. and Nicolis, G. (1981). Stochastic aspects of climatic transitions–additive fluctuations. *Tellus*, 33(3):225–234.

Nicolis, C., Vannitsem, S., and Royer, J.-F. (1995). Short-range predictability of the atmosphere: Mechanisms for superexponential error growth. *Quarterly Journal of the Royal Meteorological Society*, 121(523):705–722.

Nicolis, G. and Nicolis, C. (1991). Nonlinear dynamic systems in the geosciences. *Bulletin (Kansas Geological Survey)*, pages 33–42.

Nicolis, G. and Nicolis, C. (2012). *Foundations of complex systems: emergence, information and predicition*. World Scientific.

Nie, J. and Sobel, A. H. (2021). Moisture processes and the predictability of atmospheric blocking. *Journal of the Atmospheric Sciences*, 78:1743–1759.

Nitsche, M. and Krasny, R. (1994). A numerical study of vortex ring formation at the edge of a circular tube. *Journal of Fluid Mechanics*, 276:139–161.

North, G. R., Cahalan, R. F., and Coakley Jr, J. A. (1981). Energy balance climate models. *Reviews of Geophysics*, 19(1):91–121.

Oort, A. H. and Peixóto, J. P. (1983). Global angular momentum and energy balance requirements from observations. In *Advances in geophysics*, volume 25, pages 355–490. Elsevier.

O'Reilly, C. H. and Czaja, A. (2015). The response of the pacific storm track and atmospheric circulation to kuroshio extension variability. *Quarterly Journal of the Royal Meteorological Society*, 141(686):52–66.

Oseledec, V. I. (1968). A multiplicative ergodic theorem, lyapunov characteristic numbers for dynamical systems. *Transactions of the Moscow Mathematical Society*, 19:197–231.

Ott, E. (2002). *Chaos in dynamical systems*. Cambridge university press.

Palmer, T., Doblas-Reyes, F., Weisheimer, A., and Rodwell, M. (2008). Toward seamless prediction: Calibration of climate change projections using seasonal forecasts. *Bulletin of the American Meteorological Society*, 89(4):459–470.

Palmer, T. N. (1993). Extended-range atmospheric prediction and the lorenz model. *Bulletin of the American Meteorological Society*, 74(1):49–66.

Park, M., Johnson, N. C., Hwang, J., and Jia, L. (2024). A hybrid approach for skillful multiseasonal prediction of winter north pacific blocking. *npj Climate and Atmospheric Science*, 7(1):227.

Parker, T. S. and Chua, L. (2012). *Practical numerical algorithms for chaotic systems*. Springer Science & Business Media.

Peixoto, J. P. and Oort, A. H. (1992). Physics of climate.

Pelly, J. L. and Hoskins, B. J. (2003). A new perspective on blocking. *Journal of the atmospheric sciences*, 60(5):743–755.

Pfahl, S., Schwierz, C., Croci-Maspoli, M., Grams, C. M., and Wernli, H. (2015). Importance of latent heat release in ascending air streams for atmospheric blocking. *Nature Geoscience*, 8(8):610–614.

Pfahl, S. and Wernli, H. (2012). Quantifying the relevance of atmospheric blocking for co-located temperature extremes in the northern hemisphere on (sub-) daily time scales. *Geophysical Research Letters*, 39(12).

Pfahl, S. and Wernli, H. (2014). Importance of latent heat release in atmospheric blocking and rossby wave breaking. *Journal of the Atmospheric Sciences*, 71:3069–3087.

Phillips, N. A. (1951). A simple three-dimensional model for the study of large-scale extratropical flow patterns. *Journal of Atmospheric Sciences*, 8(6):381–394.

Plaut, G. and Vautard, R. (1994). Spells of low-frequency oscillations and weather regimes in the northern hemisphere. *Journal of Atmospheric Sciences*, 51(2):210–236.

Qiu, B., Chen, S., and Schneider, N. (2017). Dynamical links between the decadal variability of the oyashio and kuroshio extensions. *Journal of Climate*, 30(23):9591–9605.

Reinhold, B. and Pierrehumbert, R. (1985). Corrections to ''dynamics of weather regimes: Quasi-stationary waves and blocking.''. *Mon. Wea. Rev*, 113:2055–2056.

Reinhold, B. B. and Pierrehumbert, R. T. (1982). Dynamics of weather regimes: Quasi-stationary waves and blocking. *Monthly Weather Review*, 110(9):1105–1145.

Rex, D. F. (1950). Blocking action in the middle troposphere and its effect upon regional climate. *Tellus*, 2(4):275–301.

Rodwell, M. J., Magnusson, L., Bauer, P., Bechtold, P., Bonavita, M., Cardinali, C., Diamantakis, M., Earnshaw, P., Garcia-Mendez, A., Isaksen, L., et al. (2013). Characteristics of occasional poor medium-range weather forecasts for europe. *Bulletin of the American Meteorological Society*, 94(9):1393–1405.

Romeiras, F. J., Grebogi, C., and Ott, E. (1990). Multifractal properties of snapshot attractors of random maps. *Physical Review A*, 41(2):784.

Ruelle, D. (1989). *Chaotic evolution and strange attractors*, volume 1. Cambridge University Press.

Saltzman, B. (1962). Finite amplitude free convection as an initial value problem-i. *J. atmos. Sci*, 19(4):329–341.

Sandler, D. and Harnik, N. (2020). Future wintertime meridional wind trends through the lens of subseasonal teleconnections. *Weather and Climate Dynamics*, 1:427–443. 10.5194/wcd-1-427-2020.

Scaife, A. A., Woollings, T., Knight, J., Martin, G., and Hinton, T. (2010). Atmospheric blocking and mean biases in climate models. *Journal of Climate*, 23(23):6143–6152.

Schiemann, R., Athanasiadis, P., Barriopedro, D., Doblas-Reyes, F., Lohmann, K., Roberts, M. J., Sein, D. V., Roberts, C. D., Terray, L., and Vidale, P. L. (2020a). Northern hemisphere blocking simulation in current climate models: evaluating progress from the climate model intercomparison project phase 5 to 6 and sensitivity to resolution. *Weather and Climate Dynamics*, 1(1):277–292.

Schiemann, R., Athanasiadis, P., Barriopedro, D., Doblas-Reyes, F. J., Lohmann, K., Roberts, M. J., Roberts, C. D., Terray, L., Vidale, P. L., and Wild, S. (2020b). Northern hemisphere blocking simulation in current climate models: evaluating progress from CMIP5 to CMIP6 and sensitivity to resolution. *Weather and Climate Dynamics*, 1(1):277–292. 10.5194/wcd-1-277-2020.

Schmidt, G. A., Ruedy, R., Hansen, J. E., Aleinov, I., Bell, N., Bauer, M., and et al. (2014). Configuration and assessment of the giss modele2 contributions to the cmip5 archive. *Journal of Advances in Modeling Earth Systems*, 6(1):141–184. 10.1002/2013MS000265.

Schubert, S. and Lucarini, V. (2016). Dynamical analysis of blocking events: spatial and temporal fluctuations of covariant lyapunov vectors. *Quarterly Journal of the Royal Meteorological Society*, 142(698):2143–2158.

Schwierz, C., Croci-Maspoli, M., and Davies, H. (2004a). Perspicacious indicators of atmospheric blocking. *Geophysical research letters*, 31(6).

Schwierz, C., Croci-Maspoli, M., and Davies, H. C. (2004b). Perspicacious indicators of atmospheric blocking. *Geophysical Research Letters*, 31(6):2003GL019341.

Seneviratne, S. I., Corti, T., Davin, E. L., Hirschi, M., Jaeger, E. B., Lehner, I., Orlowsky, B., and Teuling, A. J. (2010). Investigating soil moisture–climate interactions in a changing climate: A review. *Earth-Science Reviews*, 99(3-4):125–161.

Shen, B.-W., Pielke Sr, R. A., and Zeng, X. (2023). The 50th anniversary of the metaphorical butterfly effect since lorenz (1972): Multistability, multiscale predictability, and sensitivity in numerical models.

Shepherd, T. G. (2019). Storyline approaches to climate change. *Nature Climate Change*, 9:191–193.

Shewalo, G., Shinde, N., Shirode, A., Singh, S., Solanki, J., Tajane, M., Tripathi, G., Gokhale, M., and Gharpure, P. (2012). Report on chaos theory. *Sardar Patel Institute of Technology, Mumbai*.

Shimada, I. and Nagashima, T. (1979). A numerical approach to ergodic problem of dissipative dynamical systems. *Progress of theoretical physics*, 61(6):1605–1616.

Shutts, G. (1983). The propagation of eddies in diffluent jetstreams: Eddy vorticity forcing of 'blocking'flow fields. *Quarterly Journal of the Royal Meteorological Society*, 109(462):737–761.

Sillmann, J., Croci-Maspoli, M., Kallache, M., and Katz, R. W. (2011). Extreme cold winter temperatures in europe under the influence of north atlantic atmospheric blocking. *Journal of Climate*, 24(22):5899–5913.

Smyth, P., Ide, K., and Ghil, M. (1999). Multiple regimes in northern hemisphere height fields via mixturemodel clustering. *Journal of the Atmospheric Sciences*, 56(21):3704–3723.

Sousa, P. M., Trigo, R. M., Barriopedro, D., Soares, P. M., and Santos, J. A. (2018). European temperature responses to blocking and ridge regional patterns. *Climate Dynamics*, 50:457–477.

Sparrow, C. (1982). *The Lorenz Equations: Bifurcations, Chaos, and Strange Attractors*, volume 41 of *Applied Mathematical Sciences*. Springer-Verlag, New York, NY. 10.1007/978-1-4612-5767-7.

Sprenger, M. and Wernli, H. (2015). Lagranto: A lagrangian trajectory tool for atmospheric research. *Geoscientific Model Development*, 8:2569–2584.

Steinfeld, D. (2020). ConTrack - Contour Tracking.

Steinfeld, D., Pfahl, S., and Wernli, H. (2020). The importance of latent heat release in atmospheric blocking formation. *Weather and Climate Dynamics*, 1:27–45.

Stephens, G. L. (2005). Cloud feedbacks in the climate system: A critical review. *Journal of climate*, 18(2):237–273.

Stips, A., Macias, D., Coughlan, C., Garcia-Gorriz, E., and Liang, X. S. (2016). On the causal structure between co2 and global temperature. *Scientific reports*, 6(1):21691.

Strain, E. et al. (2020). The response of atmospheric blocking to climate change: A review. *Current Climate Change Reports*, 6:194–206.

Strogatz, S. H. (2001). *Nonlinear dynamics and chaos: with applications to physics, biology, chemistry, and engineering (studies in nonlinearity)*, volume 1. Westview press.

Strogatz, S. H. (2024). *Nonlinear dynamics and chaos: with applications to physics, biology, chemistry, and engineering*. Chapman and Hall/CRC.

Sura, P. (2002). Noise-induced transitions in a barotropic β-plane channel. *Journal of the atmospheric sciences*, 59(1):97–110.

Tatebe, H., Ogura, T., Nitta, T., Komuro, Y., Ogochi, K., Takemura, T., Sudo, K., Sekiguchi, M., Abe, M., Saito, F., et al. (2019a). Description and basic evaluation of simulated mean state, internal variability, and climate sensitivity in miroc6. *Geoscientific Model Development*, 12(7):2727–2765.

Tatebe, H., Ogura, T., Nitta, T., Komuro, Y., Takemura, T., Sudo, K., Sekiguchi, M., Abe, M., Ogochi, K., Okajima, H., and Watanabe, M. (2019b). Description and basic evaluation of simulated mean state, internal variability, and climate sensitivity in miroc6. *Geoscientific Model Development*, 12(7):2727–2765. 10.5194/gmd-12-2727-2019.

Tatebe, H. and Watanabe, M. (2018). MIROC MIROC6 model output prepared for CMIP6 CMIP historical.

Thompson, D. W. and Wallace, J. M. (2000). Annular modes in the extratropical circulation. part i: Month-to-month variability. *Journal of climate*, 13(5):1000–1016.

Thompson, J. M. T. and Stewart, H. B. (2002). *Nonlinear dynamics and chaos*. John Wiley & Sons.

Tibaldi, S. and Molteni, F. (1990). On the operational predictability of blocking. *Tellus A*, 42(3):343–365.

Trefethen, L. N. and Bau, D. (1997). *Numerical Linear Algebra*. SIAM, Philadelphia.

Trigo, R., Trigo, I., DaCamara, C., and Osborn, T. (2004). Climate impact of the european winter blocking episodes from the ncep/ncar reanalyses. *Climate Dynamics*, 23:17–28.

Trigo, R. M. and DaCamara, C. C. (2004). Blocking episodes in the euro-atlantic sector: The role of precipitation and diabatic processes. *Climate Dynamics*, 23:17–28.

Tung, K. and Rosenthal, A. (1985). Theories of multiple equilibria—a critical reexamination. part i: Barotropic models. *J. Atmos. Sci*, 42(24):2804–2819.

Ulbrich, U. and Speth, P. (1991). The global energy cycle of stationary and transient atmospheric waves: Results from ecmwf analyses. *Meteorology and Atmospheric Physics*, 45(3):125–138.

Vallis, G. K. (2017). *Atmospheric and oceanic fluid dynamics*. Cambridge University Press.

Vannitsem, S. (2017). Predictability of large-scale atmospheric motions: Lyapunov exponents and error dynamics. *Chaos: An Interdisciplinary Journal of Nonlinear Science*, 27(3).

Vannitsem, S., Demaeyer, J., De Cruz, L., and Ghil, M. (2015). Low-frequency variability and heat transport in a low-order nonlinear coupled ocean–atmosphere model. *Physica D: Nonlinear Phenomena*, 309:71–85.

Vannitsem, S. and Lucarini, V. (2016). Statistical and dynamical properties of covariant lyapunov vectors in a coupled atmosphere-ocean model—multiscale effects, geometric degeneracy, and error dynamics. *Journal of Physics A: Mathematical and Theoretical*, 49(22):224001.

Vannitsem, S. and Nicolis, C. (1997a). Lyapunov vectors and error growth patterns in a t21l3 quasigeostrophic model. *Journal of the atmospheric sciences*, 54(2):347–361.

Vannitsem, S. and Nicolis, C. (1997b). Lyapunov vectors and error growth patterns in a t21l3 quasigeostrophic model. *Journal of the Atmospheric Sciences*, 54(2):347 – 361. 10.1175/1520-0469(1997)054<0347:LVAEGP>2.0.CO;2.

Virtanen, P., Gommers, R., Oliphant, T. E., Haberland, M., Reddy, T., Cournapeau, D., Burovski, E., Peterson, P., Weckesser, W., Bright, J., Van Der Walt, S. J., Brett, M., Wilson, J., Millman, K. J., Mayorov, N., Nelson, A. R. J., Jones, E., Kern, R., Larson, E., Carey, C. J., Polat, İ., Feng, Y., Moore, E. W., VanderPlas, J., Laxalde, D., Perktold, J., Cimrman, R., Henriksen, I., Quintero, E. A., Harris, C. R., Archibald, A. M., Ribeiro, A. H., Pedregosa, F., Van Mulbregt, P., SciPy 1.0 Contributors, Vijaykumar, A., Bardelli, A. P., Rothberg, A., Hilboll, A., Kloeckner, A., Scopatz, A., Lee, A., Rokem, A., Woods, C. N., Fulton, C., Masson, C., Häggström, C., Fitzgerald, C., Nicholson, D. A., Hagen, D. R., Pasechnik, D. V., Olivetti, E., Martin, E., Wieser, E., Silva, F., Lenders, F., Wilhelm, F., Young, G., Price, G. A., Ingold, G.-L., Allen, G. E., Lee, G. R., Audren, H., Probst, I., Dietrich, J. P., Silterra, J., Webber, J. T., Slavič, J., Nothman, J., Buchner, J., Kulick, J., Schönberger, J. L., De Miranda Cardoso, J. V., Reimer, J., Harrington, J., Rodríguez, J. L. C., Nunez-Iglesias, J., Kuczynski, J., Tritz, K., Thoma, M., Newville, M., Kümmerer, M., Bolingbroke, M., Tartre, M., Pak, M., Smith, N. J., Nowaczyk, N., Shebanov, N., Pavlyk, O., Brodtkorb, P. A., Lee, P., McGibbon, R. T., Feldbauer, R., Lewis, S., Tygier, S., Sievert, S., Vigna, S., Peterson, S., More, S., Pudlik, T., Oshima, T., Pingel, T. J., Robitaille, T. P., Spura, T., Jones, T. R., Cera, T., Leslie, T., Zito, T., Krauss, T., Upadhyay, U., Halchenko, Y. O., and Vázquez-Baeza, Y. (2020). SciPy 1.0: Fundamental algorithms for scientific computing in Python. *Nature Methods*, 17(3):261–272.

Wallace, J. M. and Gutzler, D. S. (1981). Teleconnections in the geopotential height field during the northern hemisphere winter. *Monthly weather review*, 109(4):784–812.

Wallace, J. M. and Hobbs, P. V. (2006). *Atmospheric science: an introductory survey*, volume 92. Elsevier.

Wang, W., Zhou, W., Wang, X., Fong, S.-K., and Leong, K. C. (2013). Summer high temperature extremes in southeast china associated with the east asian jet stream and circumglobal teleconnection. *Journal of Geophysical Research: Atmospheres*, 118(15):8306–8319. 10.1002/jgrd.50633.

Washington, W. M. and Parkinson, C. (2005). *Introduction to three-dimensional climate modeling*. University science books.

Watanabe, M., Suzuki, T., O'ishi, R., Komuro, Y., Watanabe, S., Emori, S., Takemura, T., Chikira, M., Ogura, T., Sekiguchi, M., Takata, K., Yamazaki, D., Yokohata, T., Nozawa, T., Hasumi, H., Tatebe, H., and Kimoto, M. (2010). Improved climate simulation by miroc5:

Mean states, variability, and climate sensitivity. *Journal of Climate*, 23(23):6312–6335. 10.1175/2010JCLI3679.1.

Weeks, E. R., Tian, Y., Urbach, J., Ide, K., Swinney, H. L., and Ghil, M. (1997). Transitions between blocked and zonal flows in a rotating annulus with topography. *Science*, 278(5343):1598–1601.

Whan, K., Zwiers, F., and Sillmann, J. (2016). The influence of atmospheric blocking on extreme winter minimum temperatures in north america. *Journal of Climate*, 29(12):4361–4381.

Wiggins, S. (2003). *Introduction to Applied Nonlinear Dynamical Systems and Chaos*, volume 2 of *Springer Texts in Applied Mathematics*. Springer-Verlag, New York, 2nd edition. 10.1007/978-0-387-21792-5.

Woollings, T., Barriopedro, D., Methven, J., Son, S.-W., Martius, O., Harvey, B., Sillmann, J., Lupo, A. R., and Seneviratne, S. (2018). Blocking and its response to climate change. *Current climate change reports*, 4:287–300.

Woollings, T., Hannachi, A., and Hoskins, B. (2010). Variability of the north atlantic eddy-driven jet stream. *Quarterly Journal of the Royal Meteorological Society*, 136(649):856–868.

Xavier, A. K., Demaeyer, J., and Vannitsem, S. (2024). Variability and predictability of a reduced-order land–atmosphere coupled model. *Earth System Dynamics*, 15(4):893–912.

Xavier, A. K., Hamilton, O., Faranda, D., and Vannitsem, S. (2025). Predictability of north pacific blocking events: Analogue based analysis of historical MIROC6 simulations. *arXiv preprint arXiv:2504.17691*. Submitted to the Quarterly Journal of the Royal Meteorological Society, 10.48550/arXiv.2504.17691.

Yiou, P. (2014). Anawege: a weather generator based on analogues of atmospheric circulation. *Geoscientific Model Development*, 7(2):531–543.

Yiou, P., Vautard, R., Naveau, P., and Cassou, C. (2007). Inconsistency between atmospheric dynamics and temperatures during the exceptional 2006/2007 fall/winter and recent warming in europe. *Geophysical Research Letters*, 34(21).

Yoden, S. (1983a). Nonlinear interactions in a two-layer, quasi-geostrophic, low-order model with topography part i: Zonal flow-forced wave interactions. *Journal of the Meteorological Society of Japan. Ser. II*, 61(1):1–18.

Yoden, S. (1983b). Nonlinear interactions in a two-layer, quasi-geostrophic, low-order model with topography part ii: Interactions between zonal flow, forced waves and free waves. *Journal of the Meteorological Society of Japan. Ser. II*, 61(1):19–35.

Yoden, S. (2007). Atmospheric predictability. *Journal of the Meteorological Society of Japan. Ser. II*, 85:77–102.

Zhengxin, Z. and Baozhen, Z. (1982). Equilibrium states of ultra-long waves driven by non-adiabatic heating and blocking situation. *Science in China (Series B)*, 4:36l–371.

Zhu, Z. (1985). Equilibrium states of planetary waves forced by topography and perturbation heating and blocking situation. *Advances in Atmospheric Sciences*, 2(3):359–367.